Two Primary Basalt Magma Types from Northwest Rota-1 Volcano, Mariana Arc and its Mantle Diapir or Mantle Wedge Plume

Y. TAMURA[1]*, O. ISHIZUKA[2], R. J. STERN[3], H. SHUKUNO[1], H. KAWABATA[1], R. W. EMBLEY[4], Y. HIRAHARA[1], Q. CHANG[1], J.-I. KIMURA[1], Y. TATSUMI[1], A. NUNOKAWA[1] AND S. H. BLOOMER[5]

[1]INSTITUTE FOR RESEARCH ON EARTH EVOLUTION (IFREE), JAPAN AGENCY FOR MARINE–EARTH SCIENCE AND TECHNOLOGY (JAMSTEC), YOKOSUKA 237-0061, JAPAN

[2]INSTITUTE OF GEOSCIENCE, GEOLOGICAL SURVEY OF JAPAN/AIST, TSUKUBA 305-8567, JAPAN

[3]GEOSCIENCES DEPARTMENT, UNIVERSITY OF TEXAS AT DALLAS, 800 W. CAMPBELL ROAD, RICHARDSON, TX 75080-3021, USA

[4]PACIFIC MARINE ENVIRONMENTAL LABORATORY, NOAA/PMEL, 2115 SE O.S.U. DR., NEWPORT, OR 97365-5258, USA

[5]DEPARTMENT OF GEOSCIENCES, OREGON STATE UNIVERSITY, 128 KIDDER HALL, CORVALLIS, OR 97331, USA

Primitive basalts are rarely found in arcs. The active NW Rota-1 volcano in the Mariana arc has erupted near-primitive lavas, which we have sampled with ROV Hyper-Dolphin (HPD). Samples from the summit (HPD480) and eastern flank (HPD488) include 17 magnesian basalts (51–52 wt % SiO_2) with 7·5–9·5 wt % MgO and Mg-number of 61–67, indicating little fractionation. Olivine phenocrysts are as magnesian as Fo_{93} and contain 0·4 wt % NiO; the Cr/(Cr + Al) values of spinels are mostly 0·5–0·8, indicating equilibrium with depleted mantle. There are three petrographic groups, based on phenocryst populations: (1) cpx–olivine basalt (COB); (2) plagioclase–olivine basalt (POB); (3) porphyritic basalt. Zr/Y and Nb/Yb are higher in POB (3·1–3·2 and 1·2–1·5, respectively) than in COB (Zr/Y = 2·8–3·0 and Nb/Yb = 0·7–0·9), suggesting that POB formed from lower degrees of mantle melting, or that the COB mantle source was more depleted. On the other hand, COB have Ba/Nb (70–80) and Th/Nb (0·4–0·5) that are higher than for POB (Ba/Nb = 30–35 and Th/Nb = 0·1–0·2), and also have steeper light rare earth element (LREE)-enriched patterns. Moreover, COB have enriched $^{87}Sr/^{86}Sr$ and $^{143}Nd/^{144}Nd$, and higher Pb isotope values, suggesting that COB has a greater subduction component than POB. $^{176}Hf/^{177}Hf$ between COB and POB are similar and Hf behavior in COB and POB is similar to that of Zr, Y and HREE, suggesting that Hf is not included in the subduction component, which produced the differences between COB and POB. The calculated primary basaltic magmas of NW Rota-1 volcano (primary COB and POB magmas) indicate segregation pressures of 2–1·5 GPa (equivalent to 65–50 km depth). These magmas formed by 24–18% melting of mantle peridotite having Mg-number ~89·5. Diapiric ascent of hydrous peridotite mixed heterogeneously with sediment melts may be responsible for the NW Rota-1 basalts. These two basalt magma types are similar to those found at Sumisu and Torishima volcanoes in the Izu–Bonin arc, with COB representing wetter and POB representing drier magmas, where subduction zone-derived melt components are coupled with the water contents.

INTRODUCTION

Kushiro (2001) noted that 'melting experiments on mantle peridotites and related materials at high pressures were

*Corresponding author. Telephone: +81-46-867-9761. Fax: +81-46-867-9625. E-mail: tamuray@jamstec.go.jp

initiated in the 1950s when it was widely recognized by Earth scientists that peridotite is the major constituent material of the upper mantle of the Earth.—Melting experiments of natural peridotites have been carried out mainly for the purpose of determining the compositions of mantle partial melts in relation to the genesis of basalt magmas.' Moreover, supra-subduction zone peridotites show large compositional variations (e.g. Parkinson & Pearce, 1998; Takazawa et al., 2000; Ishimaru et al., 2007; Arai & Ishimaru, 2008; Ionov, 2010), which largely reflect partial melting processes. In spite of this, our understanding of mantle melting above subduction zones is impeded because of the scarcity of melts generated in equilibrium with peridotite, so-called primary magmas. Most arc magmas are fractionated, with 4–6 wt % MgO (e.g. Tamura & Tatsumi, 2002; Kelemen et al., 2003; Tamura, 2003) and differ significantly from primary magmas. Finding and studying relatively unfractionated mantle-derived primary lavas is fundamental to understanding the nature of the mantle source and the processes that yield primary magmas.

We present here results from a study of the petrography and geochemistry of recently discovered primitive and phenocryst-poor lavas from the submarine NW Rota-1 volcano in the Mariana arc. These magnesian basalts show surprising compositional variability, which we have classified petrographically into three groups: (1) cpx–olivine basalt (COB); (2) plagioclase–olivine basalt (POB); (3) porphyritic basalt. We calculate primary COB magmas and POB magmas for NW Rota-1 volcano. By using these primary magmas, existing melting experiments of mantle peridotites, and supra-subduction zone peridotites, we gain new insights into the nature and origin of arc magmas.

An additional motivation for this study is to compare primitive Mariana arc lavas with those of the Izu–Bonin arc. Tamura et al. (2005, 2007) found two types of basalt magmas (low- and high-Zr basalts) in Sumisu and Torishima volcanoes originating from wet and dry parental basaltic magmas, respectively. COB and POB may be the primitive equivalents of these Izu–Bonin basalt magma types, further suggesting universal primitive arc magma types. This finding could help explain the variability of fractionated arc magmas, but at the same time it raises the questions: 'Why do COB and POB coexist in arc volcanoes and how are they produced in the mantle wedge?'

GEOLOGICAL BACKGROUND

The Izu–Bonin–Mariana arc system (IBM) stretches over 2800 km, from near Tokyo, Japan, to beyond Guam, USA, and is an excellent example of an intraoceanic convergent margin (Fig. 1a) [see Stern et al. (2003) for an overview]. The Mariana segment has been subdivided into the Northern Seamount Province (NSP), Central Island Province (CIP) and Southern Seamount Province (SSP) (Bloomer et al., 1989) (Fig. 1b). The CIP is best known and has the most complete dataset among the three provinces (e.g. Woodhead, 1989; Elliott et al., 1997; Pearce et al., 2005; Wade et al., 2005; Stern et al., 2006). Less is known about the composition of lavas erupted from smaller, submarine arc volcanoes, where there is a chance that mantle-derived melts can arrive at the surface without significant fractionation. Northwest Rota-1 (14°36·05′N, 144°46·52′E) is a submarine volcano that is located ∼100 km north of Guam in the Mariana SSP (Fig. 1b); it is the largest edifice in a volcanic cross-chain that extends east–west along 14°40′N; Kohut et al. (2006) referred to this as the 14°40′N cross-chain. NW Rota-1 is located about 40 km west of the SSP volcanic front, defined in the region by Esmeralda Bank and West Rota volcanoes. Esmeralda Bank is an active volcano, dominated by fractionated basalt and basaltic andesite (Stern & Bibee, 1984). West Rota volcano is extinct but erupted voluminous silicic pyroclastic deposits from a large (10 km diameter) caldera (Stern et al., 2008). The only volcano in the 14°40′N cross-chain that has been studied petrologically is Chaife volcano, ∼10 km east of NW Rota-1; this has erupted unusually primitive basalts, picrite and ankaramite (Kohut et al., 2006). Unpublished results show that Mt. Manganese to the east of NW Rota-1 is also dominated by primitive basalts (Kohut et al., personal communication, 2010). Cross-chains are common in the Marianas and those that do exist consist of one or two large edifices aligned behind the magmatic front (e.g. Guguan cross-chain, Stern et al., 2006; Kasuga cross-chain, Stern et al., 1993). In contrast, the 14°40′N cross-chain consists of four substantial edifices (among which NW Rota-1 is the largest) and at least five smaller cones scattered throughout an east–west zone that is ∼40 km at the magmatic front and narrows to its western terminus, ∼100 km away. This region is seismically active with focal mechanisms that indicate NNE–SSW extension (Heeszel et al., 2008). This extension may have enhanced adiabatic decompression of underlying mantle peridotite and provided easy access for magmas to rise to the surface without fractionating.

The Mariana Trough is an active back-arc basin located west of the Mariana arc (Fig. 1b). The Mariana Trough shows marked variations along strike, with seafloor spreading south of 22° and rifting farther north (Yamazaki et al., 2003). The spreading rate determined by global positioning system (GPS) increases southward from 16 mm a^{-1} at 18·75°N to 45 mm a^{-1} at 13·5°N (Kato et al., 2003). The spreading ridge converges toward the arc at its southern and northern extremities and has a maximum distance from the arc of about 100 km at 18°N. NW Rota-1 is about 60 km east of the spreading axis (Fig. 1b). Back-arc basin lavas range from those indistinguishable from mid-ocean
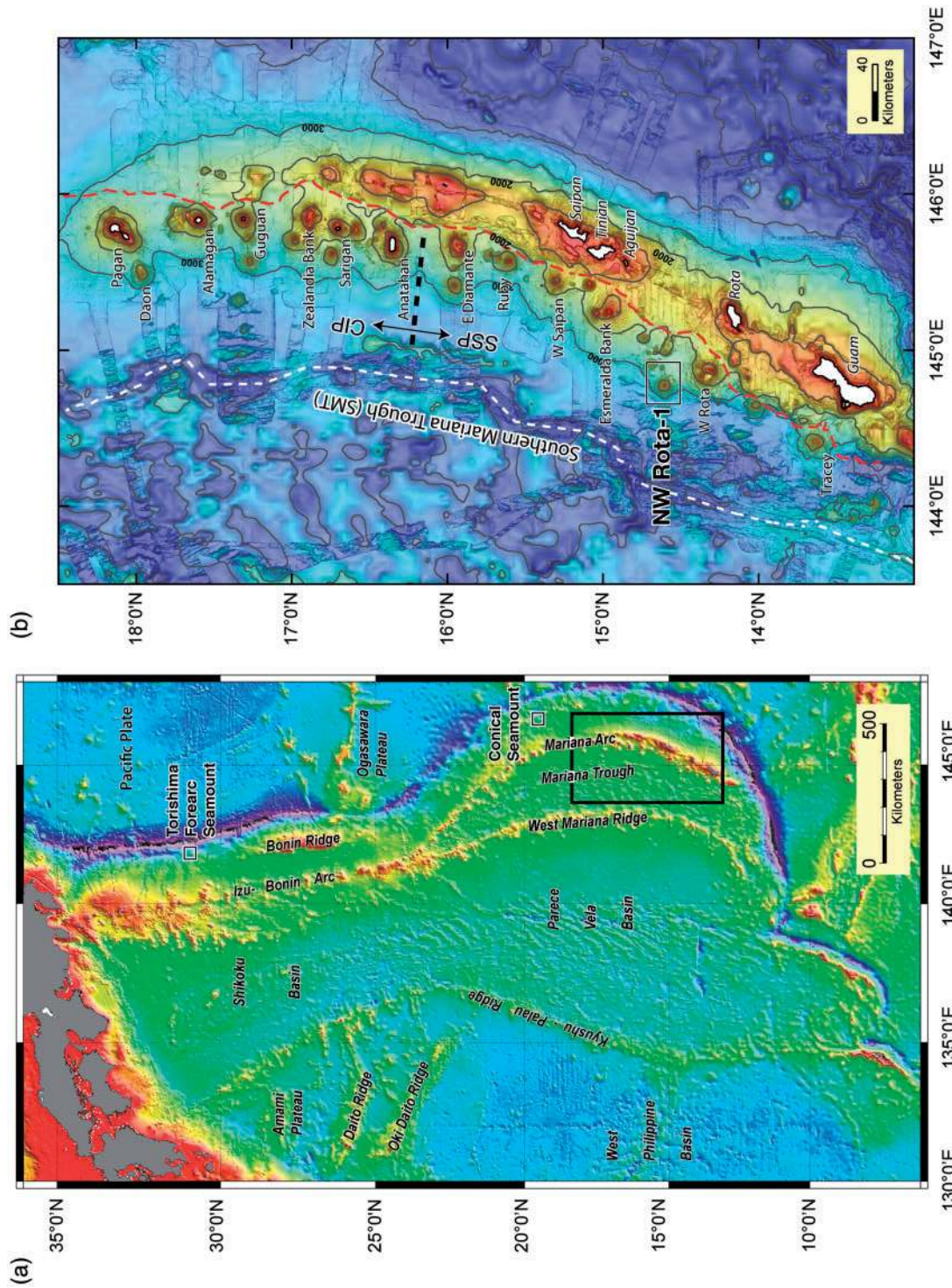
Fig. 1. (a) Bathymetry of the eastern Philippine Sea, including the Izu–Bonin–Mariana (IBM) arc system. Two serpentinite seamounts, Torishima forearc seamount in the Izu–Bonin forearc and Conical seamount in the Mariana forearc, are located by squares. The rectangle indicates the area of (b). (b) Map showing the southern IBM arc, which includes from west to east, the Mariana Trough (back-arc basin), the active Mariana arc, the old Mariana forearc (including the islands of Saipan, Tinian, Aguijan, Rota and Guam), and the Mariana Trench. The magmatic arc in this map is a part of the Central Island Province (CIP) mostly defined by volcanic islands, ranging from Farallon de Pajaros (20°32′N) to Anatahan (16°20′N) and the Southern Seamount Province (SSP), ranging from East Diamante (15°55′N) to Tracey (13°38′N). White dashed line shows the Mariana Trough spreading ridge, which has been active since 7 Ma. Basaltic glasses have been dredged along the spreading ridge of the southern Mariana Trough (SMT; 15–17°N) (Gribble *et al.*, 1996; Pearce *et al.*, 2005). Red dashed line shows the boundary between the active Mariana arc and the Mariana forearc, which was active from Eocene to Miocene time. (c) NW Rota-1 volcano showing the sampling tracks of ROV *Hyper-Dolphin*: the summit (HPD 480, 48l and 952), eastern flank (HPD 488) and east knoll (HPD 951).
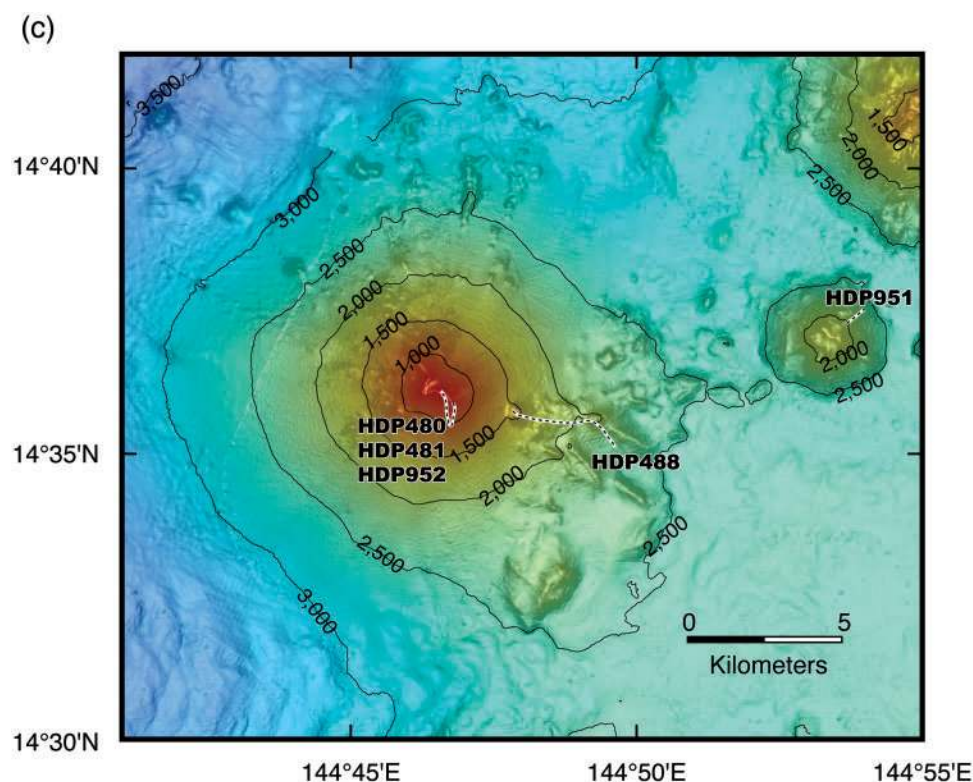
Fig. 1. Continued.

ridge basalts (MORB) to ones similar to island-arc basalts (IAB), but the characteristic back-arc basin basalts (BABB) are intermediate between these two end-members (e.g. Gill, 1976; Pearce & Stern, 2006). We compare BABB from the southern Mariana Trough (15–17°N) with COB and POB from NW Rota-1 to gain insight into mantle input beneath the back-arc region and the interaction of mantle and subduction components.

NW Rota-1 is conical and about 16 km in diameter at its base at 2700 m water depth. The summit is about 520 m deep (Fig. 1c). Continuous submarine eruption has occurred near the summit since 2004 and has been witnessed during remotely operated vehicle (ROV) visits in 2004, 2005, 2006, 2008, 2009 and 2010 (Embley *et al.*, 2006; Chadwick *et al.*, 2008, 2010). This activity is characterized by the repeated buildup and collapse of a cinder cone at the vent (Chadwick *et al.*, 2010). We visited NW Rota-1 in 2005 (NT05-17) and 2009 (NT09-02), using ROV *Hyper-Dolphin* and R.V *Natsushima*. Rocks were collected from the summit areas at 520–1000 m depth (dives HPD480, HPD481 and HPD952), from the eastern flank of the volcano [HPD488; 1500–2300 m below sea level (b.s.l.)], where pillow lavas dominate, and from a knoll ∼13 km east of the NW Rota-1 summit, which consists of monolithological andesite lava flows (HPD951; 2000–2300 m b.s.l.) (Fig. 1c). We present new analyses of rocks from NW Rota-1 volcano and the unnamed knoll to its east.

ANALYTICAL METHODS

After sawing and jaw crushing, all samples were pulverized in an agate ball mill. Major and selected trace elements (Ba, Ni, Cu, Zn, Pb, Th, Rb, Sr, Y, Zr and Nb) were determined by X-ray fluorescence (XRF) at IFREE, JAMSTEC. Trace elements were analyzed on pressed powder discs, and major elements were determined on fused glass discs. A mixture of ∼0·4 g powdered sample and 4 g of anhydrous lithium tetraborate ($Li_2B_4O_7$) was used; no matrix correction was applied because of the high dilution. All discussion in this paper refers to analyses that have been normalized to 100% on a volatile-free basis with total iron calculated as FeO.

The rare earth elements (REE), V, Cr, Rb, Sr, Y, Zr, Nb, Cs, Ba, Hf, Ta, Pb, Th and U concentrations were analyzed by inductively coupled plasma mass spectrometry (ICP-MS) on a VG Platform instrument at the Geological Survey of Japan/AIST. About 100 mg of powder from each sample was dissolved in a $HF–HNO_3$ mixture (5:1). After evaporation to dryness, the residues were redissolved with 2% HNO_3 prior to analysis. Reproducibility is better than ±4% (2 standard deviations; SD) for the REE,

Rb and Nb, and better than ±6% (2 SD) for other elements.

Isotopic compositions of Sr, Nd, and Pb were determined on 200 mg of hand-picked 0·5–1 mm rock chips. The chips were leached in 6M HCl at 140°C for 1 h prior to dissolution in HF–HNO$_3$. Sr and Nd isotope ratios were measured on a seven-collector VG Sector 54 mass spectrometer. Sr was isolated using Sr resin (Eichrom Industries, Illinois). For Nd isotopic analysis, the REE were initially separated by cation exchange before isolating Nd on Ln resin (Eichrom Industries) columns. Sr and Nd isotopic compositions were determined as the average of 150 ratios by measuring ion beam intensities in multidynamic collection mode. Isotope ratios were normalized to $^{86}Sr/^{88}Sr = 0.1194$ and $^{146}Nd/^{144}Nd = 0.7219$. Measured values for NBS SRM-987 and JNdi-1 ($^{143}Nd/^{144}Nd = 0.512115$; Tanaka *et al.*, 2000) were $^{87}Sr/^{86}Sr = 0.710276 \pm 6$ (2 SD, $n = 4$) and $^{143}Nd/^{144}Nd = 0.512104 \pm 12$ (2 SD, $n = 4$) during the measurement period.

Pb was isolated using AG1-X8 200–400 mesh anion exchange resin. Procedural Pb blanks were <30 pg, considered negligible relative to the amount of sample analyzed. Pb isotopic measurements were made in multidynamic collection mode using the double spike technique (Southampton-Brest-Lead 207–204 spike SBL74; Ishizuka *et al.*, 2003). Natural (unspiked) measurements were made on 60–70% of collected Pb, giving ^{208}Pb beam intensities of $(2.5–3.0) \times 10^{11}$ A. Fractionation-corrected Pb isotopic compositions and internal errors were obtained by a closed-form linear double-spike deconvolution (Johnson & Beard, 1999). The reproducibility of Pb isotopic measurement (external error of 2 SD) by double spike is <200 ppm for all $^{20x}Pb/^{204}Pb$ ratios. Measured values for NBS SRM-981 during the measurement period were $^{206}Pb/^{204}Pb = 16.9401 \pm 0.0011$, $^{207}Pb/^{204}Pb = 15.5003 \pm 0.0025$, and $^{208}Pb/^{204}Pb = 36.7236 \pm 0.0041$.

Hf isotopes were determined in IFREE, JAMSTEC. Prior to sample digestion, the powder sample splits were leached with 6N HCl at room temperature for 1 h, rinsed with Milli-Q water, and then dried. The samples were digested with HF and HClO$_4$, and then dissolved in HCl. Hf was separated by a single-column method using Ln resin following the method of Münker *et al.* (2001). The total procedural blanks for Hf were <25 pg.

Hf isotope ratios were measured by multi-collector (MC)-ICP-MS on a sector-type Neptune Thermo Scientific® system at IFREE, JAMSTEC. Mass fractionation factor was determined by the $^{179}Hf/^{177}Hf$ ratio and isotope ratios were normalized to a $^{179}Hf/^{177}Hf$ value of 0·7325 using an exponential law. ^{173}Yb and ^{175}Lu peaks were monitored to correct interference of ^{176}Yb and ^{176}Lu on the ^{176}Hf peak. Repeated measurement of the JMC475 standard provided $^{176}Hf/^{177}Hf$ ratios of 0·282141 ±0·000010

(2 SD, $n = 9$) during the measurements. The reported $^{176}Hf/^{177}Hf$ ratio is adjusted by reference to a JMC475 $^{176}Hf/^{177}Hf = 0.28216$.

Representative major and trace element and Sr–Nd–Pb–Hf isotope data for NW Rota-1 lavas are reported in Table 1. The entire dataset of volcanic rocks from NW Rota-1 volcano, ranging from basalt to andesite, is available as Electronic Appendix Table 1, which may be downloaded from http://www.petrology.oxfordjournals.org/.

Microprobe analyses were carried out on the JAMSTEC JEOL JXA-8900 Superprobe equipped with five wavelength-dispersive spectrometers (WDS). Olivine analyses were made with 100 s counting time, 20 kV accelerating voltage, 25 nA beam current, and 5 μm spot diameter, which ensured reliable Ni analyses. Pyroxene, spinel and plagioclase analyses were made with 20 s counting time, 15 kV accelerating voltage, and 15 nA beam current. Representative mineral compositions from NW Rota-1 volcano are given in Electronic Appendix Table 2, which may be downloaded from http://www.petrology.oxfordjournals.org/.

MAGMATIC VARIATION OF NW ROTA-1 VOLCANO

Figure 2a shows silica variation diagrams of lavas and scoria from NW Rota-1 volcano, which range from 51 to 58 wt % SiO$_2$ and form a medium-K suite as defined by Gill's (1981) criterion (Fig. 2a). Rocks from the summit area and eastern flank have a similar silica range, but the east knoll consists of andesite lavas with ~55 wt % SiO$_2$. These have higher FeO* than NW Rota-1 lavas as well as lower Na$_2$O, K$_2$O and P$_2$O$_5$ contents. Thus the east knoll could be a monogenetic volcano unrelated to the NW Rota-1 magmatic system. NW Rota-1 andesite lavas with 57–58 wt% SiO$_2$ show systematic differences between the summit area and the eastern flank. Andesites from the summit area have higher TiO$_2$, Al$_2$O$_3$ and P$_2$O$_5$ and lower SiO$_2$ and MgO than those from the eastern flank. Basalts (<53 wt % SiO$_2$) from NW Rota-1 are also variable. Basalts from the eastern flank are the most magnesian (~9·5 wt % MgO), but some rocks from the summit also have >8 wt % MgO (it should be noted that the present eruption is basaltic, with ~51–52% SiO$_2$). Interestingly, the magnesian basalts range in TiO$_2$ content from 0·75 to 0·9 wt %.

Figure 2b shows silica vs Mg-number [$=100 \, Mg/(Mg + \sum Fe)$], silica vs FeO*/MgO and silica vs Zr/Y (measured by XRF). Rocks from the eastern flank (HPD488) are calc-alkaline, the east knoll andesites (HPD951) are tholeiitic, and lavas from the summit (HPD 480, 481 and 952) straddle the calc-alkaline–tholeiitic boundary of Miyashiro (1974). Arculus (2003) proposed

Table 1: Representative major and trace element and Sr–Nd–Pb–Hf isotope data for NW Rota-1 and East Knoll lavas

Locality:	NW Rota-1 summit						
Magma type:	Porphyritic basalt		Porphyritic basalt	Porphyritic basalt			
Sample no.:	HPD480R01	HPD480R06	HPD480R09	HPD480R10	HPD481R01	HPD481R06	HPD481R10
Latitude (N):	14°35·991′	14°36·004′	14°36·077′	14°36·085′	14°36·051′	14°35·451′	14°35·574′
Longitude (E):	144°46·509′	144°46·435′	144°46·423′	144°46·422′	144°46·522′	144°46·761′	144°46·776′
Depth (m b.s.l.):	606	645	570	561	532	1068	952
wt %							
SiO_2	51·26	51·34	51·11	51·05	51·73	56·83	56·85
TiO_2	0·76	0·77	0·76	0·76	0·78	0·96	0·98
Al_2O_3	17·21	20·27	17·13	17·19	20·33	18·54	17·94
Fe_2O_3	8·47	7·49	8·62	8·54	7·55	7·63	7·87
MnO	0·14	0·13	0·15	0·15	0·13	0·14	0·15
MgO	7·70	4·78	8·24	7·95	4·72	2·81	3·06
CaO	11·18	11·40	11·03	11·17	11·43	8·11	7·95
Na_2O	2·33	2·54	2·28	2·29	2·59	3·59	3·54
K_2O	0·61	0·65	0·61	0·61	0·66	1·16	1·18
P_2O_5	0·15	0·16	0·15	0·15	0·16	0·24	0·24
Total	99·83	99·51	100·07	99·84	100·06	100·01	99·75
Trace elements (ppm) by XRF							
Ba	116·5	119·8	130·8	120·5		201·6	220·8
Ni	92·2	41·7	120·4	101·4		6·7	10·4
Cu	85·5	89·4	88·5	90·2		56·4	62·4
Zn	62·8	61·7	65·5	63·2		73·7	75·2
Pb	1·6			2·4		2·9	3·6
Th		1·2	2·1	1·0		2·6	3·0
Rb	11·3	11·8	11·6	11·2		21·9	22·4
Sr	320·8	377·1	322·6	323·4		364·2	353·4
Y	17·0	16·4	16·4	16·4		25·7	26·0
Zr	54·0	55·7	53·3	52·2		99·5	100·2
Nb	2·1	1·9	1·8	1·9		3·6	3·3
Trace elements (ppm) by ICP-MS							
V							
Cr							
Ni							
Rb	11·09	11·49	11·30	11·28	12·31	21·33	21·35
Sr	309	379	311	340	369	341	358
Y	18·0	19·9	20·3	18·4	19·4	31·2	29·9
Zr	57·7	61·9	54·2	57·8	65·1	104·6	107·1
Nb	1·89	2·04	1·98	1·91	1·97	3·71	3·63
Cs	0·22	0·25	0·25	0·21	0·23	0·47	0·42
Ba	120·3	141·0	134·0	128·5	141·8	241·5	232·5
La	6·61	7·44	6·98	7·05	7·03	12·53	12·22
Ce	14·43	15·42	15·07	14·97	14·96	26·33	26·38
Pr	1·97	2·07	2·09	2·02	2·05	3·50	3·43
Nd	9·74	9·76	9·83	9·68	10·23	16·67	15·99
Sm	2·53	2·69	2·72	2·48	2·51	4·42	4·10
Eu	0·91	0·96	0·93	0·91	0·91	1·33	1·37
Gd	2·97	3·14	3·04	2·87	2·87	4·58	4·57
Tb	0·50	0·49	0·51	0·49	0·48	0·79	0·77
Dy	3·12	3·05	3·15	3·03	3·05	4·66	4·68
Ho	0·66	0·64	0·67	0·63	0·63	1·01	0·98
Er	1·84	1·92	1·99	1·79	1·75	3·02	2·94
Tm	0·28	0·27	0·28	0·28	0·25	0·43	0·38
Yb	1·79	1·90	2·00	1·72	1·79	3·02	2·85
Lu	0·27	0·28	0·29	0·27	0·28	0·44	0·45
Hf	1·79	1·50	1·57	1·44	1·44	2·77	2·87
Ta	0·140	0·176	0·177	0·136	0·146	0·278	0·250
Pb	1·51	1·75	1·86	1·59	1·54	2·90	2·84
Th	0·763	0·871	0·929	0·761	0·919	1·778	1·615
U	0·296	0·368	0·353	0·296	0·314	0·624	0·590
$^{87}Sr/^{86}Sr$		0·703255			0·703234	0·703244	
$^{143}Nd/^{144}Nd$		0·512979			0·513002	0·512989	
$^{206}Pb/^{204}Pb$		18·8060			18·8077	18·8088	
$^{207}Pb/^{204}Pb$		15·5506			15·5516	15·5518	
$^{208}Pb/^{204}Pb$		38·405			38·407	38·414	
$^{176}Hf/^{177}Hf$							

(continued)

Table 1: Continued

Locality:	NW Rota-1 eastern flank						
Magma type:	COB	POB	COB	COB	COB	COB	
Sample no.:	HPD488R01	HPD488R02	HPD488R03	HPD488R04	HPD488R05	HPD488R06	HPD488R07
Latitude (N):	14°35·290′	14°35·306′	14°35·318′	14°35·318′	14°35·325′	14°35·325′	14°35·325′
Longitude (E):	144°49·609′	144°49·606′	144°49·595′	144°49·595′	144°49·596′	144°49·596′	144°49·596′
Depth (m b.s.l.):	2260	2255	2238	2238	2229	2229	2229
wt %							
SiO_2	51·21	51·64	50·57	50·69	50·74	50·69	50·97
TiO_2	0·80	0·90	0·76	0·75	0·75	0·76	0·78
Al_2O_3	16·56	16·75	15·85	15·95	15·89	16·02	16·52
Fe_2O_3	9·55	8·92	9·59	9·50	9·63	9·54	9·49
MnO	0·16	0·16	0·17	0·16	0·16	0·16	0·16
MgO	7·71	7·75	8·81	8·67	9·02	8·56	7·96
CaO	11·31	10·42	11·31	11·37	11·33	11·35	11·33
Na_2O	2·03	2·51	1·94	1·91	1·91	1·90	2·00
K_2O	0·51	0·54	0·47	0·48	0·48	0·50	0·50
P_2O_5	0·14	0·16	0·14	0·14	0·14	0·14	0·14
Total	99·98	99·76	99·59	99·62	100·06	99·61	99·87
Trace elements (ppm) by XRF							
Ba	109·3	89·2	92·1	114·5	119·0	108·3	98·1
Ni	69·1	101·8	99·6	99·8	104·8	93·9	75·4
Cu	75·2	58·2	83·4	83·6	85·6	83·3	78·4
Zn	72·8	72·9	72·4	73·8	72·4	73·0	71·5
Pb	1·9						
Th	0·9		0·7		0·7	0·7	0·9
Rb	8·6	8·3	7·9	8·2	8·1	7·7	8·1
Sr	353·5	311·1	345·8	343·9	347·9	349·9	350·6
Y	15·6	17·5	14·6	14·6	14·4	14·5	14·5
Zr	43·8	62·8	41·6	40·8	40·6	40·8	42·8
Nb	1·5	3·3	1·2	1·0	1·4	1·0	1·3
Trace elements (ppm) by ICP-MS							
V		274·9		289·5		295·7	
Cr		230·79		287·06		273·84	
Ni		107·0		95·0		103·6	
Rb	8·52	8·04	7·73	7·57	8·29	8·00	8·23
Sr	348	322	330	349	368	340	325
Y	18·1	21·1	16·2	16·9	18·3	17·1	17·0
Zr	47·9	66·6	43·8	41·3	44·9	40·9	44·9
Nb	1·38	3·66	1·20	1·34	1·23	1·28	1·39
Cs	0·24	0·16	0·18	0·17	0·20	0·15	0·15
Ba	95·1	102·7	94·7	95·9	100·7	97·0	97·7
La	5·73	5·87	5·58	5·52	6·07	5·58	6·27
Ce	13·06	13·45	12·44	11·82	13·82	12·33	13·68
Pr	1·78	1·75	1·74	1·61	1·88	1·61	1·74
Nd	9·02	8·36	8·78	8·18	9·15	7·98	8·85
Sm	2·35	2·48	2·30	2·13	2·55	2·15	2·46
Eu	0·84	0·95	0·82	0·80	0·91	0·79	0·91
Gd	2·63	2·89	2·55	2·47	2·92	2·27	2·81
Tb	0·46	0·49	0·44	0·42	0·48	0·40	0·47
Dy	2·77	3·12	2·74	2·53	2·79	2·51	2·76
Ho	0·61	0·70	0·57	0·56	0·59	0·54	0·57
Er	1·76	1·94	1·65	1·61	1·77	1·55	1·68
Tm	0·27	0·31	0·25	0·25	0·27	0·23	0·27
Yb	1·68	1·94	1·56	1·56	1·69	1·46	1·63
Lu	0·25	0·30	0·25	0·24	0·24	0·23	0·24
Hf	1·19	1·55	1·20	1·10	1·22	1·04	1·17
Ta	0·124	0·182	0·118	0·086	0·132	0·079	0·132
Pb	1·37	1·39	1·27	1·40	1·25	1·94	1·28
Th	0·594	0·577	0·532	0·583	0·534	0·588	0·596
U	0·237	0·210	0·217	0·204	0·246	0·204	0·229
$^{87}Sr/^{86}Sr$	0·703151	0·703111	0·703168				0·703152
$^{143}Nd/^{144}Nd$	0·512987	0·513019	0·513018				0·512985
$^{206}Pb/^{204}Pb$	18·8211	18·6674	18·8232				18·8213
$^{207}Pb/^{204}Pb$	15·5471	15·5265	15·5475				15·5490
$^{208}Pb/^{204}Pb$	38·399	38·267	38·398				38·403
$^{176}Hf/^{177}Hf$	0·512987	0·513019	0·513018				0·512985

(continued)

Table 1: Continued

Locality:	NW Rota-1 eastern flank						
Magma type:	COB	COB	POB	POB	POB	POB	
Sample no.:	HPD488R08	HPD488R09	HPD488R10	HPD488R11	HPD488R12	HPD488R13	HPD488R15
Latitude (N):	14°35·367′	14°35·400′	14°35·453′	14°35·453′	14°35·514′	14°35·551′	14°35·603′
Longitude (E):	144°49·581′	144°49·569′	144°49·541′	144°49·541′	144°49·466′	144°49·422′	144°48·126′
Depth (m b.s.l.):	2196	2180	2151	2151	2117	2079	1675
wt %							
SiO_2	50·76	50·98	51·04	50·83	50·66	50·76	57·53
TiO_2	0·75	0·79	0·87	0·84	0·85	0·86	0·81
Al_2O_3	15·82	16·20	16·24	15·90	15·95	15·78	17·18
Fe_2O_3	9·69	9·52	9·10	9·15	9·20	9·23	7·48
MnO	0·16	0·16	0·16	0·16	0·16	0·16	0·16
MgO	8·76	8·05	8·57	9·40	9·04	9·29	3·77
CaO	11·39	11·25	11·06	11·08	10·96	11·05	7·81
Na_2O	1·91	1·99	2·25	2·17	2·22	2·20	3·56
K_2O	0·50	0·51	0·50	0·45	0·48	0·45	1·19
P_2O_5	0·13	0·14	0·15	0·14	0·14	0·14	0·21
Total	99·87	99·59	99·93	100·12	99·66	99·92	99·69
Trace elements (ppm) by XRF							
Ba	102·4	107·2	84·0	83·0	82·7	102·5	212·7
Ni	101·2	77·9	123·5	142·4	135·0	131·8	17·5
Cu	77·0	76·1	79·5	71·7	76·4	73·1	53·1
Zn	71·9	73·3	72·5	71·3	75·8	72·1	69·5
Pb		1·6					2·9
Th	0·6			0·9		1·1	1·5
Rb	8·0	8·8	7·6	6·8	7·4	7·1	23·6
Sr	344·2	349·3	301·1	288·9	298·6	301·0	395·9
Y	14·5	14·9	17·7	16·9	17·4	16·8	25·6
Zr	40·1	43·1	54·7	52·6	53·8	53·6	92·8
Nb	1·1	1·5	2·4	2·3	2·4	2·6	2·8
Trace elements (ppm) by ICP-MS							
V	296·6	297·1	283·8		278·5	277·7	
Cr	330·65	343·59	360·37		384·72	404·55	
Ni	96·2	99·2	124·8		132·5	148·0	
Rb	7·55	7·68	7·20	6·77	7·13	6·60	22·72
Sr	352	345	306	322	303	305	395
Y	16·6	16·9	19·6	20·8	19·8	19·0	29·0
Zr	41·1	41·9	57·8	61·4	56·5	56·2	100·6
Nb	1·30	1·23	2·89	2·84	2·71	2·58	3·15
Cs	0·16	0·16	0·17	0·15	0·15	0·12	0·43
Ba	96·0	95·8	87·1	88·9	86·7	84·2	222·0
La	5·31	5·29	4·99	5·34	4·86	4·83	12·02
Ce	11·71	12·08	11·84	13·04	11·49	11·38	26·17
Pr	1·59	1·58	1·61	1·70	1·54	1·52	3·48
Nd	7·78	7·92	7·70	9·14	7·60	7·73	16·22
Sm	2·15	2·16	2·29	2·68	2·26	2·17	4·26
Eu	0·77	0·80	0·85	0·93	0·85	0·88	1·42
Gd	2·45	2·41	2·60	3·04	2·80	2·56	4·45
Tb	0·41	0·41	0·47	0·53	0·47	0·45	0·76
Dy	2·52	2·47	3·04	3·24	3·01	2·89	4·57
Ho	0·54	0·54	0·63	0·72	0·66	0·65	1·01
Er	1·63	1·52	1·90	2·15	1·98	1·85	2·90
Tm	0·25	0·23	0·29	0·33	0·28	0·28	0·37
Yb	1·56	1·47	1·83	2·02	1·85	1·80	2·88
Lu	0·24	0·23	0·29	0·33	0·29	0·27	0·46
Hf	1·09	1·06	1·38	1·48	1·34	1·34	2·35
Ta	0·081	0·076	0·141	0·227	0·139	0·141	0·229
Pb	1·39	1·35	1·22	1·42	1·33	1·13	2·91
Th	0·576	0·583	0·461	0·475	0·470	0·467	1·583
U	0·211	0·198	0·179	0·277	0·208	0·164	0·618
$^{87}Sr/^{86}Sr$					0·703072	0·703064	
$^{143}Nd/^{144}Nd$					0·513015	0·513016	
$^{206}Pb/^{204}Pb$					18·6786	18·6730	
$^{207}Pb/^{204}Pb$					15·5326	15·5264	
$^{208}Pb/^{204}Pb$					38·286	38·268	
$^{176}Hf/^{177}Hf$					0·513015	0·513016	

(continued)

Table 1: Continued

Locality:	NW Rota-1 eastern flank		East Knoll			
Magma type:	POB					
Sample no.:	HPD488R17	HPD488R19	HPD951R02	HPD951R06	HPD951R08	HPD951R14
Latitude (N):	14°35·604′	14°35·615′	14°37·484′	14°37·455′	14°37·417′	14°37·281′
Longitude (E):	144°48·102′	144°48·085′	144°53·962′	144°53·928′	144°53·879′	144°53·709′
Depth (m b.s.l.):	1649	1629	2314	2267	2212	1992
wt %						
SiO_2	51·34	57·00	54·07	53·56	53·34	53·93
TiO_2	0·89	0·80	0·92	0·92	0·92	0·91
Al_2O_3	16·77	17·65	17·19	17·12	17·11	17·20
Fe_2O_3	9·00	7·42	10·62	10·84	10·82	10·64
MnO	0·15	0·16	0·18	0·18	0·18	0·18
MgO	7·68	3·69	3·35	3·45	3·46	3·38
CaO	11·15	8·10	8·58	8·69	8·67	8·60
Na_2O	2·43	3·46	2·81	2·73	2·70	2·82
K_2O	0·47	1·13	0·75	0·75	0·86	0·76
P_2O_5	0·15	0·21	0·16	0·16	0·16	0·16
Total	100·03	99·62	98·62	98·39	98·21	98·57
Trace elements (ppm) by XRF						
Ba	107·5	203·6	167·1	154·7	163·4	157·4
Ni	95·9	16·2			6·2	5·5
Cu	92·9	55·7	94·9	107·6	106·5	101·1
Zn	71·7	68·2	87·3	86·3	87·1	84·5
Pb		2·1	2·3	2·6		2·7
Th	0·7	1·8	1·2	0·6	1·2	0·9
Rb	9·1	22·5	12·8	12·0	14·3	12·2
Sr	315·3	405·3	324·4	322·7	324·5	326·8
Y	18·2	24·8	19·9	21·2	20·8	21·1
Zr	57·4	89·7	67·2	65·3	64·7	66·8
Nb	2·8	2·7	1·9	1·8	1·9	2·1
Trace elements (ppm) by ICP-MS						
V	285·5	198·0	284·9	302·5	325·6	334·5
Cr	291·95	47·98	2·24	8·30	2·09	3·17
Ni	105·5	21·0	7·57	8·02	8·26	5·03
Rb	7·57	22·60	11·44	11·48	13·03	11·55
Sr	319	381	325	340	327	335
Y	20·4	28·3	23·7	23·7	23·6	24·5
Zr	57·7	94·0	70·4	64·6	67·5	70·0
Nb	2·82	3·18	2·30	2·27	2·18	2·17
Cs	0·28	0·39	0·29	0·30	0·29	0·30
Ba	92·4	210·0	171·7	161·0	163·7	166·4
La	5·22	11·94	6·01	5·87	5·88	6·38
Ce	12·28	25·22	13·88	13·13	13·73	14·53
Pr	1·65	3·43	1·90	1·86	1·86	1·98
Nd	8·16	15·60	9·47	9·23	9·48	9·76
Sm	2·37	4·21	2·64	2·72	2·63	2·88
Eu	0·88	1·36	0·95	0·97	0·96	0·98
Gd	2·70	4·35	3·26	3·29	3·22	3·48
Tb	0·48	0·72	0·55	0·57	0·57	0·60
Dy	3·15	4·47	3·69	3·61	3·74	3·91
Ho	0·70	0·95	0·80	0·79	0·76	0·82
Er	2·02	2·75	2·29	2·33	2·29	2·38
Tm	0·30	0·41	0·37	0·36	0·36	0·38
Yb	1·94	2·85	2·32	2·24	2·34	2·31
Lu	0·30	0·44	0·35	0·34	0·34	0·37
Hf	1·45	2·45	1·83	1·80	1·79	1·86
Ta	0·150	0·179	0·163	0·151	0·149	0·168
Pb	1·37	2·73	2·10	2·04	2·01	2·12
Th	0·503	1·609	0·726	0·669	0·650	0·751
U	0·178	0·542	0·344	0·318	0·315	0·358
$^{87}Sr/^{86}Sr$		0·703235				
$^{143}Nd/^{144}Nd$		0·512978				
$^{206}Pb/^{204}Pb$		18·8377				
$^{207}Pb/^{204}Pb$		15·5498				
$^{208}Pb/^{204}Pb$		38·429				
$^{176}Hf/^{177}Hf$						

Table 2: Phenocryst assemblages and modal proportions (vol. %) of primitive basalts (Mg-number > 61 and MgO > 7·5 wt %)

Magma type:	Porphyritic basalts			POB					
Sample no.:	HPD480R1	HPD480R9	HPD480R10	HPD488R2	HPD488R10	HPD488R11	HPD488R12	HPD488R13	HPD488R17
Vesicle vol. %	12·2	19·3	22·5	21·7	18·4	30·9	29·3	14·6	7·7
Vol. % excluding vesicles									
Olivine	9·3	3·7	4·4	3·8	2·3	0·8	1·7	1·5	2·5
Plagioclase	16·1	19·0	20·5	1·9	1·0	0·8	+	0·6	1·4
Clinopyroxene	2·0	0·7	1·3	0·0	0·3	0·0	+	0·0	0·2
Groundmass	72·6	76·6	73·8	94·3	96·4	98·4	98·3	97·9	96·0

Magma type:	COB							
Sample no.:	HPD488R1	HPD488R3	HPD488R4	HPD488R5	HPD488R6	HPD488R7	HPD488R8	HPD488R9
Vesicle vol. %	18·4	11·5	21·5	12·3	21·4	10·9	19·2	24·4
Vol. % excluding vesicles								
Olivine	1·7	2·8	4·6	3·0	3·8	1·1	3·4	2·5
Plagioclase	0·0	0·2	0·1	0·0	0·2	0·0	0·1	0·0
Clinopyroxene	0·0	1·0	0·8	1·0	2·4	0·3	2·2	1·5
Groundmass	98·3	96·0	94·5	96·0	93·5	98·6	94·3	96·1

Modal proportions (vol. %) based on 4000–5000 points counts.

that the spectrum of sub-alkaline rocks be divided into high-, medium-, and low-Fe suites, complementing divisions made on the basis of K contents. On this basis, rocks from the eastern flank, the summit and the east knoll form low-Fe, medium-Fe and high-Fe suites, respectively. We focus here on NW Rota-1 primitive and near-primitive basalts, with Mg-number >61 (Fig. 2b), and use these compositions to understand the genesis of basaltic magmas in the mantle wedge. These basalts, however, are somewhat heterogeneous; for example, they have Zr/Y from 2·8 to 3·6 (Fig. 2b). These variations suggest that the mantle source is also compositionally variable or is variably melted, as has been shown for lavas from Sumisu and Torishima volcanoes in the Izu–Bonin arc, which have Zr/Y ranging from 1·4 to 2·2 (Tamura *et al.*, 2005, 2007).

TWO BASALT MAGMA TYPES
Cpx–olivine basalt (COB) and plagioclase–olivine basalt (POB)

Samples from HPD480 (summit) and HPD488 (eastern flank) include 17 magnesian basalts (51–52 wt % SiO_2) with 7·5–9·5 wt % MgO and Mg-number of 61–67, indicating little fractionation (Fig. 2). These magnesian basalts

are classified on the basis of their petrography into three groups: (1) cpx–olivine basalt (COB); (2) plagioclase–olivine basalt (POB); (3) porphyritic basalt (Fig. 3 and Table 2). The COB (eight samples from deeper part of HPD488) contain phenocrysts of augite (0–2·4%) and olivine (1·1–4·6%) sometimes with rare (<0·2%) plagioclase. The POB (six samples from shallower part of HPD488) have plagioclase (rare to 1·9%) and olivine (0·8–3·8%) phenocrysts with 0–0·3% clinopyroxene. The porphyritic basalts (three samples from HPD480) contain up to 9% olivine, 20% plagioclase, and 2% clinopyroxene (Table 2).

Most COB olivines are 0·5–1·0 mm across, rarely as large as 4 mm. In contrast, POB olivines are smaller (mostly <0·5 mm). COB clinopyroxenes and POB plagioclases range from 0·4 to 1·0 mm. Porphyritic basalts contain much coarser olivine, clinopyroxene and plagioclase phenocrysts up to 6 mm, 2 mm and 3 mm, respectively. Vesicularities (size and vol. % of vesicles) of COB and POB, on the other hand, do not differ systematically; vesicles up to 7 mm in size range from 10 to 24 vol. % in COB and from 8 to 30 vol. % in POB (Table 2). POB have higher Mg-number (63–67) than COB (61–65) at the same silica contents (Fig. 3). Magnesian POB cannot differentiate into COB via crystal
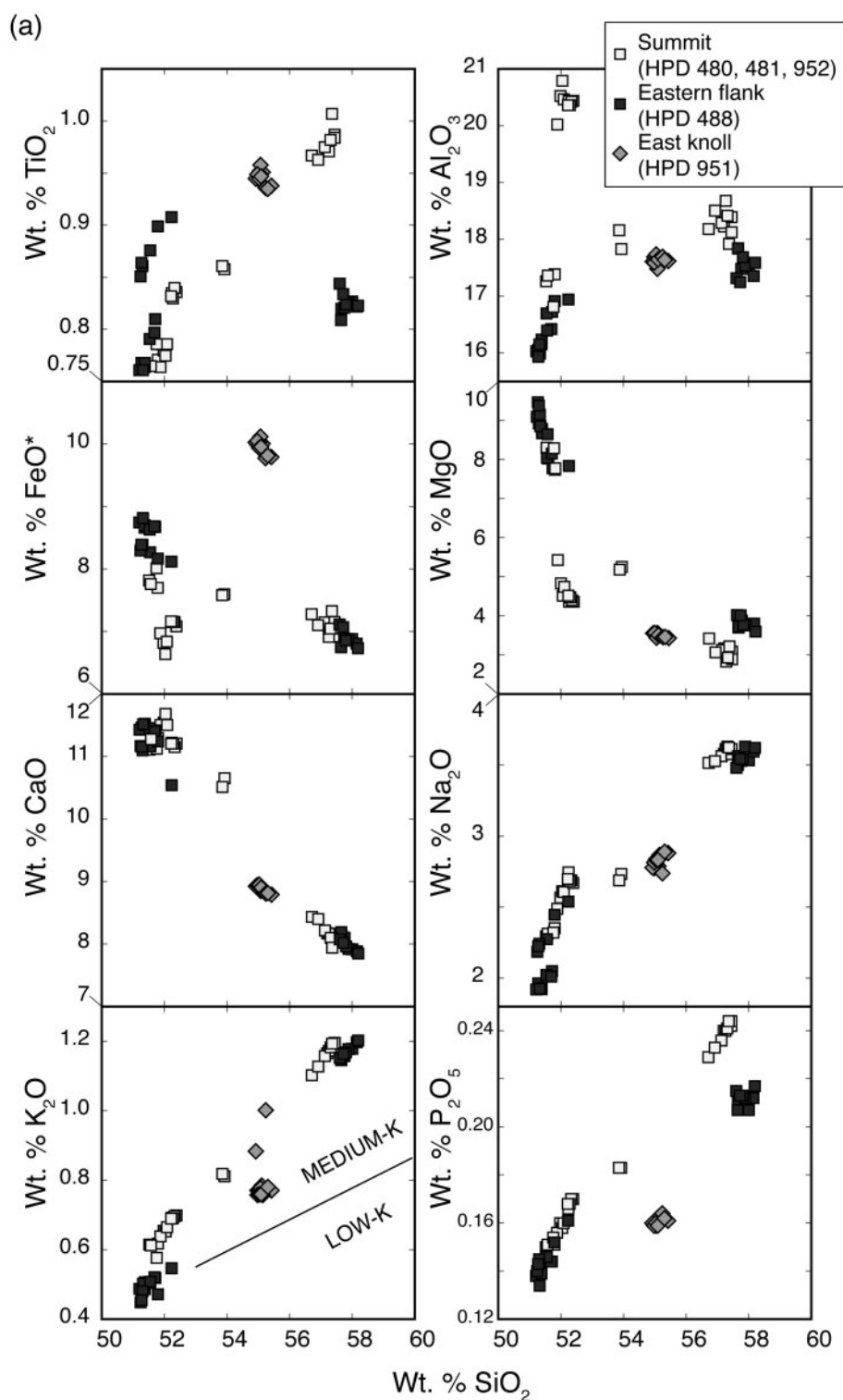
Fig. 2. SiO$_2$ variation diagrams of NW Rota-1 lavas and scorias, collected by ROV *Hyper-Dolphin*, from the summit (HPD 480, 481 and 952), eastern flank (HPD 488) and east knoll (HPD 951). Dive tracks are shown in Fig. 1c. (a) Variation diagrams of SiO$_2$ vs major element oxides (wt %). Medium- and low-K boundary after Gill (1981). (b) Variation diagrams of wt % SiO$_2$ vs Mg-number [100Mg/(Mg + ∑Fe)], FeO*/MgO and Zr/Y. The discriminant boundary (dashed line) between calc-alkaline and tholeiitic suites is from Miyashiro (1974). The discriminant boundaries (continuous lines) between low-, medium-, and high-Fe suites are from Arculus (2003). The rectangle in the upper diagram encompasses the most primitive basalts (Mg-number > 61 and MgO > 7·5 wt %); this is shown enlarged in Fig. 3.
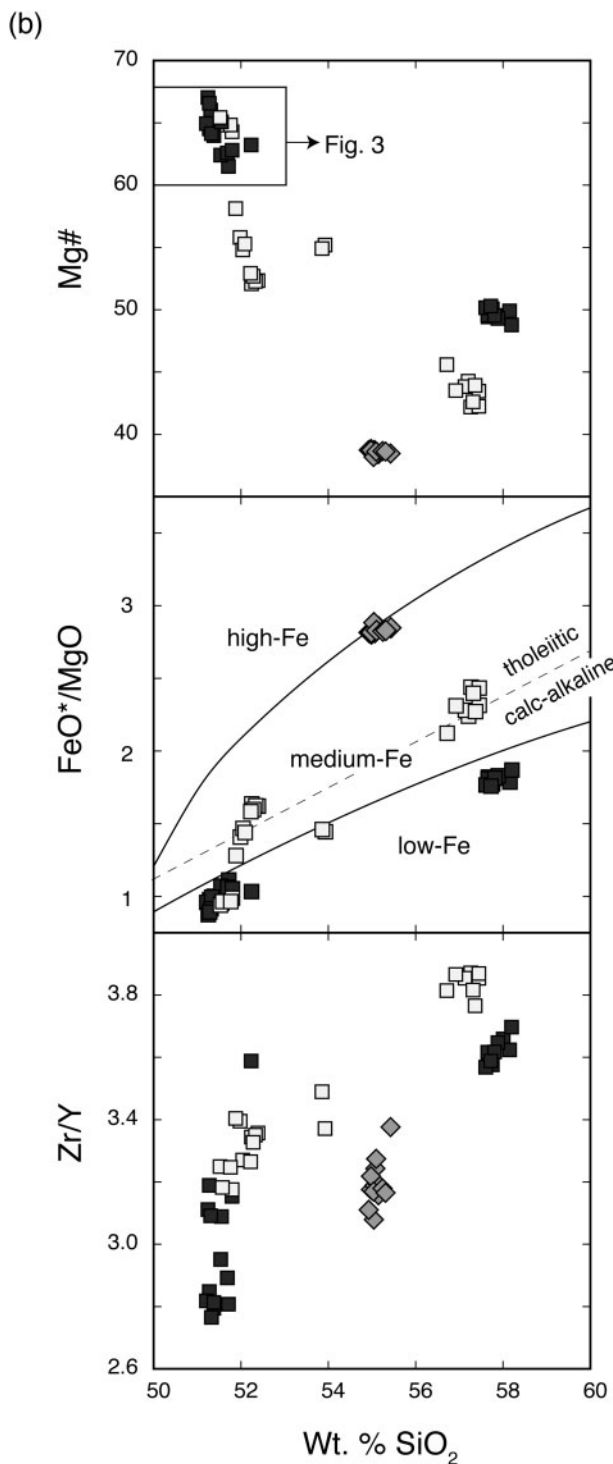
Fig. 2. Continued.

Major and trace elements of COB, POB, and porphyritic basalt from NW Rota-1 and primitive back-arc basin basalt from the Southern Mariana Trough

Figure 4 shows silica variation diagrams for major elements (Fig. 4a), trace elements and trace element ratios (Fig. 4b and c) among the POB, COB and porphyritic basalts from NW Rota-1 volcano from this study and near-primitive basaltic glasses with Mg-number >61 of BABB of the Southern Mariana Trough (SMT) from 15°N to 17°N (Gribble *et al.*, 1996; Pearce *et al.*, 2005). Primitive SMT BABB glasses range from 49·5 to 52 wt % SiO_2, but all NW Rota-1 primitive basalts are relatively SiO_2-rich (51−52·5 wt %).

TiO_2, Al_2O_3, K_2O and Na_2O increase with SiO_2 in both POB and COB. POB have distinctly higher TiO_2 and Na_2O and lower FeO* contents than COB (Fig. 4a). On the other hand, Al_2O_3, MgO and K_2O for the two groups overlap at the same SiO_2 content. Porphyritic basalts have higher Al_2O_3 and K_2O and lower FeO* than POB and COB, which could result from the accumulation of olivine, plagioclase and clinopyroxene in differentiated melts. Primitive BABB glasses have higher TiO_2, Al_2O_3 and Na_2O and lower FeO*, MgO and K_2O. Although some values overlap with those of POB and/or porphyritic basalt, K_2O contents of BABB (0·2–0·3 wt %) are distinctly lower than those of NW Rota-1 basalts (0·4–0·6 wt %).

Figure 4b shows the variation of Sr, Y, Zr, Nb, Ba, Hf and Th contents (measured by ICP-MS) and Zr/Y with SiO_2. POB have higher Y, Zr, Nb and Hf contents and lower Sr, Ba and Th contents compared with COB. Moreover, POB have higher Zr/Y than COB. Zr/Y is a proxy for mantle fertility and per cent melting as shown by Tamura *et al.* (2005, 2007), suggesting that the COB magmas could have resulted from a higher degree of partial melting of similar mantle to that which generated the POB. BABB glasses are more like POB in terms of the 'mantle fertility' indicators Y, Zr, Nb, and Hf, but have distinctly lower abundances of 'subduction component' indicators such as K_2O (Fig. 4a), Sr, Ba and Th (Fig. 4b) than either POB or COB.

Incompatible and compatible trace element abundances can be significantly modified by fractional crystallization and crystal accumulation in porphyritic basalts. Ba, Th and Nb are highly incompatible, behaving similarly during melting and crystallization, but only Ba is mobile in hydrous fluids. Ratios of incompatible trace elements are likely to be useful for inferring whether the porphyritic basalts are related to POB, COB, or neither. Figure 4c shows Nb/Yb, Ba/Nb, Th/Nb and Ba/Th vs SiO_2 content, and Fig. 4d shows Th/Nb vs Ba/Nb and Th/Nb vs Nb/Yb. Nb/Yb is a ratio of two fluid-immobile elements with different compatibilities and highlights mantle depletion (Pearce *et al.*, 2005). Ba/Nb, Th/Nb and Ba/Th highlight

fractionation, because plagioclase has no reaction relations with any other phase. Finding these two magma types coexisting within the same volcano is new in the Mariana arc.
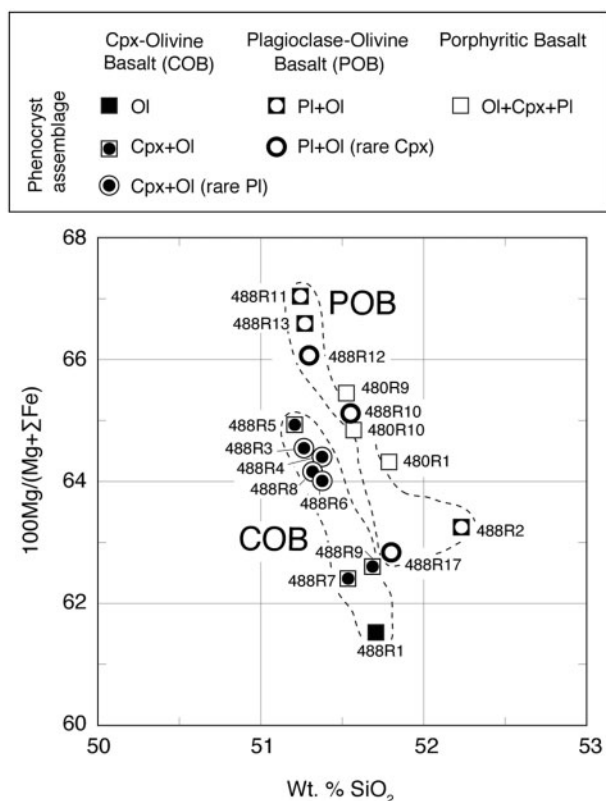
Fig. 3. Mg-number $[100Mg/(Mg + \sum Fe)]$ vs wt % SiO_2 for primitive basalts (Mg-number > 61 and MgO > 7·5 wt %). These basalts are classified into three types [plagioclase–olivine basalt (POB), cpx–olivine basalt (COB) and porphyritic basalt] based on the phenocryst assemblage and phenocryst content. (See Table 2 for modal analyses.)

subduction input; Ba/Nb proxies for total subduction addition, Th/Nb proxies for deep subduction addition (sediment melting) and Ba/Th is sensitive to shallow (hydrous fluid) subduction addition (Pearce *et al.*, 2005). Assuming that melting occurs in the spinel peridotite stability field, the lower Nb/Yb of COB relative to POB suggests greater depletion and/or higher degrees of melting of its source, which is consistent with variations in Zr/Y (Fig. 4b). Ba/Nb and Th/Nb variations suggest that COB have total and deep subduction additions that are larger than those for POB (Fig. 4c). These ratios partially reflect the lower abundance of Nb in COB relative to POB (Fig. 4b); however, the positive correlation between Th/Nb and Ba/Nb (Fig. 4d) emphasizes the importance of subduction addition in COB and porphyritic basalts. Ba/Th does not differ systematically between two magma types, but both Ba/Th and Ba/Nb are higher than in BABB, suggesting that the shallow subduction addition is equally important for COB and POB. Differences in mantle source depletion (Nb/Yb) are continuous between POB and COB, but subduction additions (Th/Nb and Ba/Nb) show a clear gap

between COB and POB (Fig. 4d). These incompatible element ratios also show that the porphyritic basalts are more akin to the COB. On the other hand, BABB are more similar to the POB in terms of Nb/Yb, Ba/Nb and Th/Nb, suggesting that subduction addition and degrees of melting in BABB and POB also might be lower than for COB (Fig. 4d).

Rare earth element (REE) patterns

Figure 5 shows chondrite-normalized REE plots for (a) COB and porphyritic basalt, (b) POB, (c) BABB from the Southern Mariana Trench (SMT) and (d) comparison of COB, POB and BABB REE patterns. NW Rota-1 basalts are more enriched in light REE (LREE; La, Ce, Pr and Nd) and middle REE (MREE; Sm, Eu, Gd, Tb and Dy) compared with heavy REE (HREE; Ho, Er, Tm, Yb and Lu). The chondrite-normalized patterns slope downwards from lanthanum (La) to dysprosium (Dy), but HREE from Ho to Lu have gentle slopes or are almost flat. The porphyritic basalts have steep patterns of LREE and MREE, which are parallel to COB REE patterns (Fig. 5a). The REE patterns suggest a close relationship between COB and porphyritic basalt, which was already shown by the trace element ratios (Fig. 4c). The BABB are four primitive glasses with Mg-number 61–65, which are shown in previous figures, and two most MORB-like glasses from D84 (Mg-number 54–55) (Gribble *et al.*, 1996; Pearce *et al.*, 2005). The REE patterns of the BABB, especially D84 (Fig. 5c), show contrasting LREE-depleted patterns. These LREE-depleted patterns are similar to those of Quaternary Izu arc front basalts, which are, however, not similar in terms of other parameters, such as Ba/Yb–Nb/Yb systematics (Yokoyama *et al.*, 2003; Tamura *et al.*, 2005, 2007; Ishizuka *et al.*, 2008).

Figure 5d shows that COB REE patterns are steeper than those of POB. Both magma types have similar concentrations of LREE, but COB contain much lower HREE abundances (Fig. 5c). The POB and primitive BABB have similar contents of HREE, but BABB contain much lower abundances of LREE, the extreme of which is shown by N-MORB-like sample D84 (Gribble *et al.*, 1996).

COB and POB MgO diagrams

Figure 6 shows MgO variation diagrams for COB and POB, which allow data to be normalized to 8 wt % MgO (Klein & Langmuir, 1987; Langmuir *et al.*, 2006). Arrows in the diagrams indicate model trend lines for olivine fractionation to illustrate the predicted slope of the process. Major element vs MgO diagrams show linear trends, parallel to olivine fractionation, that are mutually distinctive for COB and POB except for K_2O (Fig. 6a). Based on the phenocryst assemblages and contents (Table 2), these trends are deemed to have resulted mainly through olivine fractionation from two different primary magmas. SiO_2, TiO_2, Al_2O_3, Na_2O, K_2O and P_2O_5 increase with
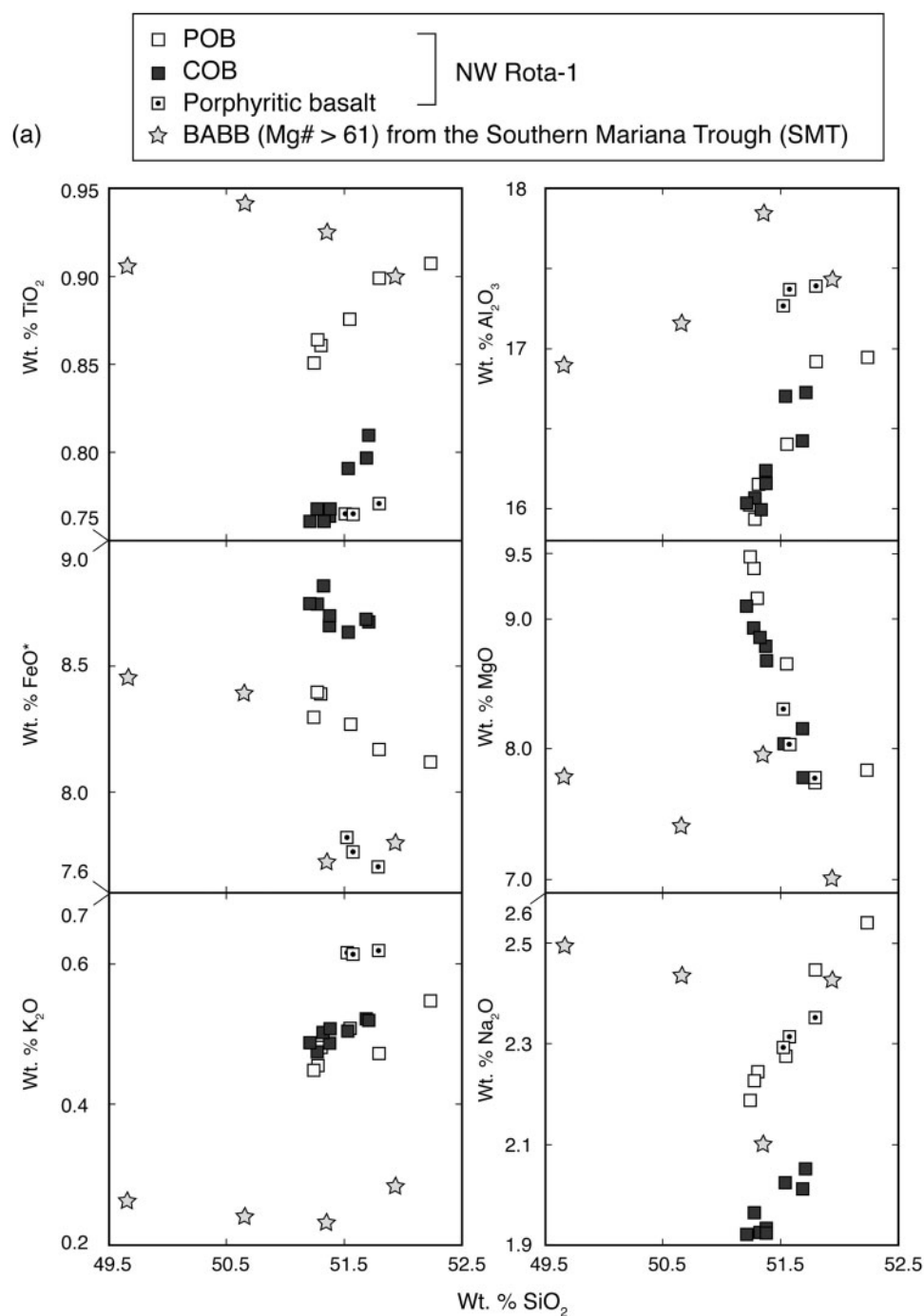
Fig. 4. Silica variation diagrams for primitive basalts from NW Rota-1 and the Southern Mariana Trough (SMT). Data for primitive back-arc basin basalts (BABB) from the SMT are from Gribble *et al.* (1996) and Pearce *et al.* (2005). (a) Variation diagrams of wt % SiO_2 vs major element oxides (wt %). (b) Variation diagrams of wt % SiO_2 vs selected trace elements (ppm) and Zr/Y. (c) Variation diagrams of wt % SiO_2 vs selected trace element ratios. Nb/Yb is a proxy for degree of melting; Ba/Nb a proxy for total subduction addition; Th/Nb a proxy for deep subduction addition and Ba/Th a proxy for shallow subduction addition (Pearce *et al.*, 2005). (d) Th/Nb vs Ba/Nb, Th/Nb vs Nb/Yb. The higher Th/Nb and Ba/Nb of the COB indicate that the COB contain greater abundances of slab-derived subduction components than the POB and BABB. Nb/Yb suggests that the degree of melting of the COB source is higher than for the POB and BABB.
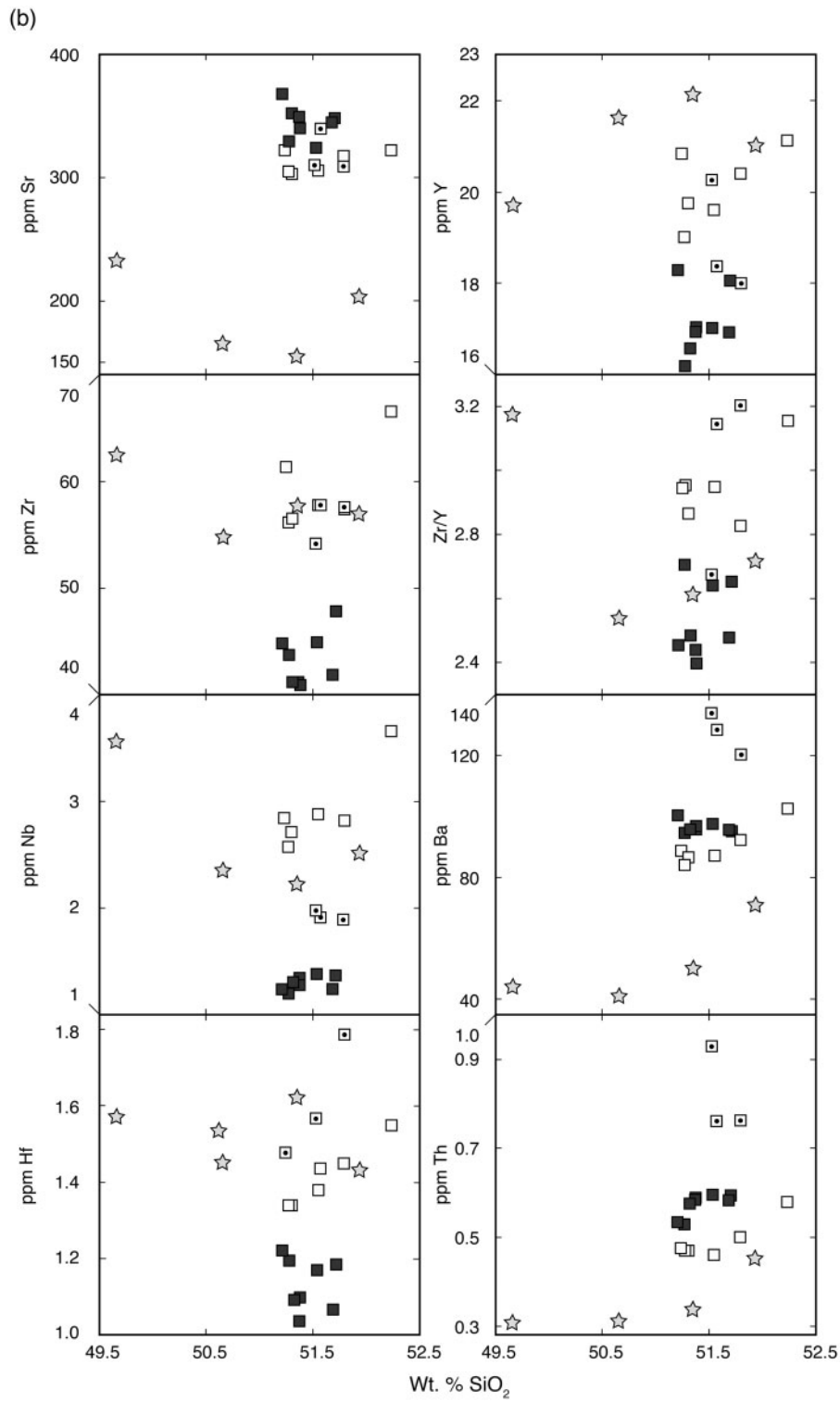
Fig. 4. Continued.
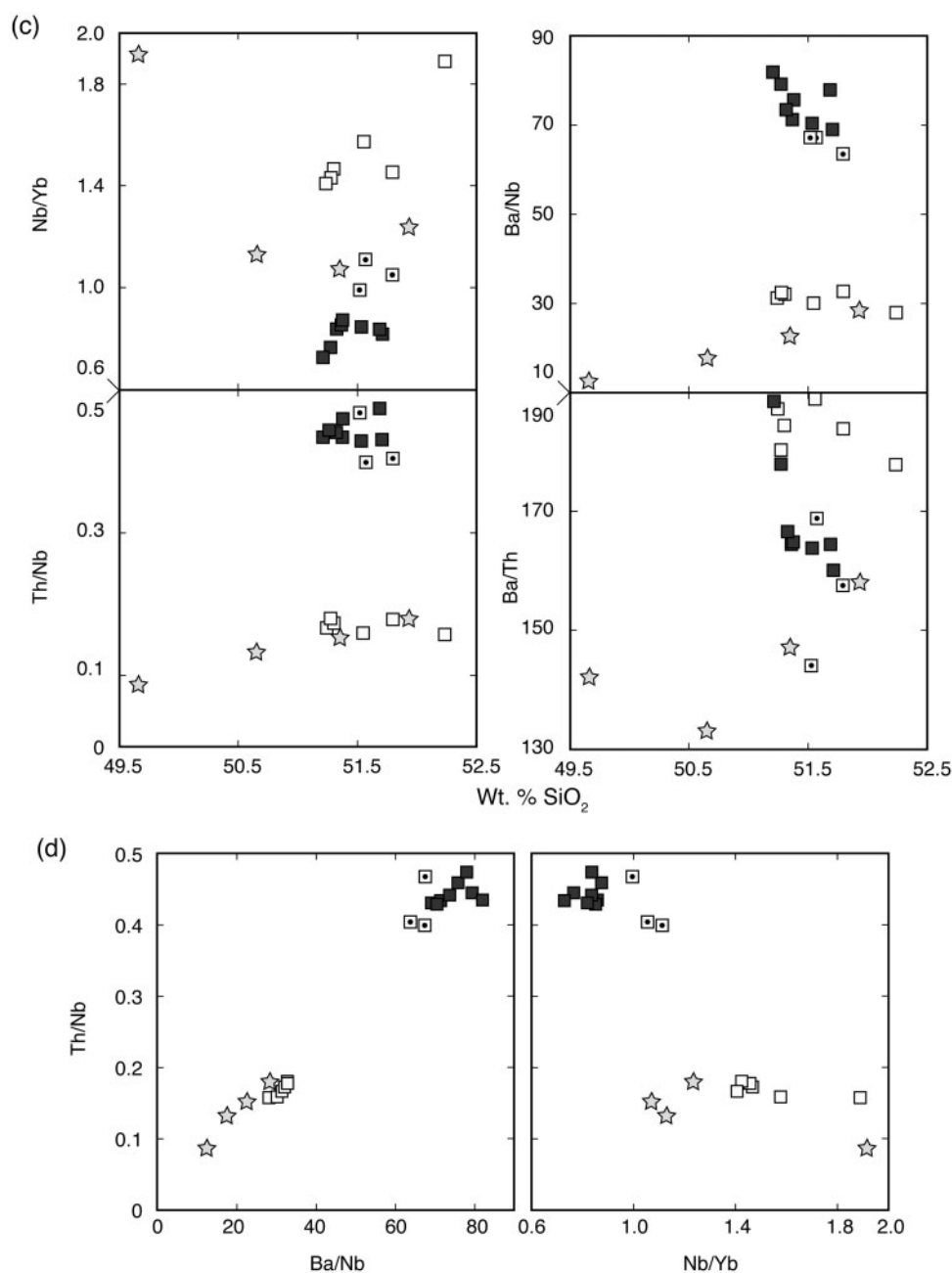
Fig. 4. Continued.

decreasing MgO for both COB and POB, and POB trends are higher in these elements for a given MgO content than COB except for K_2O (Fig. 6a). COB and POB show negative and overlapping trends on the K_2O–MgO diagram. Higher FeO* contents of COB compared with POB for a given MgO content are consistent with higher degrees of partial melting. As a consequence of this, POB have higher Mg-numbers than COB for a given MgO content. Thus, COB may be more differentiated than the

POB at 8 wt % MgO, suggesting that correcting to 8 wt % MgO may not indicate the same degrees of differentiation for melts in equilibrium with the source mantle. In fact, Mg-number should be calculated as $100\,Mg/(Mg + Fe^{2+})$, so the apparently lower Mg-number of COB at 8% MgO may reflect the fact that they are more oxidized magmas.

Figure 6b shows selected trace elements vs MgO content. Nb, Zr, Hf and Y contents are higher in POB than in
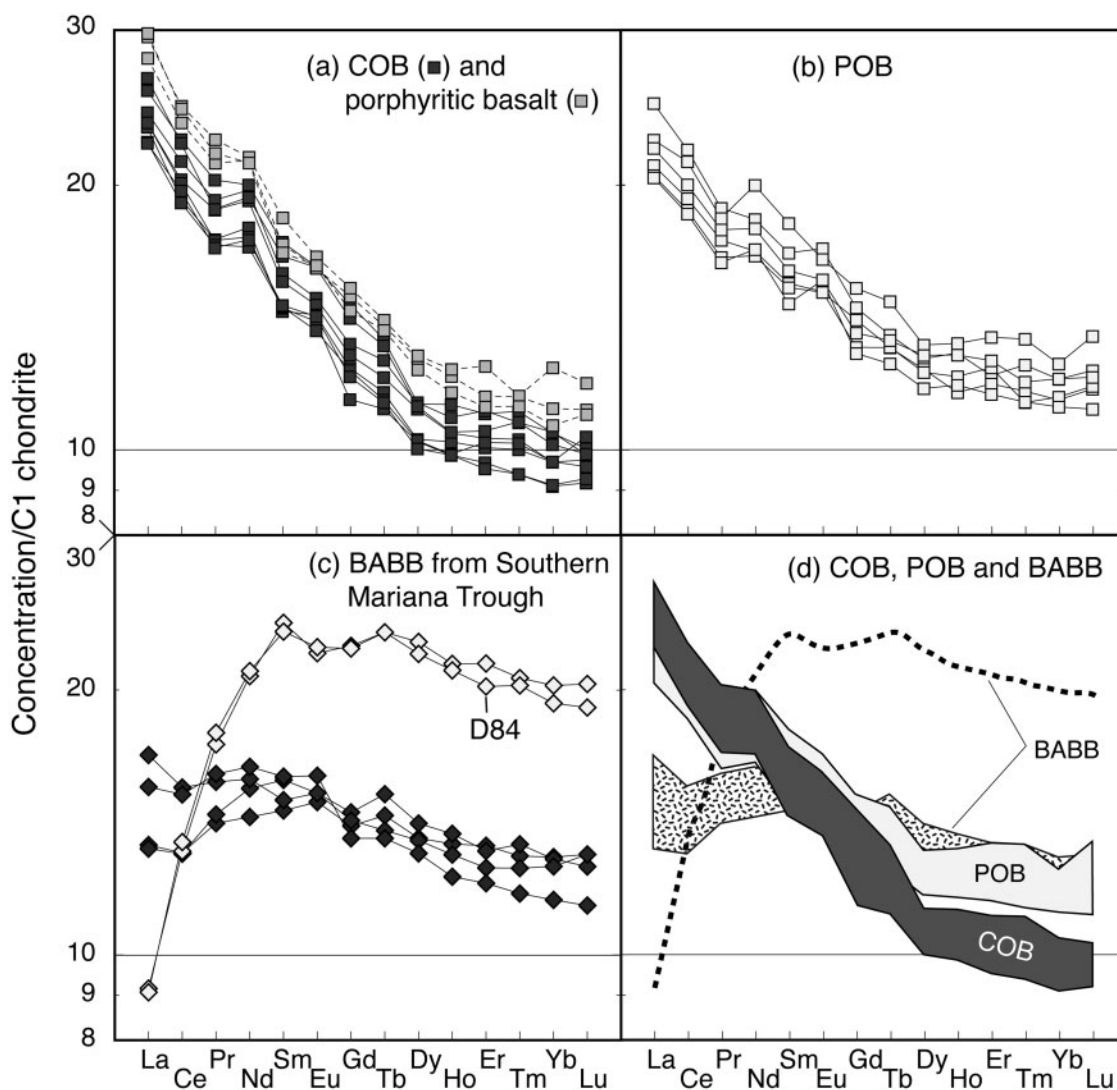
Fig. 5. REE patterns of primitive basalts from NW Rota-1 and the Southern Mariana Trough. (a) COB and porphyritic basalts. (b) POB. (c) BABB from the SMT, including four primitive glasses with Mg-number 61–65, and most MORB-like glasses from D84 (Mg-number 54–55) (Gribble *et al.*, 1996; Pearce *et al.*, 2005). (d) Comparison of COB, POB and BABB REE patterns; the first two groups are more strongly enriched in the LREE (La, Ce, Pr and Nd) and MREE (Sm, Eu, Gd, Tb and Dy) compared with the HREE (Ho, Er, Tm, Yb and Lu). C1 chondrite composition is that of McDonough & Sun (1995).

COB for a given MgO. POB and COB show distinct trends, parallel to olivine fractionation trends (Fig. 6b). On the other hand, Ba, Th, La and Sr, which are mostly added from subducted sediments and crust and are referred to as 'subduction components', are higher in COB than in POB. Interestingly, the Ba and Sr contents of COB do not increase as MgO decreases and thus seem independent of fractionation (Fig. 6b). It seems that the COB source is much more enriched in subduction components (K_2O, Ba, Th, La, Sr) than that of POB. Enrichments of these elements in the COB source may reflect recent introduction by hydrous metasomatic fluids or melts, which should have also caused more mantle melting

and thus systematic differences between COB and POB in terms of high field strength elements (HFSE) and major element compositions (Fig. 6). However, subduction component abundances are not uniform within the COB, so there must be a threshold of fluid- and subduction component-addition required to produce COB.

8 wt % MgO values

Figure 7 shows (a) MORB-normalized incompatible trace element patterns of eight COB and six POB, (b) MORB-normalized patterns for COB and POB corrected to 8% MgO (using the linear trends shown in Fig. 6), (c) $POB_{MgO=8}$ and (d) $COB_{MgO=8}$, highlighting
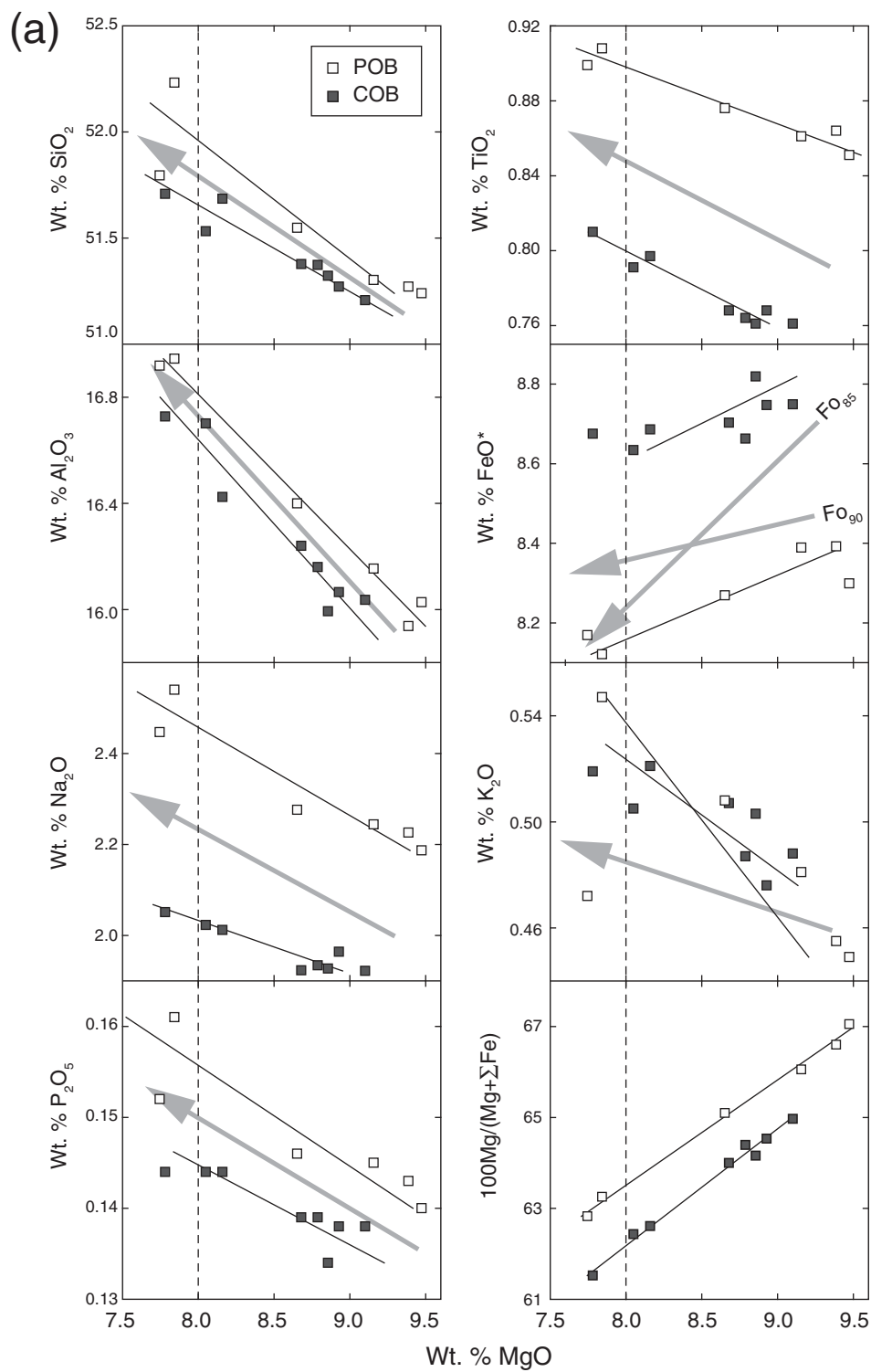
Fig. 6. MgO (wt %) variation diagrams for COB and POB from NW Rota-l. Linear regression lines through the COB and POB data are shown in each diagram. The arrows indicate model trend line for olivine fractionation. The points of intersection of the regression lines with the vertical dashed line (MgO = 8 wt %) determines the values normalized to 8 wt % MgO, which are shown in Fig. 7. (a) Variation diagrams of wt % MgO vs major elements oxides (wt %) and Mg-number [l00Mg/(Mg + $\sum$Fe)]. (b) Variation diagrams of wt % MgO vs selected trace elements (ppm).
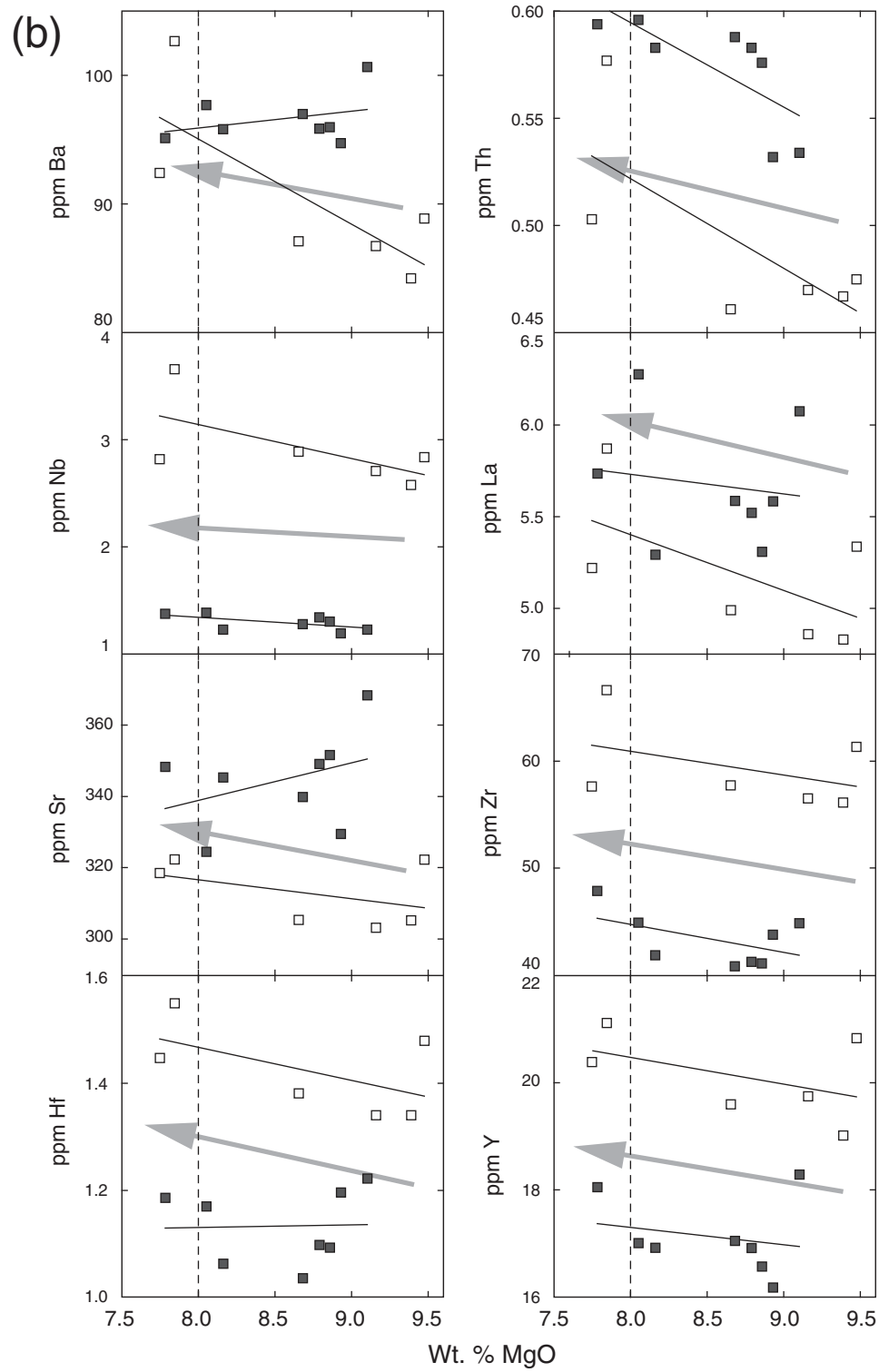
Fig. 6. Continued.
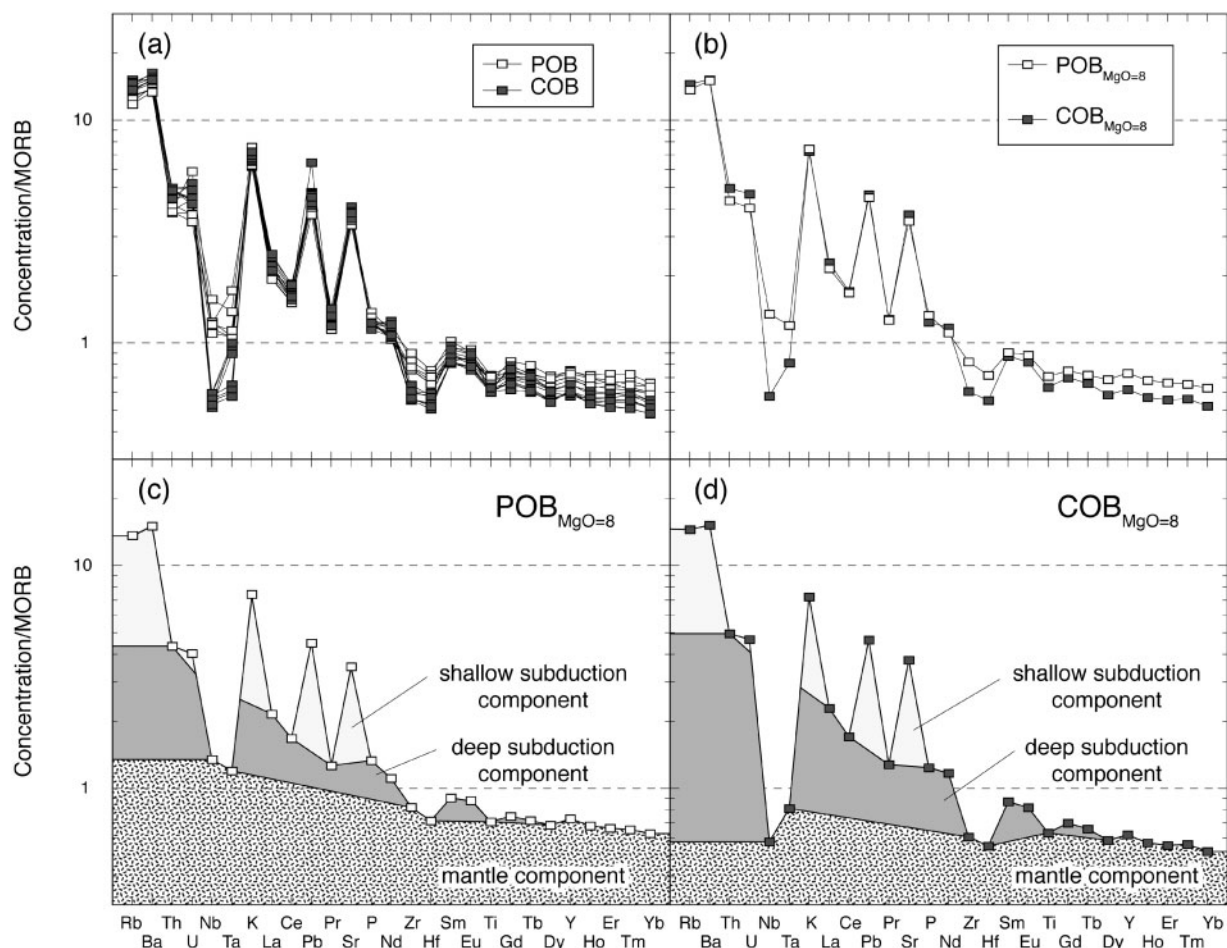
Fig. 7. MORB-normalized incompatible element patterns of (a) eight COB and six POB, (b) their corrections to a given concentration of MgO ($MgO = 8$ wt %) by using the linear trends shown in Fig. 6, (c) $POB_{MgO=8}$ and (d) $COB_{MgO=8}$ highlighting the distinctive mantle, deep subduction and shallow subduction components suggested by Pearce et al. (2005).

distinctive mantle, deep subduction and shallow subduction components as suggested by Pearce et al. (2005). In a given subduction system, shallow subduction input is characterized by elements such as Ba, Rb, Sr and Pb, which are mobile in low-temperature aqueous fluids. In contrast, deep subduction is characterized by source-region enrichments in both this group of elements as well as the group of melt-mobile incompatible elements including Th and LREE, which are mobile at higher temperature or as a result of sediment melting (Pearce et al., 2005). $COB_{MgO=8}$ are more enriched in the deep subduction component than $POB_{MgO=8}$. The shallow subduction component appears to be similar between $COB_{MgO=8}$ and $POB_{MgO=8}$. Lower TiO_2, Al_2O_3, Na_2O, P_2O_5, Zr, and Hf of COB compared with POB at $MgO = 8$ wt % in Fig. 6 also suggests that the COB are derived from a more depleted mantle source or by higher degrees of melting of a similar mantle source.

Sr–Nd–Pb–Hf isotopes

New Sr, Nd, Pb and Hf isotopic data for NW Rota-1 lavas are integrated with previously published data for the SMT (Gribble et al., 1996; Woodhead et al., 2001) and Mariana CIP (Fig. 8; Woodhead, 1989; Elliott et al., 1997; Woodhead et al., 2001; Wade et al., 2005; Stern et al., 2006). NW Rota-1 samples plot at the high $^{87}Sr/^{86}Sr$ and high $^{206}Pb/^{204}Pb$ ends of arrays formed by SMT lavas, or the lowest $^{87}Sr/^{86}Sr$ and lowest $^{206}Pb/^{204}Pb$ ends of the Mariana CIP arrays (Fig. 8a), as is expected for magmas that formed behind the magmatic front. NW Rota-1 lavas show a negative trend on the $^{143}Nd/^{144}Nd$–$^{87}Sr/^{86}Sr$ diagram and a gentle positive slope on the $^{206}Pb/^{204}Pb$–$^{207}Pb/^{204}Pb$ diagram, both of which are different from Mariana CIP arrays. Positive co-variation of Sr and Nd isotopic compositions is characteristic of arc cross-chains (e.g. Ishizuka et al., 2003; Stern et al., 2006;
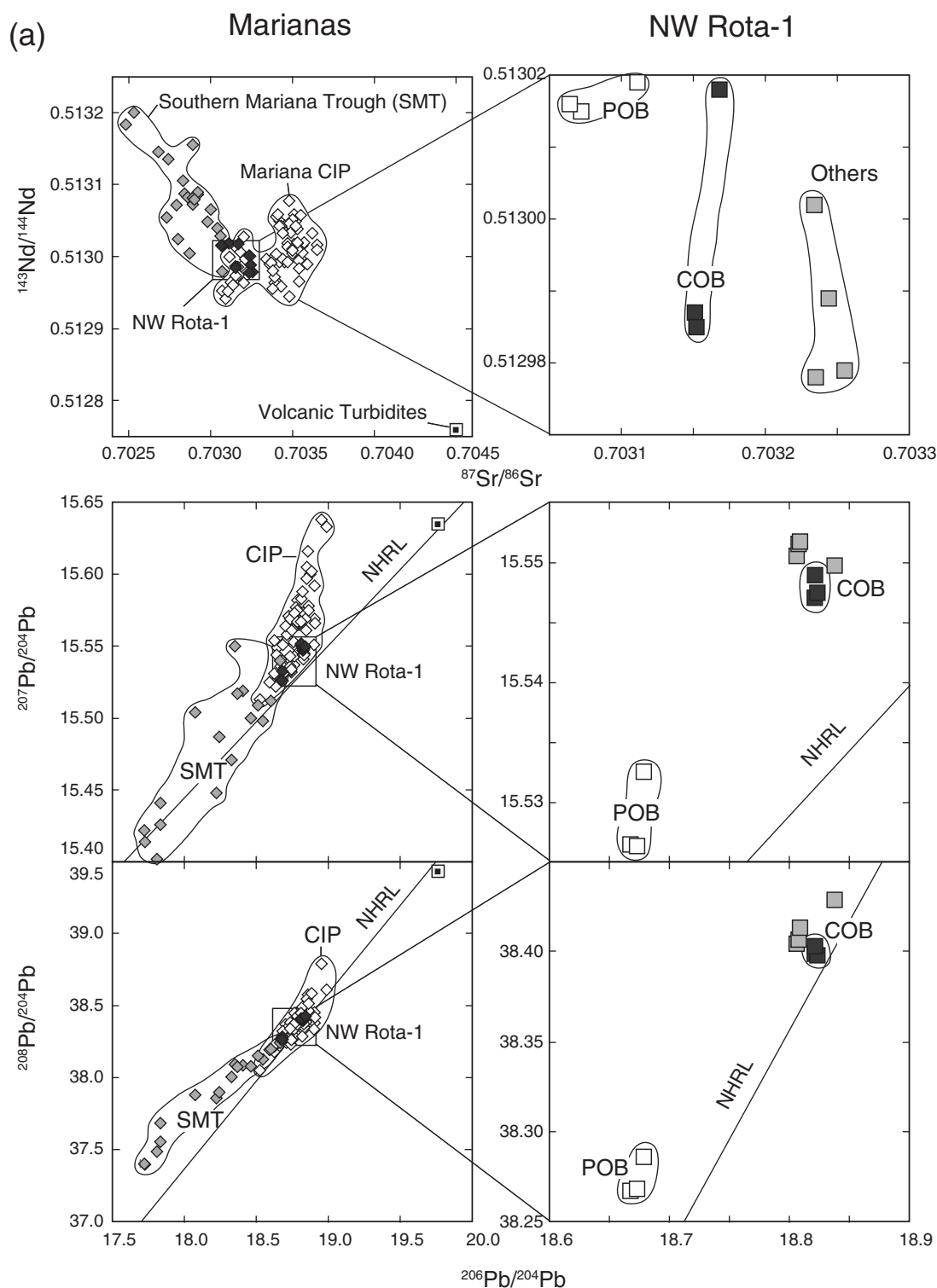
Fig. 8. (a) Sr–Nd–Pb isotope variation in NW Rota-l, Southern Mariana Trough (SMT) and Mariana CIP lavas. The 'Northern Hemisphere Reference Line' of Hart (1984; NHRL) is indicated by a continuous line in the Pb–Pb plots. Data for the SMT are from Gribble *et al.* (1996) and data for the Mariana CIP are from Woodhead (1989), Elliott *et al.* (1997), Wade *et al.* (2005) and Stern *et al.* (2006). Cretaceous OIB-derived volcanic turbidites represent those being subducted beneath the Mariana arc (Plank & Langmuir, l998). The field labelled 'Others', from NW Rota-l, is for less magnesian basalts (480R6 and 481R1) and andesites (481R6 and 488R19). (b) $^{176}Hf/^{177}Hf$ vs $^{143}Nd/^{144}Nd$ for NW Rota-l, SMT and Mariana CIP lavas. Dashed line shows the Indian–Pacific boundary line of Pearce *et al.* (1999). NW Rota-l basalts are less Indian-plate like than CIP lavas. Data for the SMT and Mariana CIP are from Woodhead *et al.* (2001) and Wade *et al.* (2005). In contrast to $^{87}Sr/^{86}Sr$, $^{143}Nd/^{144}Nd$, $^{206}Pb/^{204}Pb$, $^{207}Pb/^{204}Pb$ and $^{208}Pb/^{204}Pb$, $^{176}Hf/^{177}Hf$ values show no systematic differences between COB and POB.
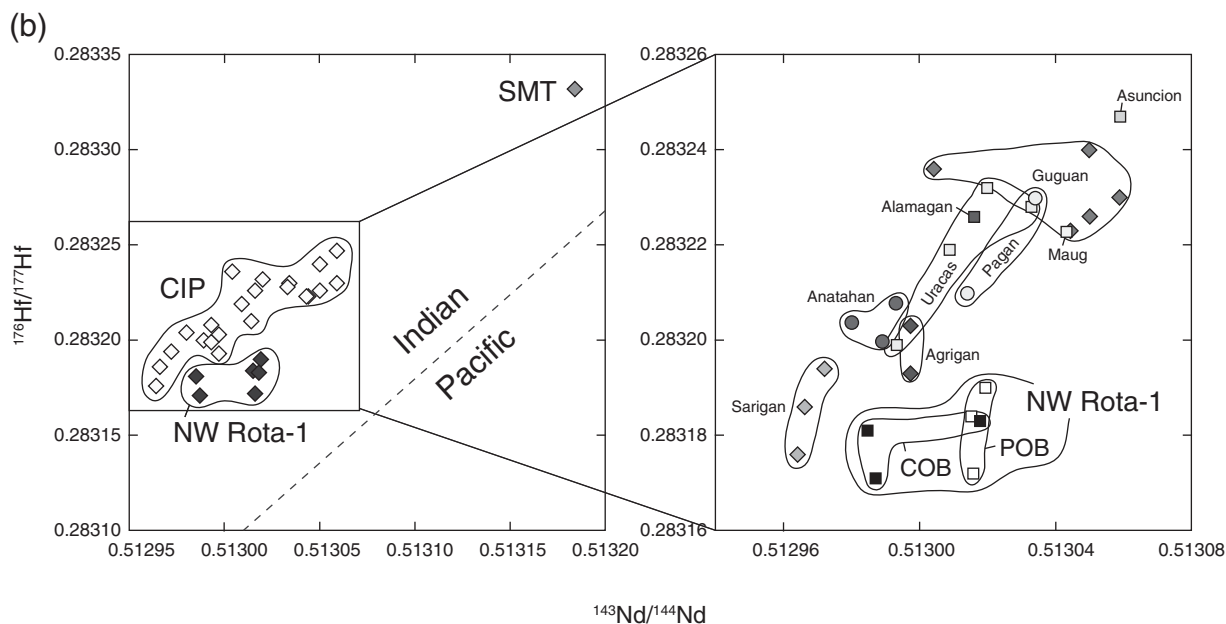
Fig. 8. Continued.

Tollstrup *et al.*, 2010), which is opposite to the observed negative co-variation for the NW Rota-1 and the SMT. The steep array on $^{206}Pb/^{204}Pb$–$^{207}Pb/^{204}Pb$ diagrams formed by the Mariana CIP is consistent with mixing between Pacific MORB-like Pb and bulk sediment Pb (Wade *et al.*, 2005). However, the arrays formed by the SMT and NW Rota-1 on $^{206}Pb/^{204}Pb$–$^{208}Pb/^{204}Pb$ diagrams are consistent with mixing between Indian Ocean MORB and magmatic front melts and/or with subducted Cretaceous ocean island basalt (OIB)-derived volcanic turbidites.

There are systematic isotopic differences between NW Rota-1 POB and COB. $^{87}Sr/^{86}Sr$, $^{206}Pb/^{204}Pb$, $^{207}Pb/^{204}Pb$ and $^{208}Pb/^{204}Pb$ of POB are lower than for COB and are more similar to the SMT. $\Delta7/4$ and $\Delta8/4$, which measure the vertical distance of samples from the Northern Hemisphere Reference Line of Hart (1984), also show that COB have higher $\Delta7/4$ and lower $\Delta8/4$ than POB. Isotopically, POB are more 'BAB-like' (i.e. lower $^{87}Sr/^{86}Sr$ and higher $\Delta8/4$) and COB are more 'arc-like' (i.e. higher $^{87}Sr/^{86}Sr$, higher $\Delta7/4$), which is consistent with their trace element ratios (Fig. 4d).

The new Hf and Nd isotope data for NW Rota-1 samples are plotted in Fig. 8b together with results for SMT and Mariana CIP lavas (Woodhead *et al.*, 2001; Wade *et al.*, 2005). Unfortunately, only one $^{176}Hf/^{177}Hf$ value, which is the most depleted in the SMT, has been published by Woodhead *et al.* (2001). Thus we cannot discuss the relationship among SMT, Mariana CIP and NW Rota-1 in terms of $^{176}Hf/^{177}Hf$. As the $^{143}Nd/^{144}Nd$ values of SMT overlap with those of Mariana CIP and NW Rota-1 as shown in

Fig. 8a, the SMT $^{176}Hf/^{177}Hf$ variation is certainly interesting.

Single Mariana CIP volcanoes and NW Rota-1 have distinct Nd–Hf isotopic compositions. Asuncion is the most radiogenic and Sarigan the least among the CIP volcanoes, which show positive correlation (Woodhead *et al.*, 2001). Samples from NW Rota-1 are out of the alignment. The dashed line in Fig. 8b shows the Indian–Pacific boundary line of Pearce *et al.* (1999). NW Rota-1 basalts are less Indian-like than the CIP lavas. In contrast to $^{87}Sr/^{86}Sr$, $^{143}Nd/^{144}Nd$, $^{206}Pb/^{204}Pb$, $^{207}Pb/^{204}Pb$ and $^{208}Pb/^{204}Pb$, $^{176}Hf/^{177}Hf$ values show no systematic differences between COB and POB.

MINERAL CHEMISTRY
Olivine

Sato (1977) pointed out that olivines crystallizing from primary magmas should have ~0·4 wt % NiO because this is reported in olivines from upper-mantle lherzolites. Although abyssal peridotite olivines contain 0·22–0·4 wt % NiO (Dick, 1989), current understanding of mantle wedge lithosphere suggests that ~0·4 wt % NiO is a useful approximation for mantle wedge olivines (e.g. Tamura *et al.*, 2000; Ionov, 2010; Fig. 9a). Figure 9a shows a tight clustering of NiO vs Fo contents for olivines from peridotite xenoliths (Avacha volcano, a Kamchatka arc volcano; Ishimaru *et al.*, 2007; Ionov, 2010), and IBM mantle wedge peridotites (Torishima forearc seamount and Conical seamount) recovered by Ocean Drilling Program Leg 125 (Ishii *et al.*, 1992; Parkinson & Pearce,
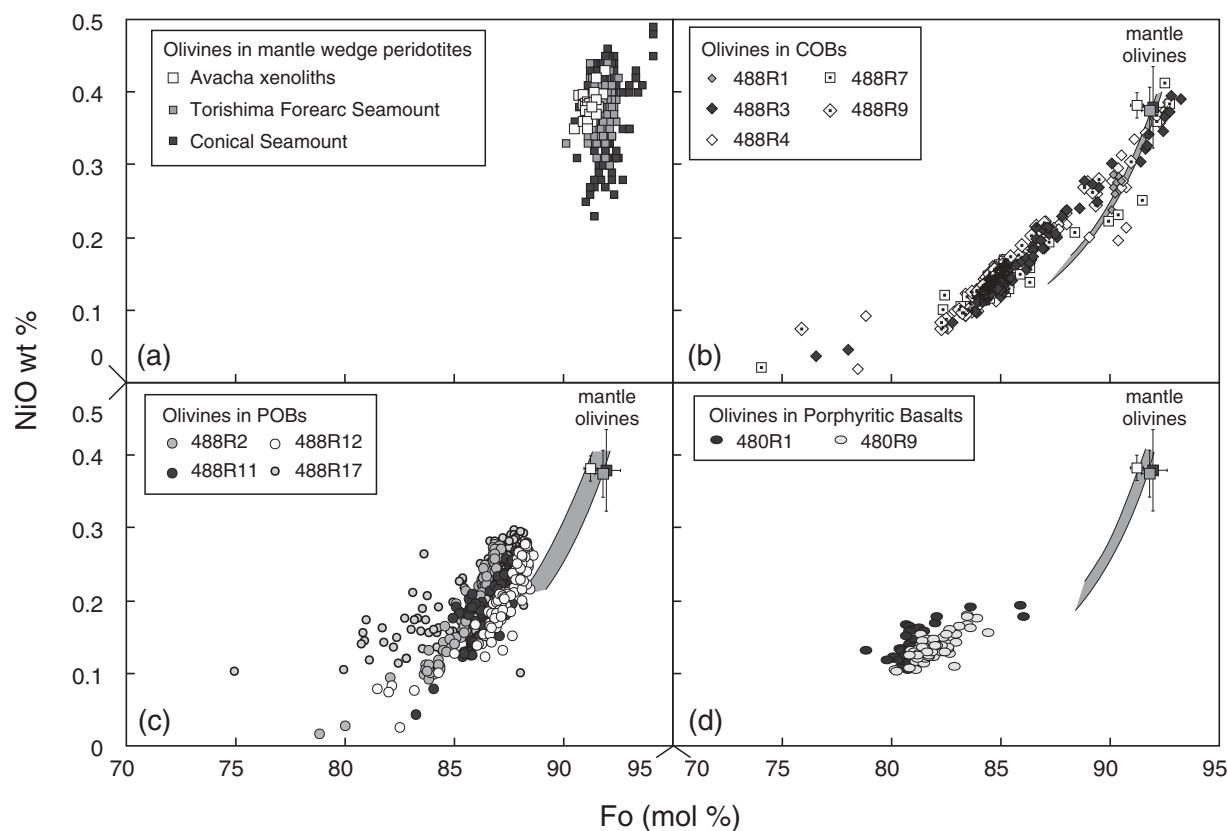
Fig. 9. Variation of NiO wt % vs Fo mol % [100Mg/(Mg + Fe)] for olivines in mantle wedge peridotites and olivine phenocrysts in NW Rota-1 primitive basalts. (a) Olivines from peridotite xenoliths from Avacha volcano, Kamchatka (Ionov, 2010) and serpentinized peridotites recovered by Ocean Drilling Program (ODP Leg 125) from Torishima forearc seamount and Conical seamount of the Izu–Bonin–Mariana arc (Ishii *et al.*, 1992). Average Fo ± 1SD of olivines from Avacha, Torishima forearc seamount and Conical seamount are $Fo_{91\cdot2\pm0\cdot3}$, $Fo_{91\cdot8\pm0\cdot4}$ and $Fo_{92\cdot0\pm0\cdot6}$, respectively and average wt % NiO of these olivines are $0\cdot38\pm0\cdot02$, $0\cdot38\pm0\cdot03$ and $0\cdot38\pm0\cdot06$, respectively, and these are shown in (b)–(d) as 'mantle olivines'. (b) COB olivines. The most magnesian olivines in these basalts are similar to the mantle olivines, representing those crystallized from primary COB magmas. Lines are olivine fractionation trends determined for COB. (c) POB olivines. Lines are olivine fractionation trends determined for POB. (d) Porphyritic basalt olivines, with olivine fractionation trends (curved lines). Observed olivines from the porphyritic basalts are iron-rich and thus more fractionated than the calculated equilibrium olivines.

1998). Mean Fo ± 1 SD contents of olivines from Avacha, Torishima forearc seamount and Conical seamount are $Fo_{91\cdot2\pm0\cdot3}$, $Fo_{91\cdot8\pm0\cdot4}$ and $Fo_{92\cdot0\pm0\cdot6}$, respectively and average $0\cdot38\pm0\cdot02$, $0\cdot38\pm0\cdot03$ and $0\cdot38\pm0\cdot06$ wt % NiO, respectively (Fig. 9a).

Magnesian basalts (Mg-number >60) from NW Rota-1 volcano contain olivine phenocrysts (1–10 vol. %), with rare Cr-spinel inclusions (Table 2). Cores and rims of 20–30 olivine phenocrysts from each of five COB, four POB and two porphyritic basalts were measured by electron microprobe. NiO contents correlate with Fo content [Fo = olivine 100 Mg/(Mg + Fe)], suggesting olivine fractionation. Fo contents of COB olivines range from 74 to 93, the most magnesian of which ($Fo_{91–93}$) contain ∼0·4 wt % NiO, indistinguishable from mantle olivines (Fig. 9b). POB olivines are more differentiated than those from COB ($Fo_{<89}$ and <0·3 wt % NiO; Fig. 9c), tending to be more iron-rich at the same NiO contents.

Gray shaded fields in Fig. 9b–d are trends of olivine fractionation calculated from lava bulk compositions, as described by Tamura *et al.* (2000), assuming that the ratio of oxidized iron to total iron [$Fe^{3+}/\sum Fe = Fe^{3+}/(Fe^{2+} + Fe^{3+})$] in NW Rota-1 basalt melts was 0·2. Kelley & Cottrell (2009) measured $Fe^{3+}/\sum Fe$, using Fe K-edge micro-X-ray absorption near-edge structure (μ-XANES) spectral analysis, and pre-eruptive magmatic H_2O contents of primitive undegassed basaltic glasses and melt inclusions. The $Fe^{3+}/\sum Fe$ ratio increases from MORB (0·13–0·17) to BABB (0·15–0·19) to arc samples (0·18–0·32) (Kelley & Cottrell, 2009). We assume that $Fe^{3+}/\sum Fe$ in the melt was 0·2, because the calculated trends are toward mantle wedge olivines (Fig. 9) and the value falls within arc samples. However, the oxidation state of Fe of COB and POB may not be the same if the oxidation state increases linearly with magmatic H_2O concentrations (Kelley & Cottrell, 2009). Some Fo-rich COB olivines are
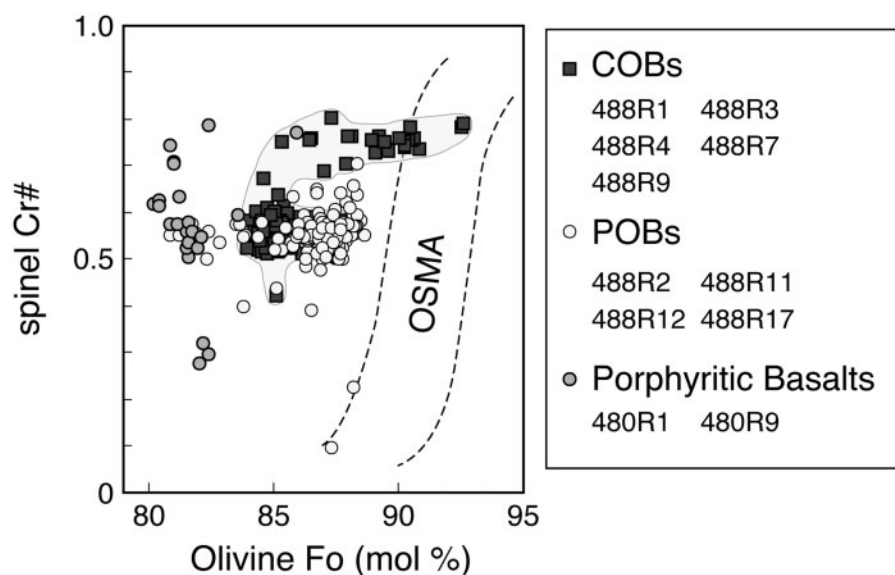
Fig. 10. Relationships between olivine Fo contents and spinel Cr-number in COB, POB and porphyritic basalts of NW Rota-1 volcano. OSMA (olivine–spinel–mantle array) represents the trend of residual spinel peridotites (Arai, 1994). The most magnesian olivine–spinel pairs from the COB lie within the OSMA, suggesting that these are from the primary magma in equilibrium with mantle peridotite.

more magnesian than the calculated trends, which suggest $Fe^{3+}/\sum Fe > 0.2$; meanwhile, many POB olivines are more iron-rich than the calculated trends. The latter suggests that $Fe^{3+}/\sum Fe < 0.2$ or the effect of supercooling has resulted in iron-rich olivines as shown by Tamura *et al.* (2000). Generally, however, COB and POB have olivine compositions that follow the calculated trends using $Fe^{3+}/\sum Fe = 0.2$ (Fig. 9b and c). Moreover, $Fe^{3+}/\sum Fe$ does not always correlate with the wt % H_2O of olivine-hosted melt inclusions from arc volcanoes (Kelley & Cottrell, 2009). Thus, we use $Fe^{3+}/\sum Fe = 0.2$ as a tentative value and further studies are planned to determine the oxidation state and actual H_2O content of melt inclusions from the NW Rota-1 volcano. Olivines in porphyritic basalts are relatively Fe-rich (Fo_{80-85}) and do not overlap calculated olivine fractionation trends (Fig. 9d). This suggests that the olivines in the porphyritic basalts are not in equilibrium with their host-rock compositions, perhaps because of the high phenocryst contents (Table 2).

Spinel

Figure 10 shows the relationship between the Fo contents of olivine and Cr-number [$=Cr/(Al + Cr)$ atomic ratio] of spinel in NW Rota-1 lavas. Primitive lavas should have olivine and spinel compositions that are similar to the olivine–spinel mantle array (OSMA), which represents the spinel peridotite residual trend (Arai, 1994). The Cpx/(Opx + Cpx) ratio also reflects the fertility of spinel peridotite, decreasing from lherzolites (>0.1) to harzburgite (<0.1) (Arai, 1994). This change accompanies increases of both olivine Fo and Cr-number of chromian spinel towards

the refractory (high-Fo, high-Cr-number) end of the OSMA. Cr-number $= 0.5-0.6$ approximates the boundary between fertile lherzolites and depleted harzburgite (Arai, 1994). Several pairs of COB magnesian olivines and chromian spinels plot in the high Fo (Fo_{90-93}) and high Cr-number ($0.7-0.8$) part of the OSMA, suggesting equilibrium with harzburgitic residual mantle. Some porphyritic basalt spinels also have high Cr-numbers similar to COB, but their olivines have lower Fo contents. No POB olivine–spinel pairs plot within the OSMA although their bulk Mg-numbers are higher than those of COB (Fig. 3).

The primitive nature of NW Rota-1 lavas is shown by the similarity of their spinel Cr-numbers to those from mantle wedge peridotites. Spinel compositions for NW Rota-1 lavas (COB, POB and porphyritic basalt) and those in peridotites from Conical and Torishima forearc seamounts (Ishii *et al.*, 1992) and mantle xenoliths of Avacha volcano in the Kurile arc (Ishimaru *et al.*, 2007; Ionov, 2010) are compared in Fig. 11. NW Rota-1 spinels have Cr-numbers with modes of $0.5-0.6$ (Fig. 11a). As mentioned above, COB and porphyritic basalts have more Cr-rich spinels (Cr-number $= 0.59 \pm 0.08$ and 0.57 ± 0.13, respectively) than POB (Cr-number $= 0.55 \pm 0.05$) (Fig. 11a). IBM forearc peridotites (Conical and Torishima seamounts) contain spinels with Cr-numbers like those of the NW Rota-1 basalts ($0.5-0.6$) (Fig. 11b). Cr-numbers of Conical seamount spinels (0.61 ± 0.14) are more variable than those of Torishima seamount (0.57 ± 0.05) and the maximum reaches ~0.9. Peridotite xenoliths of Avacha volcano have chromian spinels with Cr-number of $0.5-0.8$, averaging 0.61 ± 0.04.
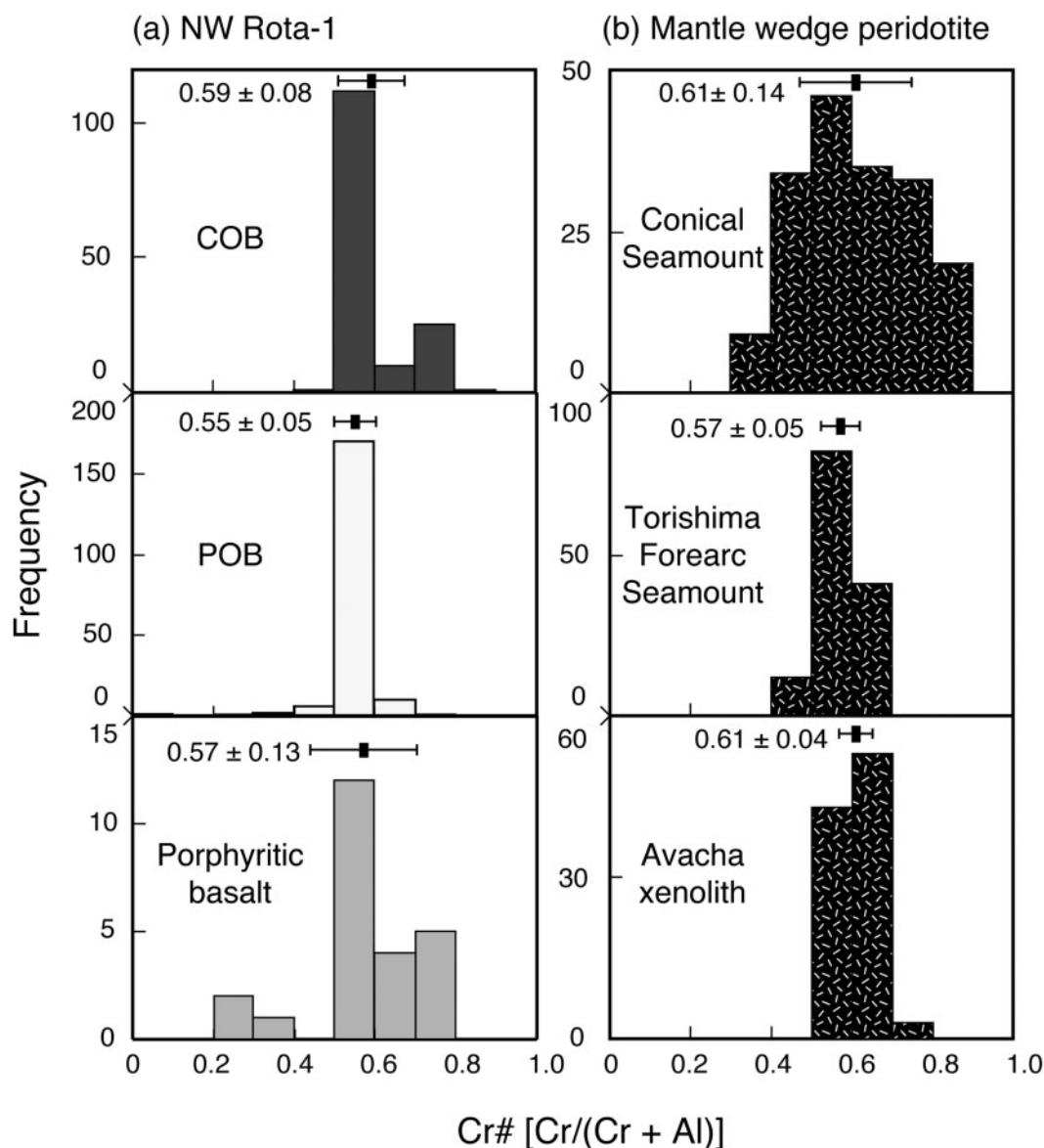
Fig. 11. Frequency distribution diagrams for spinel Cr-numbers [Cr/(Cr +Al) atomic ratio] from (a) primitive basalts (COB, POB and por-phyritic basalts) of NW Rota-1 volcano and (b) mantle wedge peridotites from Conical and Torishima Forearc seamounts of the Izu–Bonin–Mariana forearc, and those from mantle peridotite xenoliths from Avacha volcano, Kamchatka. An average ± 1 SD Cr-number is shown in each diagram.

Clinopyroxene and plagioclase

Figure 12 shows frequency diagrams of the Mg-number [100Mg/(Mg + Fe) atomic ratio] of augite phenocrysts in COB and anorthite content [An; 100Ca/(Ca + Na) atomic ratio] of plagioclase phenocrysts in POB. Compositions of both phenocrysts in the porphyritic basalts are also com-pared. Mg-numbers of augite in COB range from 80 to 88. Augite in the porphyritic basalts is more iron-rich (mean Mg-number = 8l). Anorthite contents of plagioclase from POB are mostly An_{76-82} whereas porphyritic basalt plagioclase is significantly more calcic, mostly An_{80-90}, with some up to An_{96} (Fig. 12).

Based on phenocryst modes and assemblages (Fig. 3 and Table 2), the crystallization sequence of COB magmas is spinel + olivine, spinel + olivine + cpx, and finally spi-nel + olivine + cpx + plagioclase. In contrast, POB magmas crystallize spinel + olivine, spinel + olivine + plagioclase, and finally spinel + olivine + cpx + plagio-clase. At first glance, it might appear that the porphyritic basalts could be derived from either the COB or the POB magmas. However, plagioclases in the porphyritic basalts have higher An contents than in POB (Fig. l2), which is in-consistent with fractionation of POB to yield the porphy-ritic basalts. Plagioclase appears after augite in the course
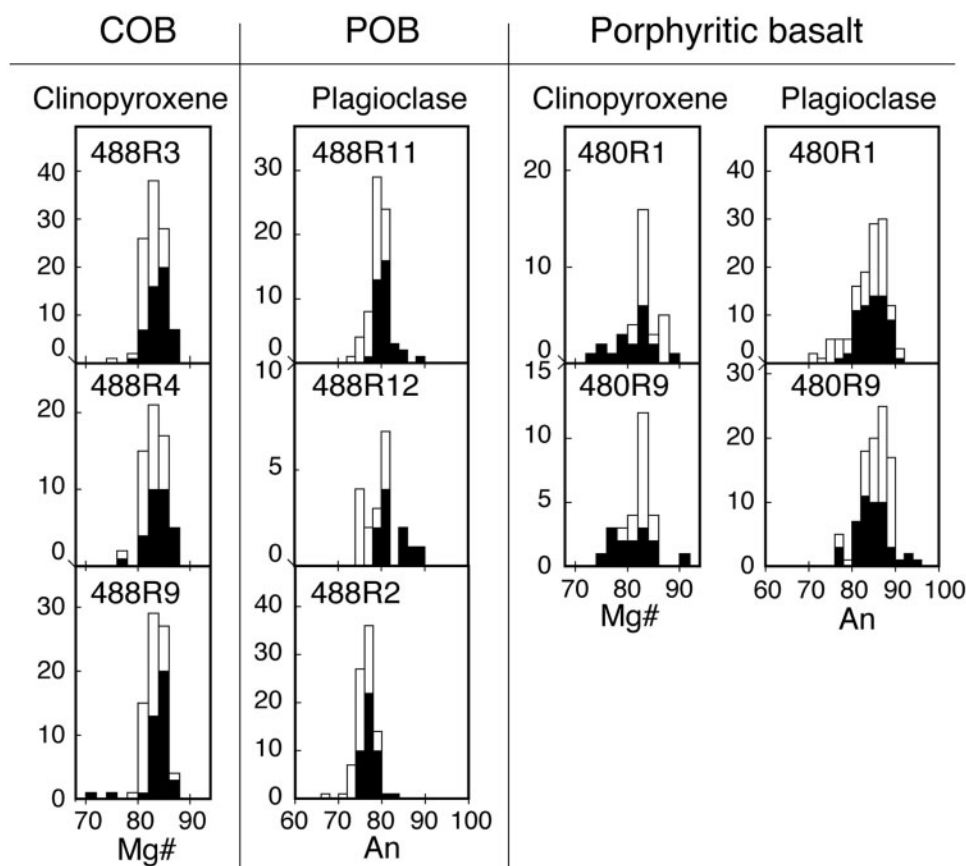
Fig. 12. Frequency distributions for the compositions of clinopyroxene phenocrysts in COB, plagioclase phenocrysts in POB, and clinopyroxene and plagioclase phenocrysts in the porphyritic basalts. Black and white bars indicate core and rim compositions, respectively.

of differentiation of COB magma, and porphyritic basalts have augites with lower Mg-numbers than those of COB. Thus, porphyritic basalts could be produced by COB fractionation. These conclusions are consistent with those based on trace element ratios (Fig. 4c and d) and REE patterns (Fig. 5), which also suggest that the porphyritic basalts are derived by fractionation of COB magma.

Olivine and plagioclase

Olivine–plagioclase assemblages in POB and porphyritic basalts are shown in Fig. 13. COB do not contain plagioclase phenocrysts, but porphyritic basalts represent differentiated COB magma type. Porphyritic basalts show distinctly high-An (>85) feldspar in more evolved melts in equilibrium with ~Fo_{80} olivine. On the other hand, POB contain more magnesian olivines (>Fo_{85}) but lower-An (An_{75-85}) feldspars. Olivine–plagioclase assemblages both in the POB and porphyritic basalts plot in the overlap of arc–BABB–MORB–OIB basalt fields, but the porphyritic basalts are displaced toward the field for oceanic arc basalts. This diagram further indicates that the porphyritic basalt cannot be derived from fractionation of POB

magma, and that the two NW Rota-1 magma types are compositionally distinct, with COB being more arc-like than POB.

PRIMARY MAGMAS

NW Rota-1 primitive and near-primitive lavas (Mg-number >60) are characterized by the following features: (1) both cpx–olivine basalts (COB) and plagioclase–olivine basalts (POB) are present (Fig. 3); (2) both magma types contain <6 vol. % phenocrysts, mostly olivine (Table 2); (3) observed olivine compositions are similar to those calculated to be in equilibrium with the host lava bulk compositions (Fig. 9); (4) magnesian olivine phenocrysts have compositions up to Fo_{93} and 0·4 wt % NiO, which overlap those of mantle olivines (Fig. 9). These observations allow estimation of the composition of the primary basalt magmas of NW Rota-1 volcano based on the method described by Tamura *et al.* (2000), described below.

A series of olivine and basalt compositions were calculated from an original basalt as follows: (1) the equilibrium olivine composition was obtained using the
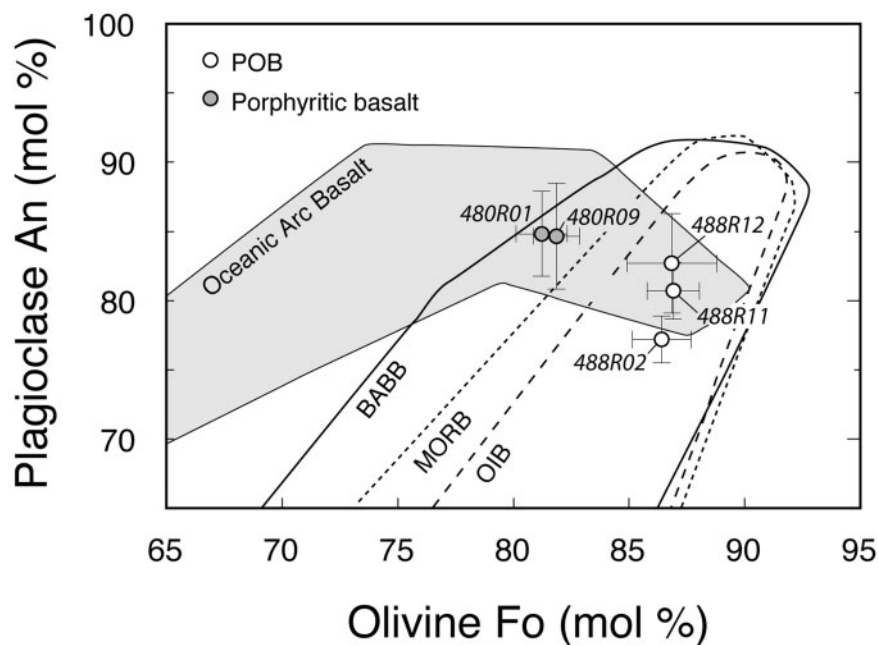
Fig. 13. Olivine–plagioclase compositions in POB and porphyritic basalts. Composition ranges for intra-oceanic arc, BABB, MORB and OIB are from Stern (2010). Assemblages in porphyritic basalts have distinctly high-An (>85) feldspar in more evolved melts in equilibrium with $Fo_{\sim 80}$ olivine.

$K_D(Fe/Mg)^{ol/liq}$ and $D_{Ni}^{ol/liq}$, assuming that $Fe^{3+}/(Fe^{2+} + Fe^{3+})$ in the melt was 0·2. (2) A more primitive basalt composition was calculated as a mixture of the basalt and the equilibrium olivine in a weight ratio of 99:1. (3) Steps (1) and (2) were repeated using the calculated, more primitive basalt to obtain another, more primitive basalt (Tamura *et al.*, 2000). This olivine fractionation model of Tamura *et al.* (2000) was revised by W. P. Leeman in 2004 and is available as a Microsoft® Excel© spreadsheet from the corresponding author (Tamura). The most magnesian olivines in NW-Rota 1 lavas are Fo_{93} and contain 0·4 wt % NiO, similar to the compositions of IBM forearc peridotite olivines (Fig. 9), which can be used to approximate the composition of the highly depleted IBM mantle wedge. The iterative addition of olivine and recalculation of basalt compositions were repeated until the calculated equilibrium olivines had 0·4 wt % NiO.

Stolper & Newman (1994) and Kelley *et al.* (2006, 2010) added equilibrium olivine back to equilibrium with Fo_{90}, and took the concentrations of elements in the modeled basalts as primitive compositions. Langmuir *et al.* (2006) noted that such a procedure presumes that all samples were derived from the same extent of melting of a homogeneous mantle source, as both extent of melting and source composition influence the forsterite content of residual olivine, which is likely to vary from Fo_{89} to Fo_{92}. We agree with these criticisms in the case of NW Rota-1 basalts because (1) the compositions of POB and COB do not indicate similar extents of melting of a homogeneous source,

and (2) some COB olivines and residual olivines of IBM forearc peridotites are more magnesian than Fo_{90} (Fig. 9).

The above procedure added 11–13 wt % olivines to POB and primary POB olivine compositions are $Fo_{91\cdot3–92\cdot1}$. On the other hand, COB needed 17–21 wt % addition of olivine and primary COB have $Fo_{92\cdot1–92\cdot4}$ olivines.

Major element compositions of NW Rota-1 primary basalt magmas were obtained by olivine addition modeling as described above. Incompatible trace elements were obtained with a Rayleigh crystal fractionation model by using the fraction of liquid (F) obtained by the olivine addition modeling. The olivine–liquid partition coefficient (D) for any incompatible element is never zero; however, $D = 0$ was used for all our calculations because (1) the difference between trace element values calculated by using $D = 0$ and $D = 0\cdot1$ at the smallest liquid fraction ($F = 0\cdot8$) is only ~2%, (2) most F values are >0·8, which reduces the differences, and (3) most reported D values for these incompatible elements are <0·1, which also makes the differences negligible. Table 3 lists the major and trace element compositions of the estimated primary POB and COB basaltic magmas.

All primary POB have higher TiO_2 and Na_2O and lower FeO* contents than those of primary COB. These differences are also recognized in analyzed POB and COB (Fig. 4a). However, differences in SiO_2, Al_2O_3 and MgO become obvious only after correcting for olivine fractionation. The SiO_2 (50·0–51·1 wt %) and MgO (12·1–14·3 wt %) contents of primary POB are

Table 3: Estimated primary arc basalts of NW Rota-1 volcano

Sample no.:	HPD488R02	HPD488R10	HPD488R11	HPD488R12	HPD488R13	HPD488R17	HPD488R01
Magma type:	POB	POB	POB	POB	POB	POB	COB
Added olivine %:	11	11	11	11	13	12	21
Fraction of liquid (F):	0·895	0·895	0·895	0·895	0·878	0·886	0·810
Equilibrium olivine Fo:	91·3	91·6	91·9	91·7	92·1	91·4	92·3
wt %							
SiO_2	51·09	50·46	50·18	50·25	50·03	50·58	49·64
TiO_2	0·81	0·78	0·76	0·77	0·76	0·80	0·66
Al_2O_3	15·20	14·70	14·36	14·48	14·00	15·02	13·56
FeO*	8·18	8·30	8·31	8·39	8·39	8·26	8·77
MnO	0·17	0·16	0·16	0·16	0·17	0·16	0·17
MgO	12·14	12·90	13·68	13·37	14·32	12·42	15·67
CaO	9·50	10·06	10·05	10·00	9·85	10·04	9·33
Na_2O	2·28	2·04	1·96	2·01	1·96	2·17	1·66
K_2O	0·49	0·46	0·40	0·43	0·40	0·42	0·42
P_2O_5	0·14	0·13	0·13	0·13	0·13	0·14	0·12
Total	100	100	100	100	100	100	100
ppm							
Rb	7·20	6·45	6·06	6·38	5·80	6·71	6·90
Sr	289	274	289	272	268	282	282
Y	18·9	17·5	18·7	17·7	16·7	18·1	14·6
Zr	59·7	51·7	54·9	50·6	49·3	51·1	38·8
Nb	3·28	2·59	2·54	2·43	2·26	2·50	1·12
Cs	0·14	0·15	0·14	0·13	0·11	0·25	0·19
Ba	91·9	78·0	79·6	77·7	73·9	81·9	77·0
La	5·26	4·47	4·78	4·35	4·24	4·63	4·64
Ce	12·05	10·60	11·68	10·28	9·98	10·88	10·57
Pr	1·56	1·44	1·52	1·38	1·33	1·46	1·44
Nd	7·48	6·89	8·18	6·80	6·78	7·23	7·30
Sm	2·22	2·05	2·40	2·03	1·90	2·10	1·90
Eu	0·85	0·76	0·83	0·76	0·77	0·78	0·68
Gd	2·59	2·33	2·72	2·51	2·25	2·40	2·13
Tb	0·44	0·42	0·48	0·42	0·40	0·43	0·37
Dy	2·80	2·72	2·90	2·70	2·54	2·79	2·25
Ho	0·63	0·57	0·65	0·59	0·57	0·62	0·50
Er	1·74	1·70	1·92	1·78	1·62	1·79	1·42
Tm	0·28	0·26	0·30	0·25	0·25	0·26	0·22
Yb	1·74	1·64	1·81	1·66	1·58	1·72	1·36
Lu	0·27	0·26	0·30	0·26	0·24	0·26	0·20
Hf	1·39	1·24	1·32	1·20	1·18	1·28	0·96
Ta	0·163	0·126	0·204	0·124	0·123	0·133	0·101
Pb	1·25	1·09	1·27	1·19	0·99	1·22	1·11
Th	0·517	0·413	0·425	0·421	0·410	0·445	0·481
U	0·188	0·160	0·248	0·186	0·144	0·157	0·192

(continued)

Table 3: Continued

Sample no.:	HPD488R03	HPD488R04	HPD488R05	HPD488R06	HPD488R07	HPD488R08	HPD488R09
Magma type:	COB	COB	COB	COB	COB	COB	COB
Added olivine %:	18	17	18	18	20	17	20
Fraction of liquid (F):	0·835	0·843	0·835	0·835	0·818	0·843	0·818
Equilibrium olivine Fo:	92·4	92·2	92·4	92·3	92·4	92·1	92·4
wt %							
SiO_2	49·57	49·75	49·51	49·66	49·61	49·70	49·74
TiO_2	0·64	0·64	0·64	0·64	0·65	0·64	0·65
Al_2O_3	13·42	13·64	13·39	13·57	13·68	13·50	13·45
FeO*	8·74	8·66	8·75	8·71	8·68	8·82	8·71
MnO	0·18	0·16	0·16	0·16	0·17	0·17	0·17
MgO	15·65	15·18	15·81	15·43	15·58	15·23	15·67
CaO	9·65	9·79	9·61	9·68	9·46	9·79	9·41
Na_2O	1·64	1·63	1·61	1·61	1·66	1·63	1·65
K_2O	0·40	0·41	0·41	0·42	0·41	0·42	0·43
P_2O_5	0·12	0·12	0·12	0·12	0·12	0·11	0·12
Total	100	100	100	100	100	100	100
ppm							
Rb	6·45	6·38	6·92	6·68	6·73	6·36	6·28
Sr	275	294	307	284	265	296	282
Y	13·5	14·3	15·3	14·2	13·9	14·0	13·8
Zr	36·6	34·8	37·5	34·1	36·8	34·7	34·3
Nb	1·00	1·13	1·03	1·07	1·14	1·10	1·01
Cs	0·15	0·14	0·16	0·13	0·12	0·14	0·13
Ba	79·1	80·8	84·0	81·0	79·9	80·9	78·4
La	4·66	4·65	5·07	4·66	5·13	4·47	4·33
Ce	10·38	9·96	11·53	10·29	11·19	9·87	9·88
Pr	1·45	1·36	1·57	1·34	1·43	1·34	1·29
Nd	7·32	6·89	7·63	6·66	7·24	6·55	6·48
Sm	1·92	1·79	2·13	1·79	2·01	1·81	1·77
Eu	0·69	0·68	0·76	0·66	0·74	0·65	0·65
Gd	2·13	2·08	2·43	1·90	2·30	2·07	1·97
Tb	0·36	0·35	0·40	0·34	0·39	0·35	0·33
Dy	2·28	2·13	2·33	2·10	2·26	2·13	2·02
Ho	0·48	0·47	0·50	0·45	0·47	0·46	0·44
Er	1·38	1·36	1·48	1·29	1·38	1·38	1·25
Tm	0·21	0·21	0·22	0·19	0·22	0·21	0·19
Yb	1·30	1·32	1·41	1·22	1·34	1·32	1·20
Lu	0·21	0·20	0·20	0·19	0·20	0·20	0·19
Hf	1·00	0·93	1·02	0·86	0·96	0·92	0·87
Ta	0·099	0·072	0·110	0·066	0·108	0·068	0·062
Pb	1·06	1·18	1·04	1·62	1·04	1·17	1·11
Th	0·444	0·491	0·446	0·491	0·488	0·485	0·476
U	0·181	0·172	0·205	0·170	0·187	0·178	0·162

systematically higher and lower, respectively, than those of primary COB (49·5–49·7 wt % SiO_2, 15·2–15·8 wt % MgO). Primary POB contain higher amounts of Al_2O_3 (14·0–15·2 wt %) than COB (13·4–13·7 wt %) (Table 3).

NW Rota-1 primary magmas vs experimental partial melts of mantle peridotite

Calculated NW Rota-1 primary basalt magmas, both COB and POB, are compared with estimated primary basalt magmas from Daisen volcano, SW Japan (Tamura *et al.*, 2000) and experimental partial melts of mantle peridotite in Figure 14. Figure 14a and b shows isobaric compositional trends for peridotite partial melts (Kushiro, 2001, figs 2 and 3). Data for partial melts of four mantle peridotites (HK66, PHN1611, KLB1 and MM3) are from Hirose & Kushiro (1993), Baker & Stolper (1994) and Kushiro (1996). Figure 14a shows the estimated Al_2O_3 and CaO contents of primary NW Rota-1 basalts and Daisen basalts. Daisen primary basalts plot in the relatively low melt fraction zone (Kushiro, 2001). NW Rota-1 primary basalts do not match any isobaric compositional trends of partial melts of these peridotites. Partial melt concentrations of CaO and Al_2O_3 depend on those in the source mantle, which are generally low. Primitive mantle is estimated to contain only 4·5 wt % CaO and 3·65 wt % Al_2O_3 (Palme & O'Neill, 2005). Therefore, the absolute concentrations of CaO and Al_2O_3 shown on the plots are less important than the different trends of the NW Rota-1 primary magmas. Al_2O_3 contents in the melt decrease as the degree of partial melting increases (Hirose & Kushiro, 1993), suggesting that the primary COB magmas resulted from higher degrees of partial melting than the primary POB magmas. CaO in the melt initially increases with increasing degree of melting (F) but then decreases after clinopyroxene disappears (Hirose & Kushiro, 1993). CaO in the primary NW Rota-1 basalts is significantly lower in the COB than in the POB magmas, suggesting the disappearance of clinopyroxene in the source of the primary COB magmas.

Figure 14b shows the FeO and MgO contents of partial melts formed from the four mantle peridotites, which have different Mg-number. The FeO content of the partial melt depends on the Mg-number of the peridotite (Baker & Stolper, 1994) and also increases with the pressure of melt generation (Fig. 14b). The FeO–MgO compositional trends of the partial melts are more or less sub-parallel; partial melts of more magnesian peridotites have lower FeO contents, whereas those formed from iron-rich peridotites have higher FeO contents (Kushiro, 2001). NW Rota-1 primary magmas plot on the isobaric compositional trends of partial melts formed from KLB-1 at 2 GPa, which has an Mg-number of 89·5, suggesting that the Mg-number of the source peridotite of the NW Rota-1

basalts could be similar. The Fo contents of some COB are higher than 89·5, which reflects the Mg-number of the residual peridotite. Figure 14b also suggests higher melt fractions for the primary COB magmas than for the primary POB and Daisen magmas, consistent with lower contents of fluid-immobile incompatible elements (Nb, Ta, Zr, Hf, Y and HREE) in COB relative to POB (Figs 4–7).

The NW Rota-1 and Daison primary magma compositions are plotted in the normative Ol–Pl–Qz diagram of Walker *et al.* (1979), together with the isobaric liquid compositional trends of garnet lherzolite melts determined by Kushiro (1996) and hydrous partial melts of KLB-1 at 1 GPa determined by Hirose & Kawamoto (1995) (Fig. 15). Hirose & Kushiro (1993) showed that the compositions of melts formed from HK-66 (Mg-number = 86·9) and KLB-1 (Mg-number = 89·5) lie approximately along the same isobaric line at the same pressure, indicating that the compositional differences between the two lherzolites do not significantly affect the isobaric trends in normative projections. Moreover, hydrous partial melts of KLB-1 at 1 GPa (Hirose & Kawamoto, 1995) plot roughly on the isobaric liquid compositional trend of PHN1611 (Mg-number = 86·8) at 1 GPa under dry conditions (Fig. 15), suggesting that these isobaric trends could be used to estimate the depth at which the hydrous NW Rota-1 primary magmas were generated, presumably by melting mantle peridotites with different compositions and water contents compared with the PHN1611 experiments.

The Walker plots (Fig. 15) suggest that the primary COB magmas were produced at slightly higher pressure (∼2 GPa) than the POB magmas (∼1·5 GPa). SiO_2 contents in primary mantle melts depend on pressure, decreasing with increasing pressure (Hirose & Kushiro, 1993). The average SiO_2 contents of the primary COB and POB magmas are 49·5 wt % and 50·3 wt %, respectively, which also suggests a higher equilibration pressure for COB relative to POB magmas. This is consistent with the higher Fe_8 of COB relative to POB (Fig. 6). Moreover, the NW Rota-1 primary magma compositions indicate that the degree of melting required to form the COB magmas is larger than for the POB magmas. This is consistent with their TiO_2, Na_2O, P_2O_5, Nb, Zr, Hf and Y contents, and compatible FeO contents on the MgO variation diagrams (Fig. 6a and 6), Zr/Y (Fig. 4b) and Nb/Yb (Fig. 4c), and Fo content of olivine in equilibrium with the spinel (Fig. 10).

NW Rota-1 primary magmas, supra-subduction zone mantle peridotites and extents of melting

The MgO contents of Izu–Bonin arc basalts (Tamura & Tatsumi, 2002) and those from the NE Japan arc volcanic
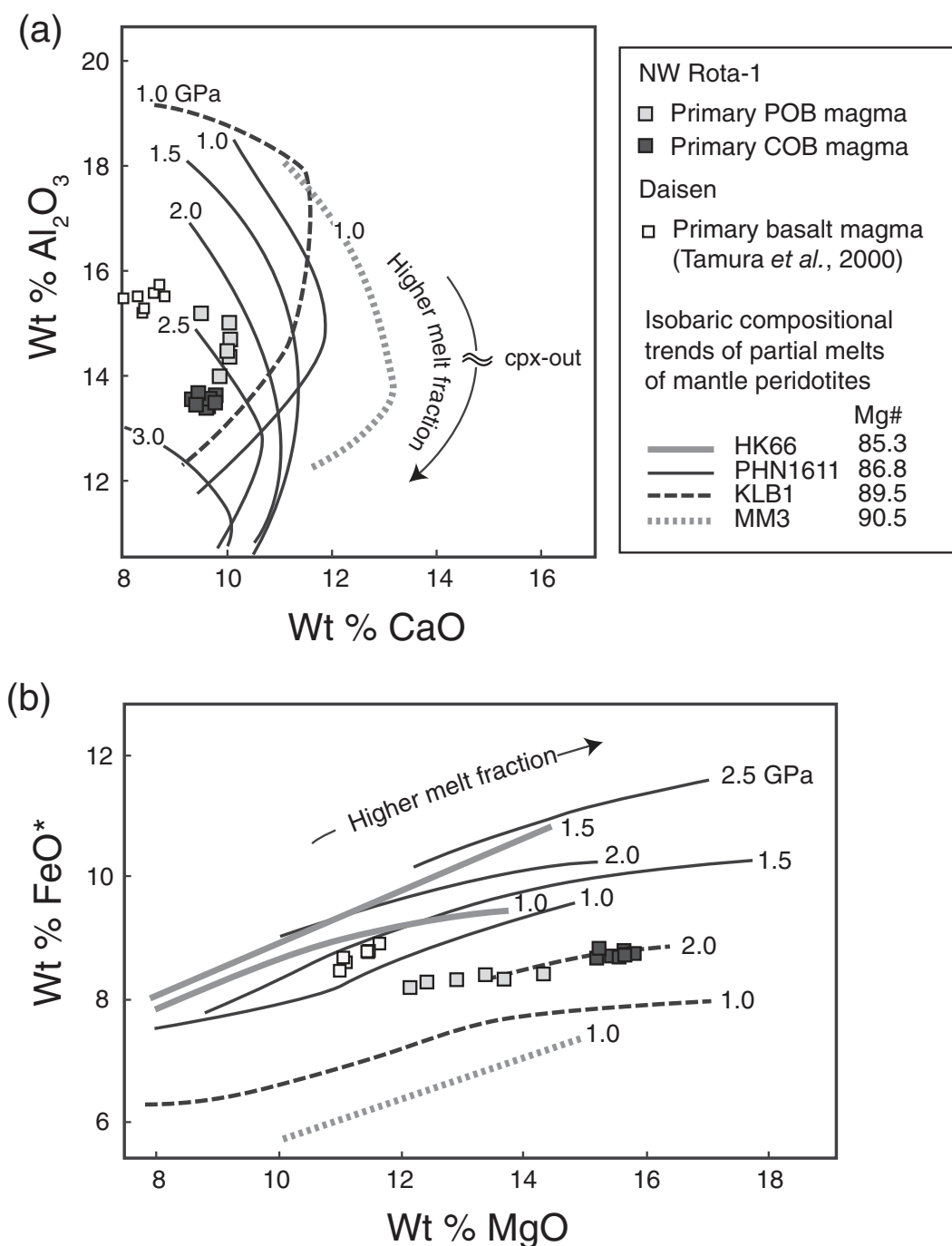
Fig. 14. Primary COB and POB magmas of NW Rota-1 volcano, primary basalt magmas from Daisen volcano, SW Japan (Tamura *et al.*, 2000) and isobaric compositional trends of experimental partial melts of four mantle peridotites (PHNl6ll, HK66, KLBl and MM3), plotted on (a) wt % Al₂O₃ vs wt % CaO and (b) wt % FeO* vs wt % MgO diagrams. Experimental melt data from Hirose & Kushiro (l993), and Baker & Stolper (l994) and Kushiro (l996, 200l).

front (Tamura, 2003) are mostly in the range 4–6 wt % but can be as high as ∼9 wt %. Most arc basalts are too differentiated and saturated with multiple phases to use for exploring the relationships of their mantle-derived arc primary magmas with mantle residues. Actual relationships between mantle-derived primary magmas and their residual mantle peridotites (lherzolite, harzburgite and dunite) have never been observed because of this crystal fractionation in arc magmas and the formation of cumulates.
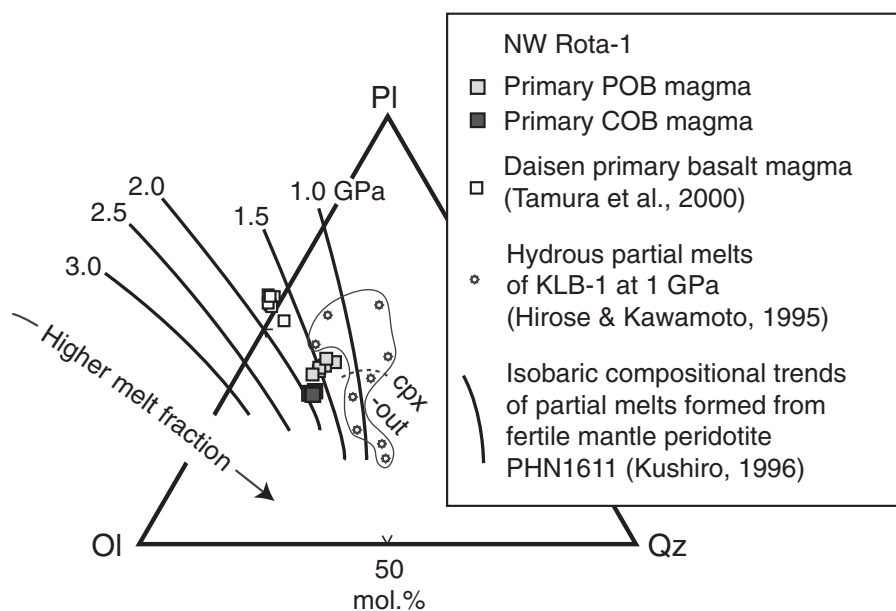
Fig. 15. Ol (olivine)−Pl (plagioclase)−Qz (SiO₂) projection of Walker *et al.* (1979) comparing calculated primary magma compositions for NW Rota-1 and Daisen volcanoes with isobaric liquid compositional trends for fertile garnet lherzolite (PHN1611) as determined by Kushiro (1996). Hydrous partial melts of KLB-1 at 1 GPa (Hirose & Kawamoto, 1995) plot near the PHN1611 1 GPa isobaric trend, possibly reflecting differences in the peridotite compositions and water contents. Calculated primary compositions of NW Rota-1 primary magmas suggest equilibration at 1·5–2·0 GPa (~60 km).

We have demonstrated the existence of two primary magma types for the NW Rota-1 volcano. Comparing these primary magmas and their likely mantle residues could provide valuable insights about mantle melting above subduction zones. Such residues are known from peridotite xenoliths from Avacha volcano (Ishimaru *et al.*, 2007; Ionov, 2010) as well as peridotites from two IBM forearc serpentinite seamounts, Torishima forearc and Conical, recovered by Ocean Drilling Program Leg 125 (Ishii *et al.*, 1992; Parkinson & Pearce, 1998) and the orogenic Horoman peridotite of Hokkaido, Japan (Takazawa *et al.*, 2000). NW Rota-1 primary basalts and these mantle residues are plotted on FeO*−MgO variation diagrams in Fig. 16.

We infer that the source mantle below NW Rota-1 volcano has Mg-number ~89·5 based on the FeO*−MgO diagram (Fig. 14). Interestingly, peridotite xenoliths from Avacha volcano and Torishima forearc and Conical seamounts have Mg-number >90, and thus may not represent the pre-melting mantle wedge of the Mariana arc. These peridotites could be residues after extensive melting (Ishii *et al.*, 1992; Parkinson & Pearce, 1998).

The low-MgO end of the array defined by the Horoman peridotite (Takazawa *et al.*, 2000) has an Mg-number of 89·6 (Fig. 16a). This is a plagioclase lherzolite (sample BZ-252) and has a composition similar to that estimated for the primitive mantle (McDonough & Frey, 1989; McDonough & Sun, 1995; Takazawa *et al.*, 2000). The

BZ-252 peridotite may thus be similar to the pre-melting mantle wedge below NW Rota-1. Calculated olivine Fo contents of primary COB and POB magmas average 92·3 and 91·7, respectively (Fig. 9b and c), which are similar to the Fo contents of residual mantle peridotites. The primary COB olivines are similar to those of Torishima forearc and Conical seamounts and the primary POB olivines are similar to those of the Avacha xenoliths, which are less magnesian than the former (Fig. 9). On two-element variation diagrams (Fig. 16), primary magma, source mantle and residual mantle should be collinear. Thus, the composition of the residual mantle in equilibrium with the primary COB magma plots in the range of the Torishima forearc and Conical seamounts on the straight line connecting primary COB and primitive mantle. Similarly, the residue of primary POB magma plots on the line POB–primitive mantle with an Mg-number similar to the Avacha peridotite xenoliths (Fig. 16b). On this basis, we can estimate the degree of melting for each basalt magma type by the Lever Rule. Primary COB magmas could be produced by ~24% partial melting of primitive mantle whereas the primary POB magmas result from ~18% melting (Fig. 16b).

Figure 16c shows primitive mantle (PM)-normalized incompatible trace element patterns of average primary COB and POB. Primitive mantle values are from McDonough & Sun (1995). It is interesting to compare this figure with Fig. 7. The mantle-derived component of
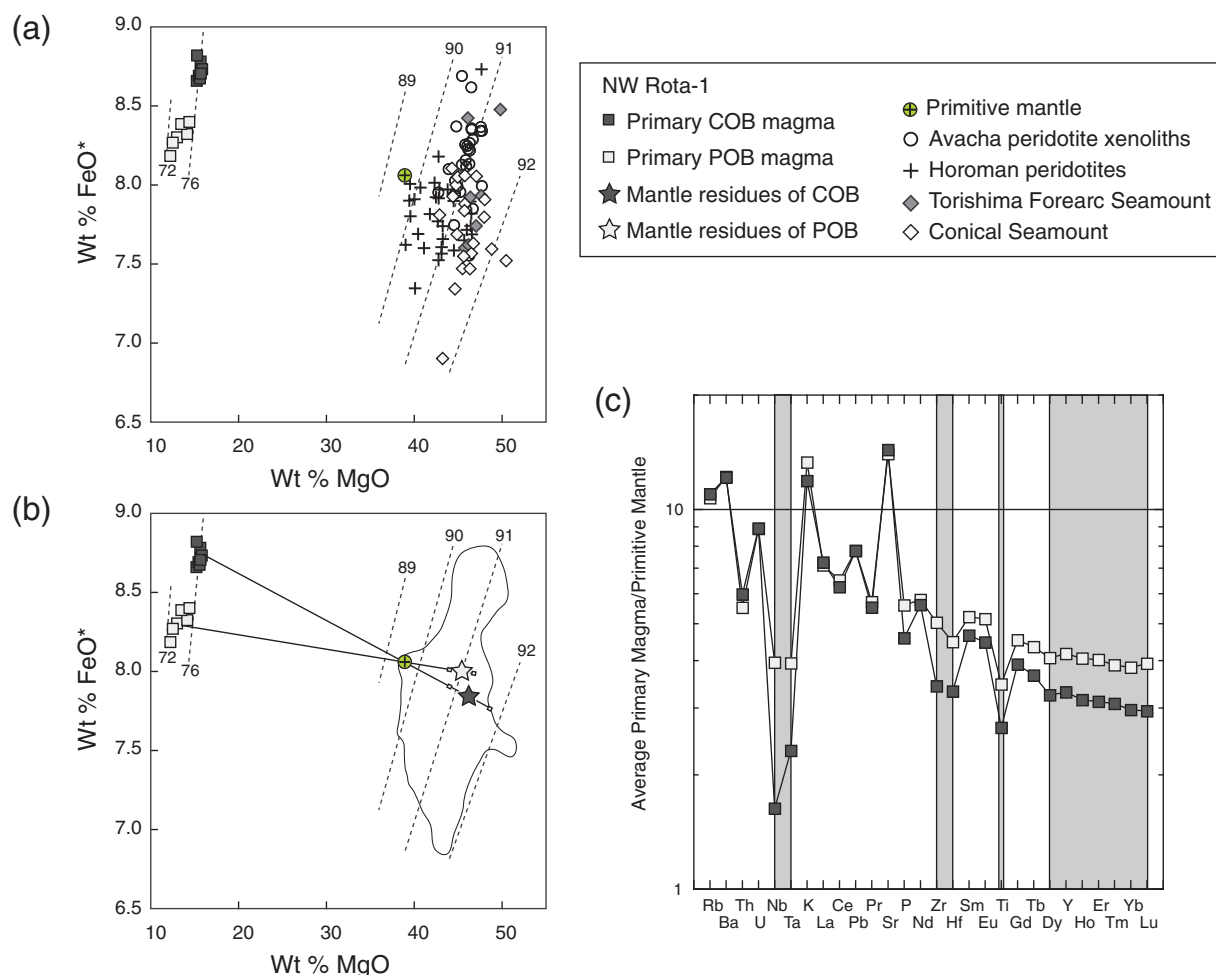
Fig. 16. (a) Wt % FeO* (total iron as FeO) vs wt % MgO of NW Rota-1 primary magmas and supra-subduction zone mantle peridotites represented by Avacha peridotite xenoliths (Ishimaru *et al.*, 2007; Ionov, 2010), Horoman peridotites (Takazawa *et al.*, 2000), and Torishima forearc seamount and Conical seamount (Parkinson & Pearce, 1998). Numbered fine dashed lines indicate Mg-numbers. The Horoman peridotite with the lowest MgO (BZ252, Takazawa *et al.*, 2000) is assumed as the mantle source. (b) Wt % FeO* (total iron as FeO) vs wt % MgO diagram showing lines connecting fertile (primitive) mantle and primary COB and POB magmas. The Mg-numbers of mantle residues after COB and POB extraction are estimated from olivine addition calculations (Fig. 9). (c) Primitive mantle (PM)-normalized incompatible trace element patterns of average primary COB and POB. Primitive mantle values are from McDonough & Sun (1995). The mantle components of the primary POB and COB are shown by the gray bands.

primary POB and COB, including Zr, Hf, Ti, Y and HREE, defines parallel patterns in Fig. 16c, with concentration ratios of POB/COB of about 4/3. This is consistent with the estimated degrees of partial melting (18% and 24%) based on the major element compositions (Fig. 16b) and the similar $^{176}Hf/^{177}Hf$ of POB and COB, which suggest mantle values (Fig. 8). However, the differences in Nb and Ta contents between POB and COB are much larger (~2), which requires greater differences in the degree of melting. POB/COB ratios are smaller for P and the MREE, which suggests some subduction component in the COB. The abundances of large ion lithophile elements (LILE), Th and LREE overlap between POB and COB, suggesting that these elements are not uniquely derived

from the mantle wedge but also from the subducting slab and that a much larger subduction component affected the COB source region.

DISCUSSION

Formation of the two NW Rota-1 magma types

We infer that POB and COB are derived from melting of mantle with the same Mg-number (~89·5) before partial melting, for two reasons. First, POB and COB occur together; both magma types were sampled along a single ROV track (HPD#488) on the eastern flank of NW Rota-1 at depths ranging from 2261 to 1649 m, over a

horizontal distance <5 km (Fig. 1c). Second, if the COB source was originally more depleted than the POB source or the COB were produced from POB mantle residue, the COB would plot on a different FeO*-depleted isobaric trend. However, the primary POB and COB compositions plot on the same isobaric compositional trend of KLB-1 on the FeO*–MgO diagram (Fig. 14b), suggesting that their sources had similar Mg-number.

Petrological conclusions about the formation of the two NW Rota-1 magma types based on this study are as follows.

(1) COB have lower TiO_2 and higher FeO* at the same MgO content than POB (Fig. 6a), mantle components (Nb, Ta, Zr, Hf, Y and HREE) are lower in COB than those in POB (Figs 6b and 7) and COB contain more magnesian olivines and Cr-rich spinels than POB (Figs 9–11). These lines of evidence suggest that primary COB formed from higher degrees of mantle melting than primary POB, which could be ~24% and ~18%, respectively (Fig. 16). This is reflected in the composition of the calculated mantle residues of COB and POB, which have olivines $Fo_{92.3}$ and $Fo_{91.7}$, respectively (Fig. 9).

(2) Olivine-hosted melt inclusions in recently erupted basaltic andesites of NW Rota-1 show water contents up to 6 wt % (A. Shaw, personal communication, 2010), but we have no direct evidence for the magmatic H_2O contents of the two primitive basalt types. Vesicularity may be a semi-quantitative indicator of volatile content, but both COB and POB contain variable amounts of vesicles (8–30 vol. %), which do not show systematic differences (Table 2). Phenocryst size may be another indicator; water appears to promote rapid growth of large crystals because it drastically diminishes the rate of nucleation so that the few nuclei that form grow into large crystals when the melt is undercooled. As described above, olivines in the COB are mostly 0·5–1·0 mm across, rarely up to 4 mm, and significantly larger than the POB olivines (mostly <0·5 mm). Moreover, cotectic crystallization of augite without plagioclase in the COB is a likely consequence of elevated magmatic water content that expands the clinopyroxene phase volume and suppresses plagioclase crystallization. Thus, phenocryst sizes and mineral assemblages (Table 2, Fig. 3) suggest that the COB parent magmas are more enriched in water than the POB magmas.

(3) COB primary magmas have a greater subduction component than POB, especially deep subduction components (sediment melt) derived from volcanic turbidites, which are known to be subducted beneath the Marianas arc (Plank & Langmuir, 1998; Figs 4–8).

(4) Estimated primary POB and COB magmas could have segregated from their mantle residues at ~1·5 GPa and ~2 GPa, respectively (Fig. 15).

Was mantle heterogeneity triggered by 'flush melting' of subducted oceanic sediment?

Stern *et al.* (2006) inferred the importance of water released from serpentinites in the genesis of magmas erupted from rear-arc volcanoes of the Guguan cross-chain, Mariana arc, based on the observation that melt inclusions from these lavas contain as much water as (or more water than) magmas from the volcanic front, whereas their host lavas show less trace element and isotopic evidence of a subduction component. This may reflect 'flush melting' owing to enhanced water flux from subducted serpentinites. Such serpentinites may form as a result of faulting at the outer trench swell, allowing water to infiltrate deep into the cold lithosphere about to be subducted (Ranero *et al.*, 2003; Contreras-Reyes *et al.*, 2008). Matsuno *et al.* (2010) reported results of a magnetotelluric (MT) survey across the central Mariana arc and found slightly lower resistivity near the Mariana Trench. They modeled this as related to hydration of the oceanic plate by water circulating along faults in the plate bending region. The effects of this serpentinite-sourced water may be responsible for the heterogeneity seen in NW Rota-1 magmas. COB primary magma has more sediment component and forms by a higher degree of melting of the mantle than POB, and probably has a higher water content. This could have resulted when the mantle wedge was metasomatized by melts of subducted oceanic sediment. Skora & Blundy (2010) coined the term 'flush melting' for the process whereby subducted sediments melt in the presence of excess water; for example, as a result of water released by serpentinite breakdown in the subducted lithospheric mantle. They showed that clay is ~54% molten at 3 GPa and a temperature of ~800°C in the presence of 15 wt % H_2O, in marked contrast to fluid-absent melting, which yields <~10% melt at this temperature. We suggest that water released as a result of serpentinite breakdown from the subducted lithospheric mantle resulted in flush melting of subducted sediments. Such hydrous sediment melts may have variably mixed with the overlying mantle to form the heterogeneous mantle source of the COB and POB.

Sediment melts and residual phases

Differences between COB and POB provide information about the subducted-sediment melt and residual phases in the slab. First, COB are enriched in 'fluid-mobile' elements such as Ba, Pb and Sr (Fig. 6) and have higher $^{87}Sr/^{86}Sr$, $^{206}Pb/^{204}Pb$, $^{207}Pb/^{204}Pb$ and $^{208}Pb/^{204}Pb$ than POB. Thus, it is suggested that the sediment melt is also enriched in

'slab-derived fluid' components and thus hydrous in addition to the sediment components. Moreover, COB are enriched in K_2O, LILE, LREE and Th (Fig. 6), which reflects the characteristics of the sediment melt and residual phases. The behavior of K_2O and LILE (Ba, Rb, Cs) is controlled by the presence of residual phengite; residual allanite and monazite control the behavior of LREE + Th (Skora & Blundy, 2010, and references therein). We suggest that phengite, allanite and monazite were not present as residual phases, so that the sediment melt is enriched in these elements. On the other hand, COB are depleted in Nb, Ta, Zr, Hf, Y and HREE relative to POB (Figs 6 and 7) and there are no systematic differences in $^{176}Hf/^{177}Hf$ between COB and POB (Fig. 8b). The stability of rutile exerts a primary control on the behavior of HFSE; garnet is known to be a major host for the HREE (Skora & Blundy, 2010, and references therein). Skora & Blundy (2010) suggested that zircon, which controls Zr and Hf abundances in sediment melts, is exhausted from the residue relatively early at low temperatures, but that

appreciable Zr and Hf are incorporated into residual garnet (Skora & Blundy, 2010). We suggest that rutile and garnet were present as residual phases so that the sediment melt is depleted in these elements, resulting in similar $^{176}Hf/^{177}Hf$, which reflects mantle values. If the sediment melt in the subducted slab below NW Rota-1 was produced by flush melting of radiolarian clay as shown by Skora & Blundy (2010), the temperature of the uppermost part of the slab must be higher than phengite-out and monazite-out temperatures ($\sim900°C$), but lower than rutile-out and garnet-out ($\sim1000°C$).

Mariana mantle wedge

Figure 17 shows the structure of the Mariana subduction zone and schematic mass flow lines (convection). The thermal and mantle flow model for the Mariana subduction zone of Wada & Wang (2009) predicts that the subducting crust undergoes peak crustal dehydration at 75–120 km depth, providing fluid for mantle hydration. Hydrous phases in the hydrated mantle both in the mantle wedge
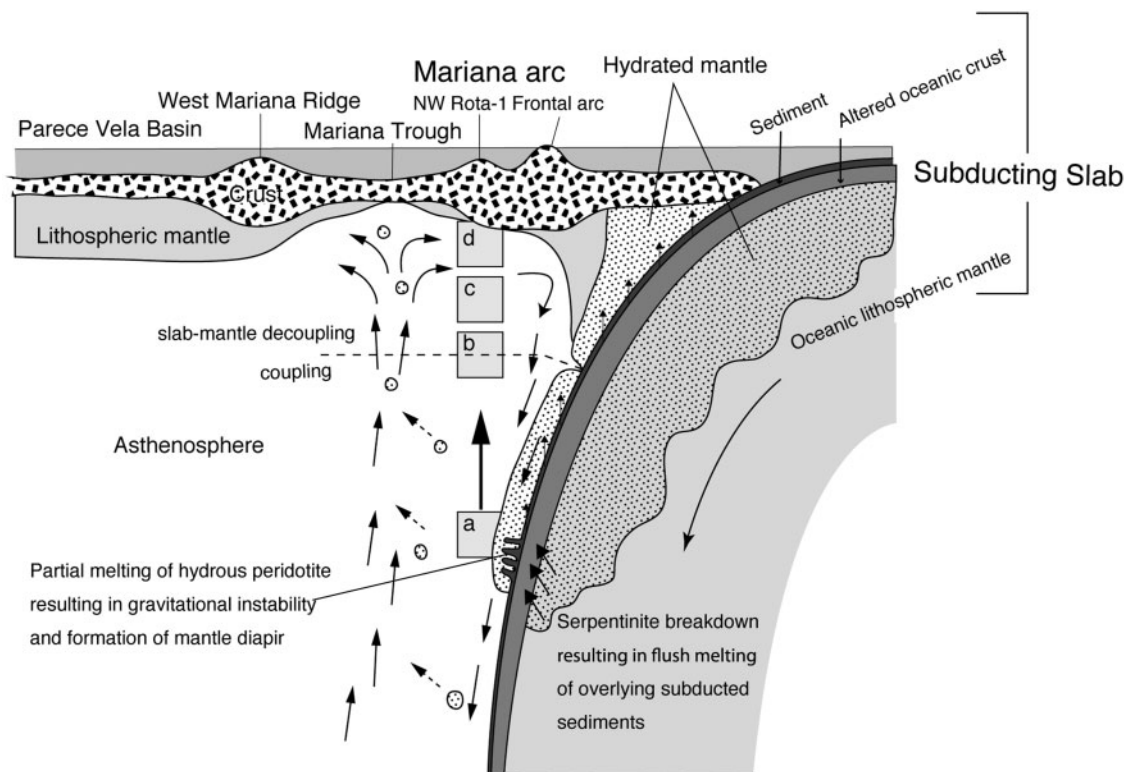

Fig. 17. Section perpendicular to the Mariana arc–back-arc basin system, showing schematic mass flow lines (convection). The upper part of the subducting slab (oceanic lithosphere) may be hydrated by bend-faulting and serpentinized (Ranero *et al.*, 2003; Contreras-Reyes *et al.*, 2008; Matsuno *et al.*, 2010). The lower part of the mantle wedge, which is dragged deeper by the slab at depths >80 km, is derived from fresh convecting mantle wedge that would have been hydrated at depths >80 km. Subducted sediment melts below NW Rota-1 between 900°C and 1000°C, and this is accompanied by flushing of fluids derived from the underlying dehydrating serpentinites of the subducting slab. Flush melting and mixing of the hydrous sediment melt with hydrated mantle in the lower part of the mantle wedge results in gravitational instability and formation of partially melted mantle diapirs. Beneath the Mariana Trough, mantle upwelling is more likely to occur in conjunction with small-scale convection. This could transfer some mantle peridotite hydrated under the arc back into the back-arc mantle (dotted arrows) (e.g. Langmuir *et al.*, 2006). Rectangles a–d correspond to the four panels in Fig. 18.

and subducting oceanic lithospheric mantle, such as antigorite and chlorite, are stable to greater depths, providing fluid in the back-arc region. Down-dragged hydrated mantle within the mantle wedge (e.g. Tatsumi, 1986) and subducting oceanic lithospheric mantle are shown in Fig. 17. Serpentinite breakdown in the underlying portions of the slab would result in flush melting of overlying subducted sediments (Fig. 17). Therefore, the release of aqueous fluid from the slab may not be restricted to the forearc region. An important finding of Wada & Wang (2009) is that the overriding mantle is mechanically decoupled from the slab at depths shallower than ~70–80 km and thus does not participate in the wedge flow. Thus, the lower part of the mantle wedge, which is dragged deeper by the slab at depths >80 km, is not derived from beneath the forearc, but fresh convecting mantle wedge shown by the arrow in Fig. 17. This dragged mantle would have been hydrated by fluids derived from the subducting slab at depths >80 km.

Isse *et al.* (2009) showed the three-dimensional shearwave velocity anomaly structure of the IBM arc. Their study revealed three slow anomalies at a scale of 500 km in the mantle wedge along the IBM arc, suggesting that mantle flow in the IBM mantle wedge is not a continuous sheet-like flow but is separated into several segments. The southern anomaly lies beneath the widest portion of the active-spreading Mariana Trough. Isse *et al.* (2009) speculated that deep mantle enters the wedge of the subduction zone, and then branches into 'hot fingers' as it ascends toward the volcanic front, which can explain the complex shear-wave splitting pattern observed for the IBM arc. The arrows in Fig. 17 show the convection of this large-scale flow, which comes from the mantle below the Mariana Trough and moves toward the volcanic front.

Thermal and mantle flow models using a realistic temperature-dependent mantle rheology (e.g. Furukawa, 1993; van Keken *et al.*, 2002; Wada & Wang, 2009) predict focusing of mantle wedge flow beneath the arc, which results in narrower spacing of flow streamlines and temperature contours. We expect that the source of the NW Rota-1 magmas is fertile lherzolitic mantle, supplied as a result of this counter flow and hydrated at >80 km depth.

Measurements of heat flow and thermobarometry data on mantle xenoliths indicate that most back-arcs are hot, even those that have not undergone recent extension (Currie & Hyndman, 2006). This indicates that there is a common mechanism to bring heat up from depth. One possible mechanism is small-scale mantle convection (Honda & Saito, 2003; Honda & Yoshida, 2005; Honda *et al.*, 2007), which is not shown in Fig. 17. This buoyancy-driven flow does not affect the forearc–arc mantle wedge owing to its cold nature, narrow space and small vertical temperature difference. In back-arcs with a

spreading ridge, mantle upwelling is more likely to occur in conjunction with small-scale convection. This could transfer some mantle peridotite hydrated under the arc back into the back-arc mantle (dotted arrows in Fig. 17) (e.g. Langmuir *et al.*, 2006) and result in the wide chemical variation of the BABB as shown in their REE patterns (Fig. 5) and Sr–Nd–Pb isotope ratios (Fig. 8a). The spacing of volcanoes and cross-arc chains in the Mariana arc (Fig. 1) might suggest the presence of 'hot fingers' in the mantle wedge, as discussed for the NE Japan arc (Tamura *et al.*, 2002). Models of small-scale convection have also been applied to explain the presence of such hot mantle fingers (Honda & Saito, 2003; Honda & Yoshida, 2005; Honda *et al.*, 2007), which split the large-scale convection (Isse *et al.*, 2009) into fingers.

How did two magma types form beneath NW Rota-1?

Figure 18 graphically summarizes how we think the two primary magma types are generated below NW Rota-1. Flux melting and decompression melting can be two-dimensional, but mantle diapirism or mantle wedge plumes are three-dimensional (Hall & Kincaid, 2001; Gerya & Yuen, 2003; Honda & Yoshida, 2005; Gerya *et al.*, 2006; Honda *et al.*, 2007; Zhu *et al.*, 2009). Moreover, it is often observed that lavas from single volcanoes show different chemical trends from those of adjacent volcanoes, as do NW Rota-1 and the East knoll (Fig. 2), which is supporting evidence for some control by mantle diapirism (Sakuyama, 1983). Although the diapir model of subduction magmatism has fallen out of favor in recent years, the experimental results of Hall & Kincaid (2001) reaffirm the feasibility of this model, which fulfills the following observational constrains: the rapid transport times of arc magmas required by recent ^{238}U–^{230}Th disequilibrium and ^{10}Be studies, the observed periodicity of magma production at arcs and the sustained high-volume magmatism at central volcanoes. However, ^{226}Ra–^{230}Th disequilibria of the order of a few thousand years or less (e.g. Turner *et al.*, 2003) are not consistent with the diapir model. We suspect that such discrepancies will be reconciled in future studies, and demonstrate here how the genesis of two magma types within a single volcano can be explained by diapiric upwelling (e.g. Hall & Kincaid, 2001; Zhu *et al.*, 2009).

Our preferred interpretation is similar to the model of Green *et al.* (1967). Hydration and partial melting of the mantle wedge above subducting slabs can trigger Rayleigh–Taylor-like instabilities. Deep subduction components, derived from flush melting of subducting sediments, play an important role in the generation of NW Rota-1 magmas. Thus, sediment melting in the subducting slab at 900–1000°C and the addition of this hydrous sediment melt to the overlying mantle wedge could have
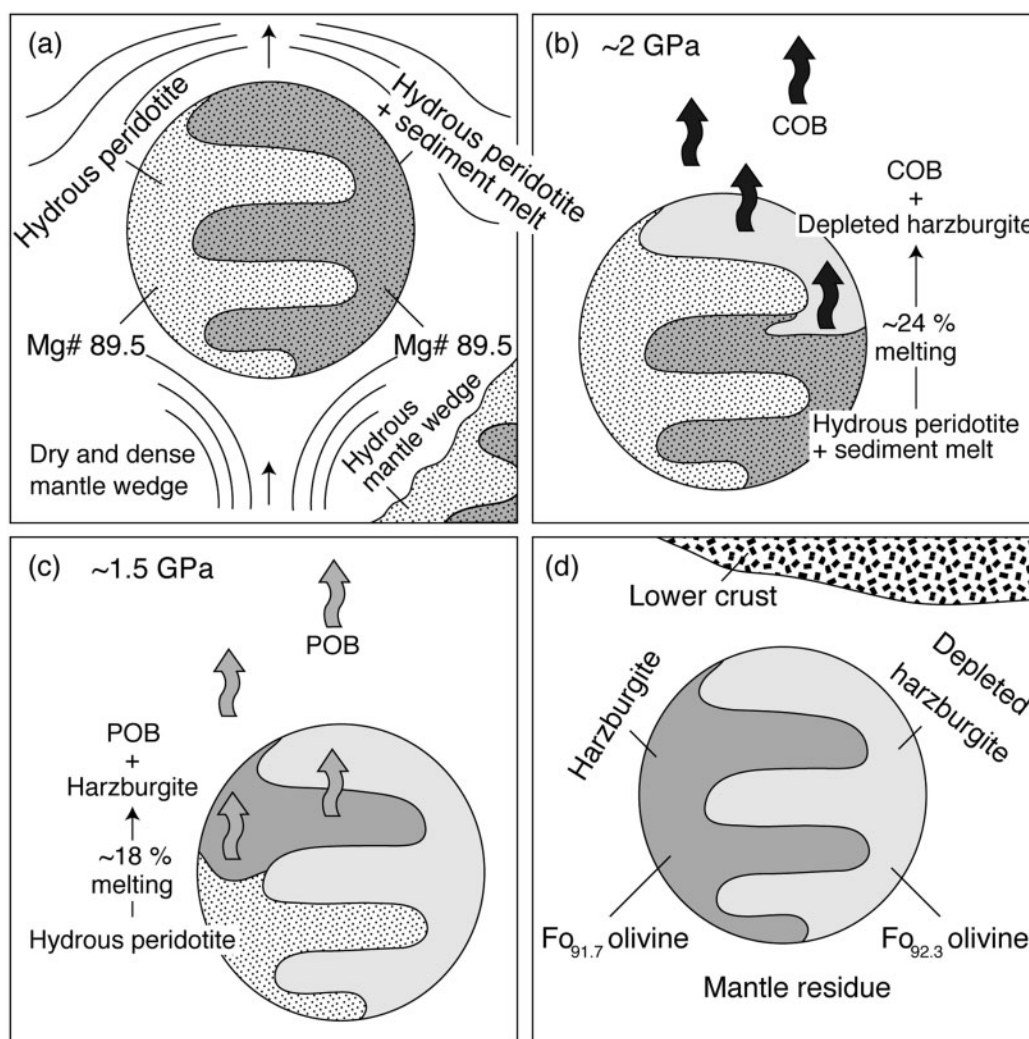
Fig. 18. Details of source modification and melting processes associated with the diapirs responsible for COB and POB melts. (a) Mantle diapir consisting of hydrated peridotite (Mg-number 89·5) and sediment melt is formed in the lower part of the mantle wedge above the subducted slab. (b) COB are produced by 24% melting of the mixture of hydrous peridotite and sediment melt at a depth corresponding to a pressure of ∼2 GPa. (c) POB are produced by 18% melting of hydrous peridotite. (d) Mantle residues below the crust consist of harzburgite (Fo of olivines ∼91·7) and depleted harzburgite (Fo ∼92·3).

triggered partial melting (Fig. 18a). We suggest that high temperatures at the base of mantle wedge (>1000°C), combined with slab-derived metasomatic agents (hydrous sediment melt addition), ultimately lead to sufficient partial melting to induce buoyancy and to initiate diapiric ascent. A crystal–liquid mush (diapir) will result from the onset of partial melting, but as long as the crystals and liquid remain together, equilibrium between the crystals and liquid will be maintained over the changing pressure–temperature conditions caused by the upward movement of the mush (Green *et al.*, 1967). Sediment melts may mix heterogeneously with hydrous peridotite, resulting in a mantle diapir consisting of two parts, one poor and another rich in sediment melt (Fig. 18b).

As partial melting during the upward 'convective' motion proceeds, a critical point will be reached at which the liquid becomes segregated from the complementary residual crystals (Green *et al.*, 1967). We conclude that COB formed from ∼24% partial melting of hydrous peridotite plus sediment melt at ∼2 GPa (Fig. 18c) whereas POB are ∼18% partial melts of hydrous peridotite at ∼1·5 GPa, which was less affected by sediment melt. The critical point required for segregation is that melting reached ∼24%, which the COB diapir reached at ∼2 GPa.

Production of COB and POB would have formed residues of depleted harzburgite (olivine Fo = 92·3) and harzburgite (olivine Fo = 91·7) (Fig. 18d). This estimated

variation is consistent with the variations shown by mantle residues (Fig. 16).

Tamura *et al.* (2005, 2007) observed two types of basalt magma in the Sumisu and Torishima volcanoes in the IBM arc to the north, low-Zr and high-Zr, respectively, originating from wet and dry parental basaltic magmas; however, neither of these contains deep subduction (sediment melt) components. The COB and POB could be their equivalents in the Mariana arc, which are much more influenced by subducted sediment components. Moreover, it is suggested based on olivine–plagioclase assemblages in intra-oceanic arc volcanoes (Fig. 13) that one parental basalt magma type cannot produce the observed variation in oceanic arc basalts, which implicitly requires another magma type. Thus, COB and POB might generally exist in arc volcanoes, but be difficult to recognize because of mixing and fractionation.

CONCLUSIONS

We demonstrate the existence of near-primitive, phenocryst-poor lavas at NW Rota-1 volcano in the Mariana arc. These magnesian basalts are petrographically distinct cpx–olivine basalt (COB) and plagioclase–olivine basalts (POB). The Fo contents of olivines and Cr-number of spinels are higher in COB than in POB. Moreover, COB are lower in Zr/Y and Nb/Yb and TiO_2, Al_2O_3, Na_2O, P_2O_5, Nb, Ta, Zr, Hf, HREE and Y than POB, both at $MgO = 8$ wt % and in the estimated primary magmas, suggesting that COB formed from higher degrees of mantle melting. COB have Ba/Nb, Th/Nb, $^{87}Sr/^{86}Sr$, $^{208}Pb/^{206}Pb$ and $^{207}Pb/^{206}Pb$ that are higher than for POB, and also have steeper LREE-enriched patterns and lower $^{143}Nd/^{144}Nd$, indicating that COB have a greater subduction component than POB. The $^{176}Hf/^{177}Hf$ ratios of COB and POB are similar, and Hf behavior in COB and POB is similar to that of Zr, Y and HREE, suggesting that Hf is not included in the subduction component, which produced the differences between COB and POB. The estimated subduction component suggests flush melting of subducting sediment in the uppermost part of the slab at a temperature between phengite-out and monazite-out ($\sim900°C$) and rutile-out and garnet-out ($\sim1000°C$). Estimated primary COB and POB magmas show that the source mantle for both had an Mg-number of $\sim89·5$ with melt segregation pressures of ~2 GPa and $\sim1·5$ GPa, respectively. Degrees of mantle melting required to form primitive COB and POB are $\sim24\%$ and 18%, respectively. Diapiric ascent of hydrous peridotite mixed heterogeneously with sediment melts may be responsible for the NW Rota-1 basalts. The Mariana COB and POB could be the equivalents of the low-Zr and high-Zr basalts recognized in the Izu arc, and similar distinct magmas might generally coexist in arc volcanoes.

SUPPLEMENTARY DATA

Supplementary data for this paper are available at *Journal of Petrology* online.

REFERENCES

Arai, S. (1994). Characterization of spinel peridotite by olivine–spinel compositional relationships: review and interpretation. *Chemical Geology* **113**, 191–204.

Arai, S. & Ishimuru, S. (2008). Insights into petrological characteristics of mantle wedge beneath arcs through peridotite xenoliths: a review. *Journal of Petrology* **49**, 665–695.

Arculus, R. J. (2003). Use and abuse of the terms calcalkaline and calcalkalic. *Journal of Petrology* **44**, 929–935.

Baker, M. B. & Stolper, E. M. (1994). Determining the composition of high-pressure mantle melts using diamond aggregates. *Geochimica et Cosmochimica Acta* **58**, 2811–2827.

Bloomer, S. H., Stern, R. J. & Smoot, N. C. (1989). Physical volcanology of the submarine Mariana and Volcano arcs. *Bulletin of Volcanology* **51**, 210–224.

Chadwick, W. W., Cashman, K. V., Embley, R. W., Matsumoto, H., Dziak, R. P., de Ronde, C. E. J., Lau, T.-K., Deardorff, N. & Merle, S. G. (2008). Direct video and hydrophone observations of submarine explosive eruptions at NW Rota-1 volcano, Mariana arc. *Journal of Geophysical Research* **113**, B08S10, doi:10.1029/2007JB005215.

Chadwick, W. W., Embley, R. W., Baker, E. T., Resing, J. A., Lupton, J. E., Cashman, K. V., Dziak, R. P., Tunnicliffe, V., Butterfield, D. A. & Tamura, Y. (2010). Spotlight 10/Northwest Rota-1 Seamount. *Oceanography* **23**, 182–183.

Contreras-Reyes, E., Grevemeyer, I., Flueh, E. R. & Reichert, C. (2008). Upper lithospheric structure of the subduction zone offshore of southern Arauco peninsula, Chile, at $\sim38°S$. *Journal of Geophysical Research* **113**, B07303, doi:10.1029/2007JB005569.

Currie, C. A. & Hyndman, R. D. (2006). The thermal structure of subduction zone back arcs. *Journal of Geophysical Research* **111**, B08404, doi:10.1029/2005JB004024.

Dick, H. J. B. (1989). Abyssal peridotites, very slow spreading ridges and ocean ridge magmatism. In: Saunders, A. D. & Norry, M. J. (eds) *Magmatism in the Ocean Basins. Geological Society, London, Special Publications* **42**, 71–105.

Elliott, T., Plank, T., Zindler, A., White, W. & Bourdon, B. (1997). Element transport form slab to volcanic front at the Mariana arc. *Journal of Geophysical Research* **102**, 14991–15019.

Embley, R. W., Chadwick, W. W., Baker, E. T. *et al.* (2006). Long-term eruptive activity at a submarine arc volcano. *Nature* **441**, 494–497.

Furukawa, Y. (1993). Depth of the decoupling plate interface and thermal structure under arcs. *Journal of Geophysical Research* **98**, 20005–20013.

Gerya, T. V. & Yuen, D. A. (2003). Rayleigh–Taylor instabilities from hydration and melting propel 'cold plumes' at subduction zones. *Earth and Planetary Science Letters* **212**, 47–62.

Gerya, T. V., Connolly, J. A. D., Yuen, D. A., Gorczyk, W. & Capel, A. M. (2006). Seismic implications of mantle wedge plumes. *Physics of the Earth and Planetary Interiors* **156**, 59–74.

Gill, J. B. (1976). Comparison and age of Lau Basin and Ridge volcanic rocks: implications for evolution of an interarc basin and remnant arc. *Geological Society of America Bulletin* **87**, 1384–1395.

Gill, J. B. (1981). *Orogenic Andesites and Plate Tectonics*. Berlin: Springer.

Green, T. H., Green, D. H. & Ringwood, A. E. (1967). The origin of high-alumina basalts and their relationships to quartz tholeiites and alkali basalts. *Earth and Planetary Science Letters* **2**, 41–51.

Gribble, R. F., Stern, R. J., Bloomer, S. H., Stüben, D., O'Hearn, T. & Newman, S. (1996). MORB mantle and subduction components interact to generate basalts in the southern Mariana Trough back-arc basin. *Geochimica et Cosmochimica Acta* **60**, 2153–2166.

Hall, P. S. & Kincaid, C. (2001). Diapiric flow at subduction zones: a recipe for rapid transport. *Science* **292**, 2472–2475.

Hart, S. R. (1984). A large-scale isotope anomaly in the Southern Hemisphere mantle. *Nature* **309**, 753–757.

Heeszel, D. S., Wiens, D. A., Shore, P. J., Shiobara, H. & Sugioka, H. (2008). Earthquake evidence for along-arc extension in the Mariana Islands. *Geochemistry, Geophysics, Geosystems* **9**, doi:10.1029/2008GC002186.

Hirose, K. & Kawamoto, T. (1995). Hydrous partial melting of lherzolites at 1 GPa: the effect of H_2O on the genesis of basaltic magmas. *Earth and Planetary Science Letters* **133**, 463–473.

Hirose, K. & Kushiro, I. (1993). Partial melting of dry peridotites at high pressures: determination of compositions of melts segregated from peridotite using aggregates of diamond. *Earth and Planetary Science Letters* **114**, 477–489.

Honda, S. & Saito, M. (2003). Small-scale convection under the back-arc occurring in the low viscosity wedge. *Earth and Planetary Science Letters* **216**, 703–715.

Honda, S. & Yoshida, T. (2005). Application of the model of small-scale convection under the island arc to the NE Honshu subduction zone. *Geochemistry, Geophysics, Geosystems* **6**, Q01002, doi:10.1029/2004GC000785.

Honda, S., Yoshida, T. & Aoike, K. (2007). Spatial and temporal evolution of arc volcanism in the northeast Honshu and Izu–Bonin arcs: evidence of small-scale convection under the island arc? *Island Arc* **16**, 214–223.

Ionov, D. A. (2010). Petrology of mantle wedge lithosphere: new data on supra-subduction zone peridotite xenoliths from the andesitic Avacha volcano, Kamchatka. *Journal of Petrology* **51**, 327–361.

Ishii, T., Robinson, P. T., Maekawa, H. & Fiske, R. (1992). Petrological studies of peridotites from diapiric serpentinite seamounts in the Izu–Ogasawara–Mariana forearc, Leg 125. In: Fryer, P., Pearce, J. A. & Stokking, L. B. *et al.* (eds) *Proceedings of the Ocean Drilling Program, Scientific Results, 125*. College Station, TX: Ocean Drilling Program, pp. 445–485.

Ishimaru, S., Arai, S., Ishida, Y., Shirasaka, M. & Okrugin, V. M. (2007). Melting and multi-stage metasomatism in the mantle wedge beneath a frontal arc inferred from highly depleted peridotite xenoliths from the Avacha volcano, southern Kamchatka. *Journal of Petrology* **48**, 395–433.

Ishizuka, O., Taylor, R. N., Milton, J. A. & Nesbitt, R. W. (2003). Fluid-mantle interaction in an intra-oceanic arc: Constraints from high-precision Pb isotopes. *Earth and Planetary Science Letters* **211**, 221–236, doi:10.1016/S0012-821X(03)00201-2.

Ishizuka, O., Geshi, N., Itoh, J., Kawanabe, Y. & TuZino, T. (2008). The magmatic plumbing of the submarine Hachijo NW volcanic chain, Hachijojima, Japan: long-distance magma transport? *Journal of Geophysical Research* **113**, doi:10·1029/2007JB005325.

Isse, T., Shiobara, H., Tamura, Y. *et al.* (2009). Seismic structure of the upper mantle beneath the Philippine Sea from seafloor and land observation: implications for mantle convection and magma genesis in the Izu–Bonin–Mariana subduction zone. *Earth and Planetary Science Letters* **278**, 107–119.

Johnson, C. M. & Beard, B. L. (1999). Correction of instrumentally produced mass fractionation during isotopic analysis of Fe by thermal ionization mass spectrometry. *International Journal of Mass Spectrometry* **193**, 87–99.

Kato, T., Beavan, J., Matsushima, T., Kotake, Y., Camacho, J. T. & Nakao, S. (2003). Geodetic evidence of back-arc spreading in the Mariana Trough. *Geophysical Research Letters* **30**, doi:10.1029/2002GL016757.

Kelemen, P. B., Yogodzinski, G. M. & Scholl, D. W. (2003). Along-strike variation in the Aleutian island arc: genesis of high Mg# andesite and implications for continental crust. In: Eiler, J. (ed.) *Inside the Subduction Factory. Geophysical Monograph, American Geophysical Union* **138**, 223–276.

Kelley, K. A. & Cottrell, E. (2009). Water and the oxidation state of subduction zone magmas. *Science* **325**, 605–607.

Kelley, K. A., Plank, T., Grove, T. L., Stolper, E. M., Newman, & Hauri, E. H. (2006). Mantle melting as a function of water content beneath back-arc basins. *Journal of Geophysical Research* **111**, B09208, doi:10.1029/2005JB003732.

Kelley, K. A., Plank, T., Newman, S., Stolper, E. M., Grove, T. L., Parman, S. & Hauri, E. H. (2010). Mantle melting as a function of water content beneath the Mariana arc. *Journal of Petrology* **51**, 1711–1738.

Klein, E. M. & Langmuir, C. H. (1987). Global correlations of ocean ridge basalt chemistry with axial depth and crustal thickness. *Journal of Geophysical Research* **92**, 8089–8115.

Kohut, E. J., Stern, R. J., Kent, A. J. R., Nielsen, R. L., Bloomer, S. H. & Leybourne, M. (2006). Evidence for adiabatic decompression melting in the southern Mariana arc from High-Mg lavas and melt inclusions. *Contributions to Mineralogy and Petrology* **152**, 201–221.

Kushiro, I. (1996). Partial melting of a fertile mantle peridotite at high pressures: an experimental study using aggregates of diamond. In: Basu, A. & Hart, S. (eds) *Earth Processes: Reading the Isotopic Code. Geophysical Monograph, American Geophysical Union* **95**, 109–122.

Kushiro, I. (2001). Partial melting experiments on peridotite and origin of mid-ocean ridge basalt. *Annual Review of Earth and Planetary Sciences* **29**, 71–107.

Langmuir, C. H., Bézos, A., Escrig, S. & Parman, S. W. (2006). Chemical systematics and hydrous melting of the mantle in back-arc basins. In: Christie, D. M., Fisher, C. R., Lee, S.-M. & Givens, S. (eds) *Back-arc Spreading Systems: Geological, Biological, Chemical, and Physical Interactions. Geophysical Monograph, American Geophysical Union* **166**, 87–146.

Matsuno, T., Seama, N., Evans, R. L., Chave, A. V., Baba, K., White, A., Goto, T., Heinson, G., Boren, G., Yoneda, A. & Utada, H. (2010). Upper mantle electrical resistivity structure

benath the central Mariana subduction system. *Geochemistry, Geophysics, Geosystems* **11**, doi:10.1029/2010GC003101.

Miyashiro, A. (1974). Volcanic rock series in island arcs and active continental margins. *American Journal of Science* **274**, 312–355.

McDonough, W. F. & Frey, F. A. (1989). REE in upper mantle rocks. In: Lipin, B. & McKay, G. R. (eds) *Geochemistry and Mineralogy of Rare Earth Elements. Mineralogical Society of America, Reviews in Mineralogy* **21**, 99–145.

McDonough, W. F. & Sun, S.-s. (1995). The composition of the Earth. *Chemical Geology* **120**, 223–253.

Münker, C., Weyer, S., Scherer, E. & Mezger, K. (2001). Separation of high field strength elements (Nb, Ta, Zr, Hf) and Lu from rock samples for MC-ICPMS measurements. *Geochemistry, Geophysics, Geosystems* **2**, doi:10.1029/2001GC000183.

Palme, H., O'Neill, H. & St., C. (2005). Cosmochemical estimates of mantle composition. In: Holland, H. D. & Turekian, K. K. (eds) *Treatise on Geochemistry 2. The Mantle, Core*. New York: Elsevier, pp. 1–38.

Parkinson, I. J. & Pearce, J. A. (1998). Peridotites from the Izu–Bonin–Mariana Forearc (ODP Leg 125): Evidence for mantle melting and melt–mantle interaction in a supra-subduction zone setting. *Journal of Petrology* **39**, 1577–1618.

Pearce, J. A. & Stern, R. J. (2006). Origin of back-arc basin magmas: trace element and isotope perspectives. In: Christie, D. M., Fisher, C. R., Lee, S.-M. & Givens, S. (eds) *Back-arc Spreading Systems: Geological, Biological, Chemical and Physical Interactions. Geophysical Monograph, American Geophysical Union* **166**, 63–86.

Pearce, J. A., Kempton, P. D., Nowell, B. M. & Noble, S. R. (1999). Hf–Nd element and isotope perspective on the nature and provenance of mantle and subduction components in western Pacific arc–basin system. *Journal of Petrology* **40**, 1579–1611.

Pearce, J. A., Stern, R. J., Bloomer, S. H. & Fryer, P. (2005). Geochemical mapping of the Mariana arc–basin system: implications for the nature and distribution of subduction components. *Geochemistry, Geophysics, Geosystems* **6**, doi:10.1029/2004GC000895.

Plank, T. & Langmuir, C. H. (1998). The chemical composition of subducting sediment and its consequences for the crust and mantle. *Chemical Geology* **145**, 325–394.

Ranero, C. R., Phipps Morgan, J., McIntosh, K. & Reichert, C. (2003). Bending-related faulting and mantle serpentinization at the Middle America trench. *Nature* **425**, 367–373.

Sakuyama, M. (1983). Petrology of arc volcanic rocks and their origin by mantle diapirs. *Journal of Volcanology and Geothermal Research* **18**, 297–320.

Sato, H. (1977). Nickel content of basaltic magmas: identification of primary magmas and a measure of the degree of olivine fractionation. *Lithos* **10**, 112–120.

Skora, S. & Blundy, J. (2010). High-pressure hydrous phase relations of radiolarian clay and implications for the involvement of subducted sediment in arc magmatism. *Journal of Petrology* **51**, 2211–2243.

Stern, R. J. (2010). The anatomy and ontogeny of modern intra-oceanic arc system. In: Kusky, T. M., Zhai, M.-G. & Xiao, W. (eds) *The Evolving Continents: Understanding Processes of Continental Growth. Geological Society, London, Special Publications* **338**, 7–34.

Stern, R. J. & Bibee, L.D. (1984). Esmeralda Bank: Geochemistry of an active submarine volcano in the Mariana Island Arc. *Contributions to Mineralogy and Petrology* **86**, 159–169.

Stern, R. J., Jackson, M. C., Fryer, P. & Ito, E. (1993). O, Sr, Nd and Pb isotopic composition of the Kasuga Cross Chain in the Mariana Arc: A new perspective on the K–h relationship. *Earth and Planetary Science Letters* **119**, 459–476.

Stern, R. J., Fouch, M. J. & Klemperer, S. L. (2003). An overview of the Izu–Bonin–Mariana subduction factory. In: Eiler, J. (ed.) *Inside the Subduction Factory. Geophysical Monograph, American Geophysical Union* **138**, 175–222.

Stern, R. J., Kohut, E., Bloomer, S. H., Leybourne, M., Fouch, M. & Vervoort, J. (2006). Subduction factory processes beneath the Guguan cross-chain, Mariana Arc: no role for sediments, are serpentinites important? *Contributions to Mineralogy and Petrology* **151**, 202–221.

Stern, R. J., Tamura, Y., Embley, R. W. *et al.* (2008). Evolution of West Rota volcano, an extinct submarine volcano in the southern Mariana arc: evidence from sea floor morphology, remotely operated vehicle observations and ^{40}Ar–^{39}Ar geochronological studies. *Island Arc* **17**, 70–89.

Stolper, E. & Newman, S. (1994). The role of water in the petrogenesis of Mariana Trough magmas. *Earth and Planetary Science Letters* **121**, 293–325.

Takazawa, E., Frey, F. A., Shimizu, N. & Obata, M. (2000). Whole rock compositional variations in an upper mantle peridotite (Horoman, Hokkaido, Japan): Are they consistent with a partial melting process? *Geochimica et Cosmochimica Acta* **64**, 695–716.

Tamura, Y. (2003). Some geochemical constraints on hot fingers in the mantle wedge: evidence from NE Japan. In: Larter, R. D. & Leat, P. T. (eds) *Intra-Oceanic Subduction Systems: Tectonic and Magmatic Processes. Geological Society, London, Special Publications* **219**, 221–237.

Tamura, Y. & Tatsumi, Y. (2002). Remelting of an andesitic crust as a possible origin for rhyolitic magma in oceanic arcs: an example from the Izu–Bonin arc. *Journal of Petrology* **43**, 1029–1047.

Tamura, Y., Yuhara, M. & Ishii, T. (2000). Primary arc basalts from Daisen volcano, Japan: equilibrium crystal fractionation versus disequilibrium fractionation during supercooling. *Journal of Petrology* **41**, 431–448.

Tamura, Y., Tani, K., Ishizuka, O., Chang, Q., Shukuno, H. & Fiske, R. S. (2005). Are arc basalts dry, wet, or both? Evidence from the Sumisu caldera volcano, Izu–Bonin arc, Japan. *Journal of Petrology* **46**, 1769–1803.

Tamura, Y., Tani, K., Chang, Q., Shukuno, H., Kawabata, H., Ishizuka, O. & Fiske, R. S. (2007). Wet and dry basalt magma evolution at Torishima volcano, Izu–Bonin arc, Japan: the possible role of phengite in the downgoing slab. *Journal of Petrology* **48**, 1999–2031.

Tamura, Y., Tatsumi, Y., Zhao, D., Kido, Y. & Shukuno, H. (2002). Hot fingers in the mantle wedge: new insights into magma genesis in subduction zones. *Earth and Planetary Science Letters* **197**, 105–116.

Tanaka, T. *et al.* (2000). JNdi-1: A neodymium isotopic reference in consistency with La Jolla neodymium. *Chemical Geology* **168**, 279–281, doi:10.1016/S0009-2541(00)00198-4.

Tatsumi, Y. (1986). Formation of the volcanic front in subduction zones. *Geophysical Research Letters* **13**, 717–720.

Tollstrup, D., Gill, J., Kent, A., Prinkey, D., Williams, R., Tamura, Y. & Ishizuka, O. (2010). Across-arc geochemical trends in the Izu–Bonin arc: Contributions form the subducting slab, revisited. *Geochemistry, Geophysics, Geosystems* **11**, doi:10.1029/2009GC002847.

Turner, S., Bourdon, B. & Gill, J. (2003). Insights into magma genesis at convergent margins from U-series isotopes. In: Bourdon, B., Henderson, G. M., Lundstrom, C. C. & Turner, S. P. (eds) *Uranium-series Geochemistry. Mineralogical Society of America and Geochemical Society, Reviews in Mineralogy and Geochemistry* **52**, 255–310.

Van Keken, P. E., Kiefer, B. & Peacock, S. M. (2002). High-resolution models of subduction zones: implications for mineral dehydration reactions and the transport of water into the deep mantle. *Geochemistry, Geophysics, Geosystems* **3**, 1056, doi:10.1029/2001GC000256.

Wada, I. & Wang, K. (2009). Common depth of slab–mantle decoupling: reconciling diversity and uniformity of subduction

zones. *Geochemistry, Geophysics, Geosystems* **10**, doi:10.1029/2009GC002570.

Wade, J. A., Plank, T., Stern, R. J., Tollstrup, D. L., Gill, J. B., O'Leary, J. C., Eiler, J. M., Moore, R. B., Woodhead, J. D., Trusdell, F., Fischer, T. P. & Hilton, D. R. (2005). The May 2003 eruption of Anatahan volcano, Mariana Islands: Geochemical evolution of a silicic island-arc volcano. *Journal of Volcanology and Geothermal Research* **146**, 139–170.

Walker, D., Shibata, T. & DeLong, S. E. (1979). Abyssal tholeiites from the Oceanographer Fracture Zone III. Phase equilibria and mixing. *Contributions to Mineralogy and Petrology* **70**, 111–125.

Woodhead, J. D. (1989). Geochemistry of the Mariana arc (western Pacific): Source composition and processes. *Chemical Geology* **76**, 1–24.

Woodhead, J. D., Hergt, J. M., Davidson, J. P. & Eggins, S. M. (2001). Hafnium isotope evidence for 'conservative' element mobility during subduction zone processes. *Earth and Planetary Science Letters* **192**, 331–346.

Yamazaki, T., Seama, N., Okino, K., Kitada, K., Joshima, M. & Oda, H. (2003). Spreading process of the northern Mariana Trough: Rifting–spreading transition at 22°N. *Geochemistry, Geophysics, Geosystems* **4**, doi:10.1029/2002GC000492.

Yokoyama, T., Kobayashi, K., Kuritani, T. & Nakamura, E. (2003). Mantle metasomatism and rapid ascent of slab components beneath island arcs: Evidence from ^{238}U–^{230}Th–^{226}Ra disequilibria of Miyakejima volcano, Izu arc, Japan. *Journal of Geophysical Research* **108**, doi:10.1029/2002JB002103.

Zhu, G., Gerya, T. V., Yuen, D. A., Honda, S., Yoshida, T. & Connolly, J. A. D. (2009). Three-dimensional dynamics of hydrous thermal–chemical plumes in oceanic subduction zones. *Geochemistry, Geophysics, Geosystems* **10**, doi:10.1029/2009GC002625.